공학박사 학위논문

Development of Pinhole X-ray Fluorescence Imaging System to Measure *in vivo* Biodistribution of Gold Nanoparticles

금나노입자의 체내 분포 측정을 위한 핀홀 엑스선 형광 영상시스템 개발

2019년 8월

서울대학교 융합과학기술대학원
융합과학부 방사선융합의생명전공

정 성 문

A dissertation for the degree of Doctor of Philosophy

Development of Pinhole X-ray Fluorescence Imaging System to Measure *in vivo* Biodistribution of Gold Nanoparticles

금나노입자의 체내 분포 측정을 위한 핀홀 엑스선 형광 영상시스템 개발

August 2019

Program in Biomedical Radiation Sciences
Department of Transdisciplinary Studies
Graduate School of Convergence Science and Technology
Seoul National University

Seongmoon Jung

ABSTRACT

Development of Pinhole X-ray Fluorescence Imaging System to Measure *in vivo* Biodistribution of Gold Nanoparticles

Seongmoon Jung
Program in Biomedical Radiation Sciences
Department of Transdisciplinary Studies
Graduate School of Convergence Science and Technology
Seoul National University

Purpose: This work aims to show the experimental feasibility for a dynamic *in vivo* X-ray fluorescence (XRF) imaging of gold in living mice exposed to gold nanoparticles (GNPs) using polychromatic X-rays. By collecting K-shell XRF photons using a 2D cadmium zinc telluride (CZT) gamma camera, the imaging system was expected to have a short image acquisition time and deliver a low radiation dose. This study also investigated the feasibility of using an L-shell XRF detection system with a single-pixel silicon drift detector (SDD) to measure *ex vivo* GNP concentrations from biological samples.

Methods: Six GNP columns of 0 % by weight (wt%), 0.125 wt%, 0.25 wt%, 0.5 wt%, 1.0 wt% and 2.0 wt% inserted in a 2.5 cm diameter polymethyl methacrylate (PMMA) phantom were used for acquiring a linear regression curve between the concentrations of GNPs and the K-shell XRF photons emitted from GNPs. A fan-beam of 140 kVp X-rays irradiated the phantom for 1 min in each GNP sample. The photon spectra were measured by the CZT gamma camera. The K-shell XRF counts were derived by subtracting the photon counts of the 0 wt% PMMA phantom (i.e., pre-scanning) from the photon counts of the GNP-loaded phantom (i.e., post-scanning). Furthermore, a 2D convolutional neural network (CNN) was applied to generate the K-shell XRF counts from the post-scanned data without the pre-scanning. For a more sensitive detection of the *ex vivo* concentrations of GNPs in the biological samples, the L-shell XRF detection system using the single-pixel SDD was developed. Six GNP samples of 2.34 μg–300 μg Au/30 mg water (i.e., 0.0078 wt%–1.0 wt% GNPs) were used for acquiring a calibration curve to correlate the GNP mass to the L-shell XRF counts.

The kidney slices of three Balb/C mice were scanned at various periods after the injection of GNPs in order to acquire the quantitative information of GNPs. The concentrations of GNPs measured by the CZT gamma camera and the SDD were cross-compared and then validated by inductively coupled plasma atomic emission spectroscopy (ICP-AES). The radiation dose was assessed by the measurement of TLDs attached to the skin of the mice.

Results: The K-shell XRF images showed that the concentration of GNPs in the right kidneys from the mice was 1.58±0.15 wt% at T = 0 min after the injection. At T = 60 min after the injection, the concentration of GNPs in the right kidneys was reduced to 0.77±0.29 wt%. The K-shell XRF images generated by the 2D CNN were similar to those derived by the direct subtraction method. The measured *ex vivo* concentration of GNPs was 0.96±0.22 wt% by the L-shell XRF detection system while it was 1.00±0.50 wt% by ICP-AES. The radiation dose delivered to the skin of the mice was 107±4 mGy for acquiring one slice image by using the direct subtraction method while it was 53±2 mGy by using the 2D CNN.

Conclusions: A pinhole K-shell XRF imaging system with a 2D CZT gamma camera showed a dramatically reduced scan time and delivered a low radiation dose. Hence, a dynamic *in vivo* XRF imaging of gold in living mice exposed to GNPs was technically feasible in a benchtop configuration. In addition, an L-shell XRF detection system can be used to measure *ex vivo* concentrations of GNPs in biological samples. This imaging system could provide a potential *in vivo* molecular imaging for metal nanoparticles to emerge as a radiosensitizer and a drug-delivery agent in preclinical studies.

……

Keywords: X-ray fluorescence, pinhole, gold nanoparticles, biodistribution, radiation dose

Student Number: 2014-24851

TABLE OF CONTENTS

CHAPTER III. RESULTS 57

LIST OF TABLES

LIST OF FIGURES

LIST OF ABBREVIATIONS

CCD	Charge-coupled device camera
CdTe	Cadmium telluride
CI	Confidence interval
CNN	Convolutional neural network
CNR	Contrast to noise ratio
CT	Computed tomography
CZT	Cadmium zinc telluride
DI	Deionized
FOV	Field of view
FWHM	Full width half maximum
GdNP	Gadolinium nanoparticle
GFAA	Graphite furnace atomic absorption spectrometry
GNP	Gold nanoparticle
GPU	Graphics processing unit
HPGe	High purity germanium
ICP-AES	Inductively coupled plasma-atomic emission spectroscopy
ICP-MS	Inductively coupled plasma-mass spectroscopy
keV	Kiloelectronvolt
kVp	Peak kilovoltage
LD_{50}	Lethal dose, 50%

M1	Mouse no.1
M2	Mouse no.2
M3	Mouse no.3
MC	Monte Carlo
MCNP	Monte Carlo N-Particle
mGy	Miligray
MNP	Metal nanoparticle
MRI	Magnetic resonance imaging
MR-SPECT	Magnetic resonance-single photon emission computed tomography
NIST	National Institute of Standards and Technology
PET	Positron emission tomography
PMMA	Polymethly methacrylate
ppb	Parts per billion
ROI	Region of interest
SAD	Source to axis distance
SDD	Silicon drift detector
SPECT	Single photon emission computed tomography
TG-61	Radiation Therapy Committee Task Group 61
TLD	Thermoluminescent dosimeter
XFCT	X-ray fluorescence computed tomography
XRF	X-ray fluorescence
Z	Atomic number

CHAPTER I. INTRODUCTION

I.1 Applications of Metal Nanoparticles in Medicine

There has been a dramatic increase in the interest in the use of metal nanoparticles (MNPs) for medical applications for a few past decades. Particularly, the applications of MNPs in the cancer therapy and diagnosis have become emerging research areas, which include for tumor targeting, for drug and gene delivery, as an imaging contrast agent and as a radiosensitizer (Fig. 1).[1-5] Among the various MNPs, high atomic number (Z) MNPs made from, for instance gold (Au), gadolinium (Gd), barium (Ba), iodine (I) or silver (Ag), were proven to have the greatest potential.[6,7] Due to their high X-ray absorption properties, high Z MNPs as the imaging contrast agent have been used for X-ray imaging or computed tomography (CT).[8] For another example, gadolinium oxide nanoparticles (GdNPs) provide a contrast enhancement for magnetic resonance imaging (MRI).[9-11] Since Hainfeld *et al.* firstly demonstrated the feasibility of using gold nanoparticles (GNPs) as the radiosensitizer in 2004,[12] a variety of studies have been reported on MNP enhanced radiation therapy using external X-ray sources, brachytherapy sources, as well as proton and carbon ion beams.[13-21]

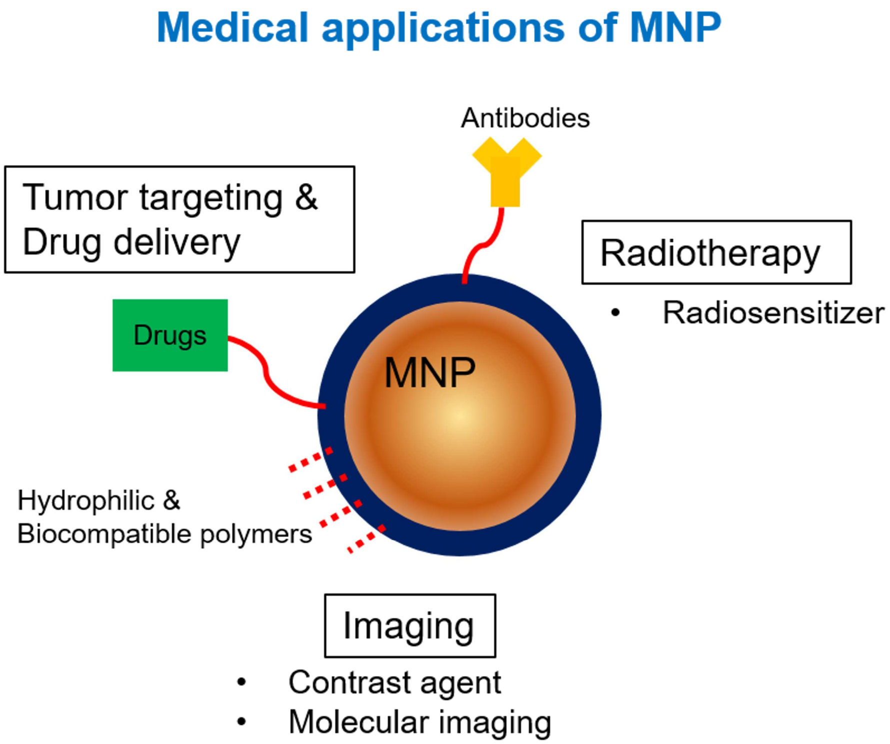

Fig. 1. Schematic illustration of applications of MNP in medical field.

I.2 Molecular Imaging of Metal Nanoparticles

When the specific organs or tumors are targeted with the nanomaterial conjugated with high Z MNPs, functional information in the target regions can be acquired by imaging those high Z MNPs. Preclinical studies using high Z MNP injected into small animals indicate that the dynamic biodistribution of MNPs is crucial to evaluating biological effect and toxicity. The most common method used for this purpose is to measure the *ex vivo* concentration of MNPs using inductively coupled plasma-mass spectroscopy (ICP-MS) or -atomic emission spectroscopy (ICP-AES) and graphite furnace atomic absorption spectrometry (GFAA).[6,8] Although these methods measure very low concentration of MNPs (i.e., in ppb), they require complex sampling procedures such as tissue excision, freeze-drying, and chemical preprocessing. In order to further implement high Z MNPs in clinical practices, monitoring the biological effect and toxicity must be carried out based on *in vivo* biodistribution of MNPs in the tumors and normal tissues.[6]

However, CT, which is the most popular imaging modality in the medical field, only offers anatomical information so that it cannot solely accommodate high demand for functional and molecular information in diagnosis. Conventional molecular imaging modalities, which provide functional information such as single photon emission computed tomography (SPECT) and positron emission tomography (PET) using radio-labeled drugs, have been used for decades in clinical diagnoses and preclinical studies.[6,22,23] However, an administration time and imaging procedures are limited due to the radioactivity and lifetime of the isotopes. In preclinical studies, modalities such as optical fluorescence imaging, diffuse optical tomography, and photo-acoustic imaging have been widely used to measure *in vivo* biodistributions of MNPs.[6,24-26] However, those modalities have a substantial limitation on imaging depth due to light scattering.[27] Recently, with the technical advance of energy resolving detectors, *in vivo* imaging of high Z MNPs using a spectral CT has been also studied.[28]

I.3 X-ray Fluorescence Imaging

I.3.1 Principle of X-ray Fluorescence Imaging

In addition to the aforementioned modalities, another promising method is X-ray fluorescence (XRF) imaging or X-ray fluorescence computed tomography (XFCT).[6,29] When an incoming radiation (e.g., X-ray or charged particles) interacts with MNPs, inner subshells (i.e., K- or L-shell) electrons are ejected out of the shells. The energy of the incoming radiation should be larger than the electron binding energies of the subshells (i.e., K- or L-edge energy). Then a vacancy in the inner shell S_0 is initiated mostly due to photoelectric effect (or ionization event for charged-particles). When the electron from the outer subshells S_1 fills the vacancy in the S_0, an isotropic XRF photon is generated with the given energy of E_{01} and the probability of P_{01}. The E_{01} is the difference of the binding energy between the S_0 and the S_1, while the P_{01} can be determined by either calculations or experiments. Since the number of the emitted XRF photons is proportional to the quantity of the MNPs, the XRF photons are used to determine the *in vivo* quantifications and distributions of MNPs. An energy resolving detector measures photon spectra including Compton scattered photons from the MNP-loaded or -injected into object and the XRF photons emitted from the MNPs. When the XRF photons are well discriminated from the Compton scattered photons, XRF images of MNPs can be generated. A schematic diagram of the emission of typical XRF photons is shown in Fig. 2 and the principal XRF peaks of Au are listed in Table 1.[30]

In comparison with the aforementioned modalities in I.2, the XRF imaging can overcome the depth-penetration limitation existed in the modalities using the optical signals. Compared with SPECT and PET that use the radio-labeled drugs, the XRF imaging can be performed to image the MNPs injected into animal without the synthesis procedure of isotopes, special storage room, limited administration time and special care after the process.[31] Therefore, the XRF imaging can provide a biological monitoring over whole *in vivo* study cycle. Although, the spectral CT provides higher spatial resolution and rapid imaging acquisition time than those of the XRF imaging, higher molecular sensitivities are expected to be achieved in the XRF imaging.[28,31]

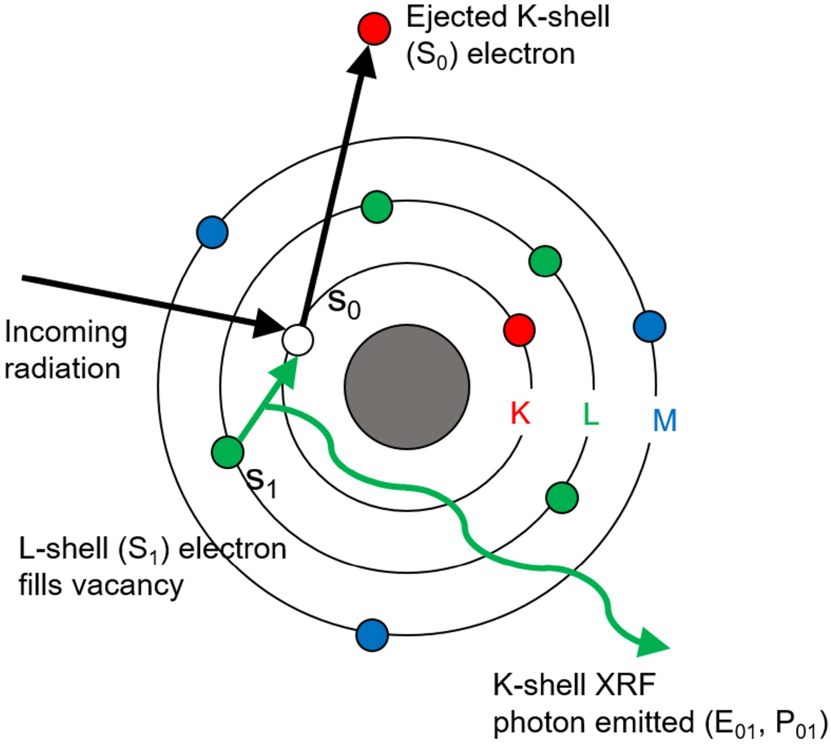

Fig. 2. Schematic diagram of emission of X-ray fluorescence.

Table 1. Principal K-shell and L-shell X-ray fluorescence (XRF) peaks of gold.[30]

Subshell, S_0-S_1	K-L_2	K-L_3	K-M_2	K-M_3	L_1-M_2	L_1-M_3	L_2-M_4	L_2-N_4	L_3-M_4	L_3-M_5	L_3-N_5
Line notation	$K_{\alpha2}$	$K_{\alpha1}$	$K_{\beta3}$	$K_{\beta1}$	$L_{\beta4}$	$L_{\beta3}$	$L_{\beta1}$	$L_{\gamma1}$	$L_{\alpha2}$	$L_{\alpha1}$	$L_{\beta2}$
Energy, E_{01} (keV)	67.18	69.04	77.82	78.23	11.19	11.60	11.48	13.42	9.62	9.71	11.59
Probability, P_{01} (%)	28.01	47.66	5.24	10.14	2.74	3.17	28.95	5.71	2.54	22.36	4.18

I.3.2 History of X-ray Fluorescence Imaging

The first XRF imaging was suggested in 1986 by using a synchrotron X-ray source.[32] The X-rays from synchrotron facilities have quasi-monochromatic energies and can provide slight higher energy than the K- or L-edge energy of the metal. The cross-section of photoelectric effect is dependent on the energy of incoming X-rays and is the highest when the energy of incoming X-rays is slightly higher than the edge energies. Therefore, a large amount of XRF photons can be generated when the X-rays from synchrotron facilities are used as the excitation source. However, due to the limited access to synchrotron facilities, researchers utilized polychromatic X-ray sources that are now available on a laboratory scale. Cheong *et al.* proposed the XRF imaging system using polychromatic X-ray source in 2010.[33] Focusing on the K-shell XRF imaging, Jones *et al.* detected 0.5% by weight (wt%) Au by using 105 kVp cone-beam X-rays.[34] Ahmad *et al.* showed images of 0.25 wt% GNP using 120 kVp pencil beam X-rays by optimizing detector angular configuration.[35] Since they used a single-pixel energy resolving detector, a rotation of the phantom and a translation of the detector were required to obtain tomographic images. The image acquisition time for an image was 90 min per slice.[27]

In order to reduce the image acquisition time, the groups of Meng and of La Riviere demonstrated improved images obtained by 2D position-sensitive detectors computationally and experimentally.[36,37] In these studies, synchrotron X-rays and pinhole collimation with a 2D X-ray charge-coupled device (CCD) camera which has detection efficiency of ~30% at 10 keV and ~15% at 15 keV were used to detect

XRF photons in iron (Fe), zinc (Zn), and bromine (Br) solutions. The energies of K-shell XRF of those elements are from 6.4 keV to 13.3 keV. Very small samples (i.e., 0.75-mm-diameter cylindrical tube) were used due to the limited penetration depth of these low-energy XRF photons. Furthermore, they recently demonstrated K-shell XRF imaging of Fe, Br and copper (Cu) solutions by using polychromatic X-rays with a slit collimator.[38] Sasaya *et al.* proposed a multi-pinhole XFCT system using 2D silicon (Si) detector and synchrotron X-rays.[23] They measured K-shell XRF photons (i.e., ~29 keV) emitted from I and L-shell XRF photons emitted from GNPs inserted in a 1 cm diameter phantom, since the detectable energy range of the 2D Si detector was 5.4-36 keV.[23,39] More recently, a benchtop XFCT system with a linear-array cadmium zinc telluride (CZT) detector was developed for *in vivo* imaging of Gd in living mice exposed to GdNPs. With an implementation of the linear-array CZT detector, the image acquisition time was reduced to 7.5 min per slice.[40]

On the other hand, several researchers claimed that the GNP concentrations used in the aforementioned XFCT experiments were not realistic in present cell targeting techniques, because the GNP concentrations in the tumor were expected to be an order of 0.001 wt%.[41-43] Therefore, an L-shell XRF imaging was suggested to achieve higher detection sensitivity than that of the K-shell XRF imaging. The L-shell XRF imaging for GNP can detect much lower concentration than does the K-shell XRF imaging due to much higher photoelectric absorption and much lower amount of Compton scattered photons. The group of Cho achieved the detection limit of ~0.001 wt% with 60 kVp pencil beam.[44] The group of Xing measured 0.06 wt%

GNP in a 2.8 cm diameter phantom using 50 kVp pencil beam.[43] Moreover, the detection limits of the both benchtop K-shell and L-shell XRF detection systems were investigated experimentally.[45,46] The estimated detection limits were 0.0005 wt% and 0.02-0.06 wt% in 0.8 cm diameter plastic tubes for the L- and K-shell XRF detection systems, respectively.[45,46] The silicon drift detector (SDD) and Si-PIN detector were well-known detectors for measuring the L-shell XRF photons due to their high energy resolution and low noise in the energy range for the L-shell XRF photon peaks of Au. However, a shallow thickness of the Si substrate (i.e., 500 μm in SDD) causes an inefficient absorption for the higher energy photons. In other words, the penetration depth of the L-shell XRF photons strongly limits the use of the L-shell XRF imaging technique to small samples whose diameter and thickness are less than 1 cm.[41-44] The groups working on the XRF imaging system using polychromatic X-rays were listed in Table 2 with respect to the type of metal, the type of XRF peaks (i.e., K- or L-shell XRF), the shape of X-ray beam, the type of detector, the design of collimator, the measured concentration by the systems, and the diameter of the phantom.

Table 2. List of research group of benchtop XRF imaging system and summary of their experimental parameters.

Group	Metal	XRF	Measured concentration (wt%)	Beam shape	detector	collimator	Phantom (cm)	REF
Cho	GNP (Au)	K-shell	0.24	Cone	CdTe	Parallel hole	3	27, 34
		L-shell	0.001	Pencil	SDD	Parallel hole	~0.8	44
Xing and Bazalova	$AuCl_3$	K-shell	0.25	Pencil	CdTe	-	6.4	35
		L-shell	0.06	Pencil	SDD	-	2.8	43
La Riviere and Meng	Fe, Cu, Br	K-shell	25	Pencil	2D CCD	Slit	0.1	38
Li and Chen	GdNP (Gd)	K-shell	0.2	Cone	Linear-array CZT	Pinhole	5	40
Ricketts	GNP (Au)	K-shell	0.02	Pencil	HPGe	Parallel hole	0.8	46
		L-shell	0.0005	Pencil	SDD	Parallel hole	0.8	45

I.3.3 Specific Aims

The K-shell XRF imaging for high Z MNP has more potential to be used in preclinical studies than does the L-shell XRF imaging in terms of the imaging depth. However, two major limitations are existed in the current benchtop K-shell XRF imaging techniques:

1. *Long image acquisition time: 90 min per slice in the benchtop XFCT system with the single-pixel photon counting detector*[27] *and 7.5 min per slice in the benchtop XFCT system with the linear-array photon counting detector.*[40]
2. *Shallow imaging depth (< 1 cm) in XFCT system with the 2D position sensitive detector (CCD camera or Si detector).*[38,39]

In order to overcome these limitations, a new K-shell XRF imaging system was suggested in this study. The K-shell XRF imaging system consists of

1. *Commercial 2D position-sensitive and energy-resolving detector having the detectable energy range of 35–285 keV for a rodent in vivo imaging*
2. *Pinhole collimator to achieve a direct 2D slice image of the MNPs injected into object irradiated by fan-beam polychromatic X-rays without image reconstruction*

In this work, a Monte Carlo (MC) model was designed to show the feasibility of K-shell XRF imaging of GdNP and GNP in cylindrical water phantoms. Among various MNPs, GdNP and GNP likely have the highest potential for being used as an imaging contrast agent and as a radiosenstizer. In particular, GNPs were proved to be much safer and less toxic sensitizing agents for the cancer treatment.[6] The model consists of the cylindrical water phantom, fan-beam polychromatic X-rays, pinhole collimators and 2D arrays of CZT gamma camera. The K-shell XRF photons stimulated by incoming X-rays, behave like isotropically emitting gammas. Photons passing through a pinhole have their own positions and energy information so that one can acquire a 2D slice image directly from a single sheet of fan-beam irradiation without image reconstruction or rotation of the object. The pinhole K-shell XRF imaging system has an imaging mechanism very similar to SPECT.[33] Hence, the design and dimension of the pinhole, and the type and the pixel size of the detector were benchmarked commonly used in preclinical pinhole SPECT.[47-51] The MC model was created by using Monte Carlo N-Particle Version 6.1 (MCNP6.1).[52] The MCNP6.1 code has been widely used for the simulation studies of CZT, CdTe, and HPGe semiconductor detectors for medical imaging.[53-55] The XRF images generated by the MC model were quantitatively evaluated in terms of image quality and imaging doses.

This work also aims to show the experimental feasibility for a dynamic *in vivo* K-shell XRF imaging of Au in living mice exposed to GNPs. The configurations and the part of geometrical dimensions of the developed K-shell XRF imaging system were based on the suggested MC model. By collecting K-shell XRF photons using a commercial 2D CZT gamma camera, the imaging system was expected to have a short image acquisition time and deliver a low imaging dose. The dynamic *in vivo*

K-shell XRF imaging of GNPs in the kidneys of three Balb/C mice was performed. The concentrations of GNPs in the kidneys were quantified with respect to the time that had elapsed after the injection. Furthermore, this investigation also showed the feasibility of using an L-shell XRF detection system with SDD to measure *ex vivo* GNP concentrations from excised biological samples without the complex sampling procedures that were required by ICP-AES. The concentrations measured by the *in vivo* K-shell XRF imaging system and the L-shell *ex vivo* XRF detection system were cross-compared. The measured *ex vivo* concentrations were then validated by ICP-AES. The objectives in this study were formulated as follows:

> ***Aim 1:*** *Design a MC model for a pinhole K-shell XRF imaging system with a commercial 2D CZT gamma camera and find a methodology for XRF signal processing.*

> ***Aim 2:*** *Demonstrate in GNP-loaded imaging phantoms that the developed pinhole K-shell XRF imaging system based on the MC model reduce the image acquisition time.*

> ***Aim 3:*** *Show the experimental feasibility of dynamic in vivo XRF imaging of Au in living mice exposed to GNP using the developed pinhole K-shell XRF imaging system*

CHAPTER II. MATERIAL AND METHODS

II.1 Monte Carlo Model

II.1.1 Geometry of Monte Carlo Simulations

A geometry of MC model was illustrated in Fig. 3. A cylindrical water phantom in the middle of Fig. 3(a) had a diameter of 5 cm and a height of 5 cm. In the phantom were placed four 1 cm diameter and 3 cm height cylindrical water columns containing Gd or Au of different concentrations: 0.01 wt%, 0.03 wt%, 0.06 wt%, and 0.09 wt% as shown in Fig. 4. Two pinhole collimators were located on both sides of the phantom, having a pinhole of 2 mm diameter on a lead sheet of 5 mm thickness. The pinhole had cone-shaped profiles with an acceptance-angle of 102° (Fig. 3(b)). The beam plane-to-collimator and the collimator-to-detector distances were 2.5 cm.

The incident X-ray beam was specified as a fan-beam of 5 mm width and 5 cm length. Due to high-energy resolution of semiconductor detector, a commercial pixelated CZT gamma camera comprised of four SRE4001-CZT25.4 modules (Integrated Detect Electronics AS, Oslo, Norway) has been chosen as a detector.[56,57] The detector consisted of 32×32 pixels of which each pixel had a dimension of 1.6×1.6 mm^2 and a 5 mm thickness. The detector had an Al6061 window of 1.5 mm thickness in front of the CZT crystal. The detector was assumed to be position-sensitive and to have 100% detective quantum efficiency due to the high attenuation coefficient of CZT. The geometric efficiency, g was calculated in (1) and (2)[49]:

$$g \approx d_{eff,g} \cos^3 \theta / 16b^2 \tag{1}$$

where $d_{eff,\,g}$ is the effective pinhole diameter calculated as (2), θ is the angle between the source (a mid-plane in water phantom where the incident X-rays pass through) and a pinhole, and b is the beam plane-to-pinhole distance.

$$d_{eff,g} = \sqrt{d[d + 2\mu^{-1} \tan(\alpha/2) + [(2\mu^{-2}) \tan^2(\alpha/2)]} \tag{2}$$

The effective pinhole diameter $d_{eff,\,g}$ accounts for penetration of the edges of the pinhole aperture. d and α are the pinhole diameter and acceptance angle, respectively. μ is the linear attenuation coefficient of collimator material (i.e., lead). The system resolution R_{sys} was calculated by (3)-(5)[49]:

$$R_{sys} = \sqrt{R_{\mathrm{int}}^2 + R_{coll}^2} \tag{3}$$

$$R_{coll} \approx d_{eff,R} (l + b) / l \tag{4}$$

$$d_{eff,R} = d + (\ln(2)/\mu) \tan(\alpha/2) \tag{5}$$

where R_{int} is the intrinsic resolution of the detector, R_{coll} is the collimator resolution, l is the distance from pinhole to active surface of detector. The field-of-view (FOV) in this configuration was 5.12 cm in diameter. However, the magnification factor and the FOV were adjustable by varying the beam plane-to-collimator and the collimator-to-detector distances. Utilizing the geometrical symmetry of collimator-and-detector configuration (shown in Fig. 3(a)), MC images from the both sides were combined to reduce noise for a given computation time.

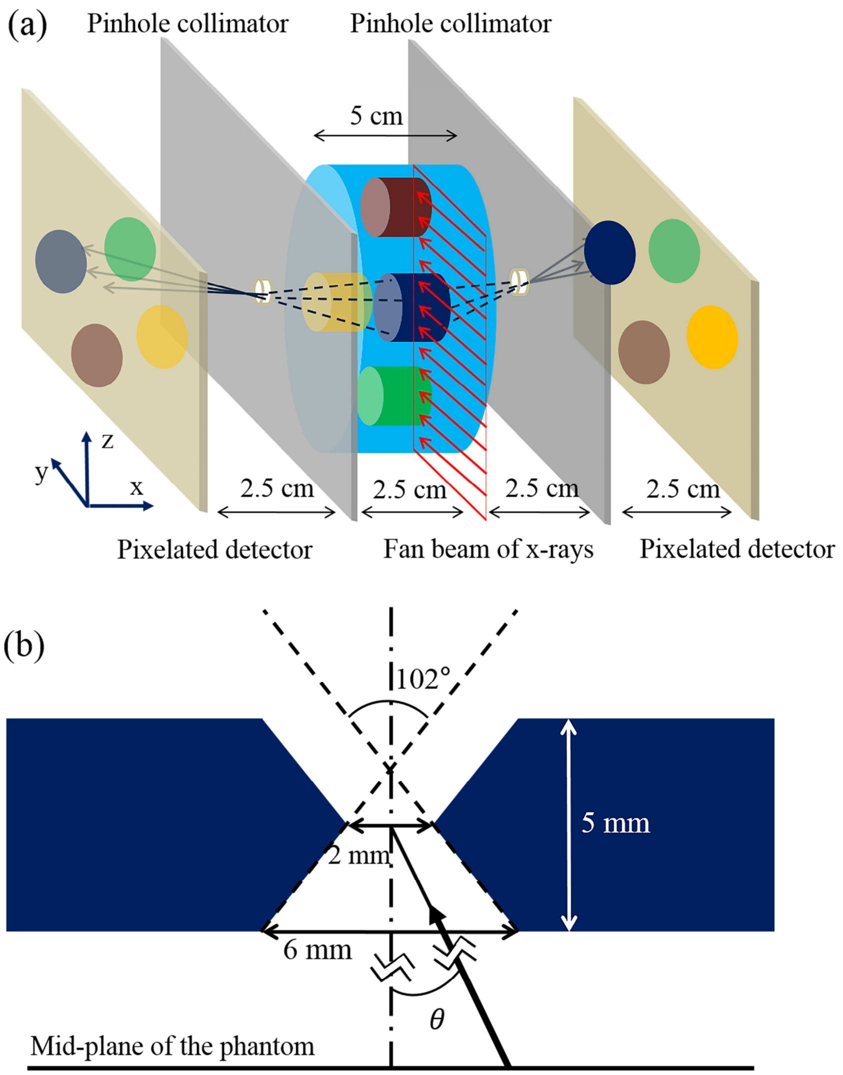

Fig. 3. (a) MC simulation geometry for pinhole K-shell XRF imaging system and (b) schematic of pinhole collimation, where the acceptance angle is 102°.

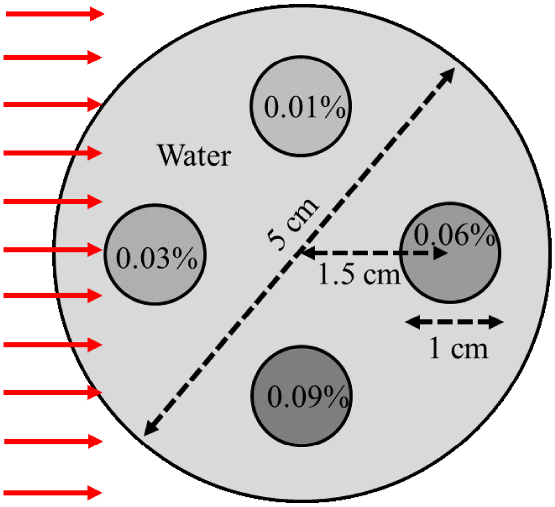

Fig. 4. Imaging water phantom where four columns are assumed to have different concentrations of either Gd or Au. The rightwards arrows indicate the incident fan-beam X-rays. Gd or Au columns of 0.01 wt%, 0.03 wt%, 0.06 wt%, and 0.09 wt% are located in left, in, out, and right with respect to the incident direction of X-rays, respectively.

A benchtop XFCT has a technical obstacle that Compton scattered photons considerably obscure the detection of K-shell XRF photons. There have been two approaches reported to enhance the discrimination of XRF photons from the Compton scattered photons: first, Ahmad *et al.* suggested an optimized spectro-spatial detector configuration,[35,58] second, Manohar *et al.* found that increasing incident X-ray energy made the gold XRF peaks more easily discerned from the Compton scattered photons.[55] Since the source and the detector arrays had a fixed angle of 90° in the simulation geometry, the later method was implemented.

In order to acquire Gd K-shell XRF images, 110 kVp polychromatic X-rays filtered with tungsten 0.3 mm were used. For Au K-shell XRF imaging, 140 kVp X-rays with Al 1.5 mm, Cu 0.25 mm, and Sn 0.75 mm filtration were used. The filter used for 140 kVp was one of the commercial filters of X-ray machine (X-RAD 320, Precision X-ray Inc., North Branford, CT, USA). The energy spectra of the above two polychromatic X-rays were extracted from the SpekCalc code that has been validated with measurements and MC results and used in several studies.[59-62] In addition, monochromatic X-rays with four different energies (i.e., 51, 60 keV for Gd, and 81, 95 keV for Au) were used to compare the image quality and the radiation dose. The X-rays of 51 and 81 keV were expected to have high photoelectric cross-sections that led high fluorescence emission, since they were close to K_{edge} energies of Gd (i.e., 50.2 keV) and Au (i.e., 80.7 keV), respectively. The X-rays of 60 and 95 keV were chosen to increase the incident X-ray energies to avoid large Compton scattered photons reaching the detector, according to Manohar *et al.*[55] The incident

X-ray source spectra for Gd and Au are shown in Fig. 5. Each simulation was conducted for 1×10^{11} histories by using mcnp6.mpi in a Linux cluster. With this number of incident particles, the image quality and the radiation dose for different X-ray spectra were evaluated.

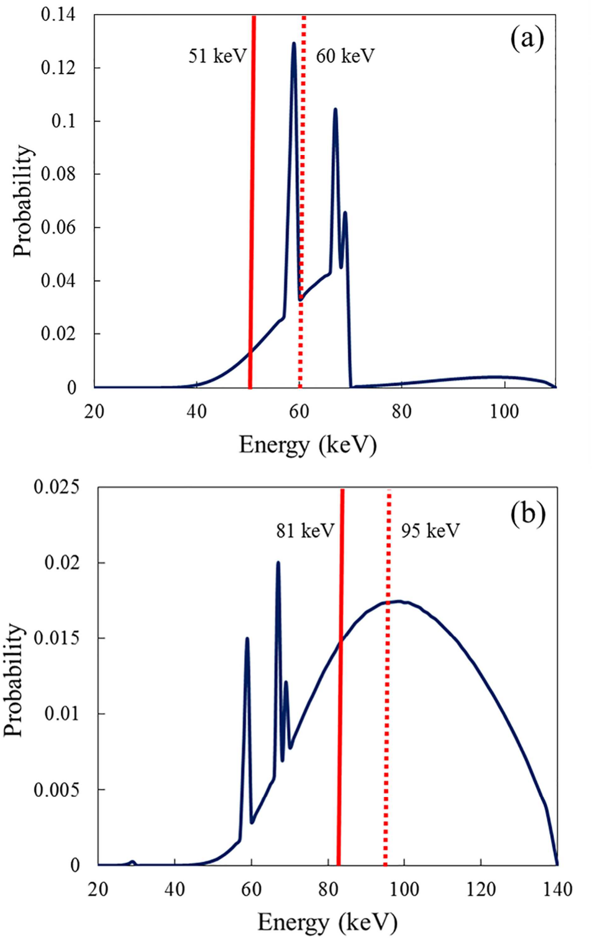

Fig. 5. Three X-ray source spectra for pinhole K-shell XRF imaging for (a) Gd and (b) Au.

II.1.2 Image Processing

The K-shell XRF photons and the Compton scattered photons reaching the detector array were tracked by the energy-specific pulse-height tallies (i.e., F8 of MCNP6.1). In order to detect distinct K-shell XRF peaks above the Compton scattered photons, an energy bin of 1 keV was set to the detector tallies in the simulations. The $K_{\alpha 1}$ and $K_{\alpha 2}$ peak energies of Gd are 43.0 keV and 42.3 keV. The Au XRF lines have their peaks at 69.0 keV and 67.2 keV. The raw XRF signals were obtained by selectively subtracting the $K_{\alpha 1}$ and $K_{\alpha 2}$ photon counts of the pure water phantom from the same energy photon counts of the water phantom with the Gd or Au columns inserted.

Since the energy resolution of the CZT gamma camera was much higher than 1 keV, a degradation of simulation results was needed to reflect realistic situation. The energy spectrum of Am-241 radio-isotope (Ortec, Oak Ridge, TN, USA) emitting 59.5 keV gammas was measured by using the CZT gamma camera. The Am-241 source was electrodeposited resulting in an active area of 3 mm diameter on a palladium disk of 12.7 mm diameter and 0.127 mm thickness. At the source-to-detector distance of 5 cm, the spectrum was measured by the CZT gamma camera for 1 hour at room temperature. All 1024 pixel counts were averaged over to determine %full width half maximum (%FWHM) of the detector at 59.5 keV. %FWHM at 59.5 keV was assumed that it might not be significantly different from those at K-shell XRF energies of Gd (~43 keV) and Au (~68 keV). Degrading the simulated photon spectra for 110 kVp and 140 kVp X-rays with the measured %FWHM caused the XRF peaks to be broadened. The raw XRF signals were derived by subtracting 41–46 keV photon counts (for Gd XRF imaging) and 66–71 keV photon counts (for Au XRF imaging) of the pure water phantom from the same energy photon counts of the water phantom with Gd or Au columns inserted.

The attenuation correction for the incident beam and XRF photons was taken into account by using mass attenuation coefficient tables published from NIST[63] as (6):

$$N_a^i = N_0^i (1/e^{-\mu_I y^i})(1/e^{-\mu_K x^i}) \qquad (6)$$

where N_a^i is the attenuation corrected fluorescence photon counts, N_0^i is the raw XRF counts of i^{th} pixel, μ_I is the linear attenuation coefficient of water at the incident X-ray energy, μ_K is the linear attenuation coefficient of water at K-shell XRF energy (i.e., Gd: 43 keV, and Au: 68 keV). The mid-plane of water phantom where the incident fan-beam passed through was divided into 32 × 32 pixels (like pinhole projection of detector array). Since the beam plane-to-collimator and collimator-to-detector distances were same, it was assumed that the photons from i^{th} pixel of the mid-plane arrived at i^{th} pixel of the detector. y^i is the path length of incident X-rays in the phantom, while x^i indicates the path length of XRF photons of i^{th} pixel in the phantom (Fig. 6). For the polychromatic X-rays, the term $e^{-\mu_I y^i}$ was replaced with (7):

$$e^{-\mu_I y^i} = \left(\sum_{m=E_K}^{E_{\max}} N_m e^{-\mu_m y^i}\right) / \sum_{m=E_K}^{E_{\max}} N_m \qquad (7)$$

where N_m and μ_m are the number of photons and the linear attenuation coefficient of water at the photon energy *m*, respectively. E_K is the energy right above K_{edge} energy (i.e., Gd: E_K = 51 keV, and Au: E_K = 81 keV). Since the incident X-rays below K_{edge} energies could not contribute to the XRF signals, those photons were excluded in (7). $E_{\max}$ is the maximum energy of incident polychromatic X-rays.

As the radial distance from the central pixel of the detector array increases, the detection sensitivity of peripheral pixels suffers from the inverse distance-square.[64] Such sensitivity correction factors were determined from empirical data obtained by additional MC simulations. As shown in Fig. 7, a virtual disk source of 5 cm diameter and 5 mm height cylinder that was isotropically emitting the same energy photons with K-shell XRF (i.e., Gd: 43 keV, Au: 68 keV) was located in a position of the mid-plane of water phantom. The sensitivity of the pinhole collimator is best for photons originating from the center of the virtual source, whereas photons from the periphery are much less detectable. The photon counts detected by each pixel of the detector were normalized against the value of the central pixel. The reciprocals of each value are the sensitivity correction factors.

By multiplying all the correction factors by the raw XRF signals of each pixel, corrected pixel values were obtained. These corrected values directly plotted on a

2D map, representing the location and concentration of Gd or Au columns. A Gaussian filter was applied to decrease noise. Contrast to noise ratio (CNR) was used to evaluate the image quality for the incident X-ray spectra as (8):

$$CNR = (\overline{C}_{ROI} - \overline{C}_{bg})/\sigma_{bg} \qquad (8)$$

where $\overline{C}_{ROI}$ and $\overline{C}_{bg}$ are the mean pixel values in the region of interest (ROI) and background region, respectively. The ROIs were the pixels projected by the Gd or Au columns, while the background region was set to the central pixels of FOV. σ_{bg} is the standard deviation of pixel values in background region.

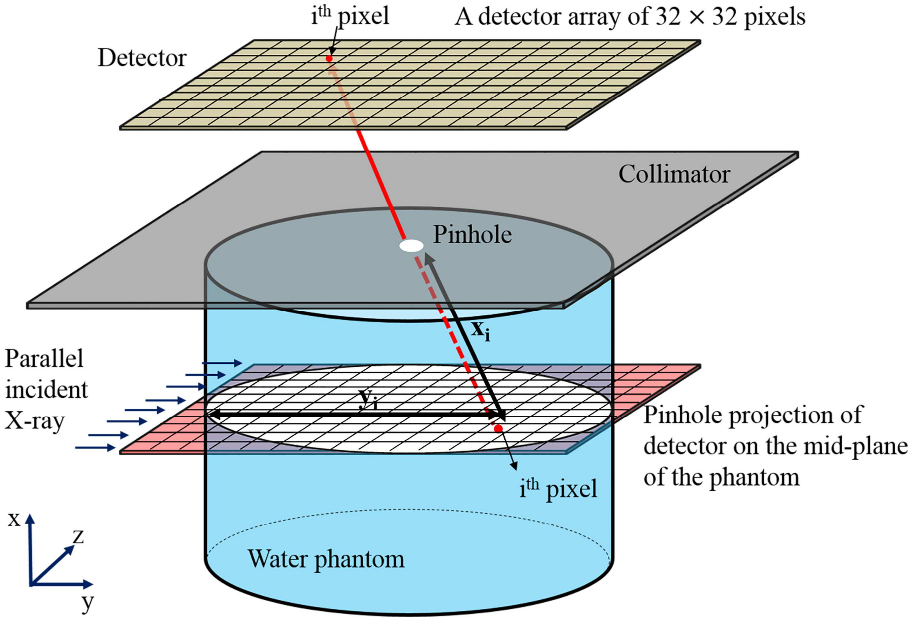

Fig. 6. Schematic of pinhole XRF imaging system. The mid-plane of water phantom was divided into 32 × 32 pixels of which each had 1.6 × 1.6 mm^2. y^i is the path length of incident X-rays in the phantom, while x^i is the path length of XRF photons of i^{th} pixel in the phantom.

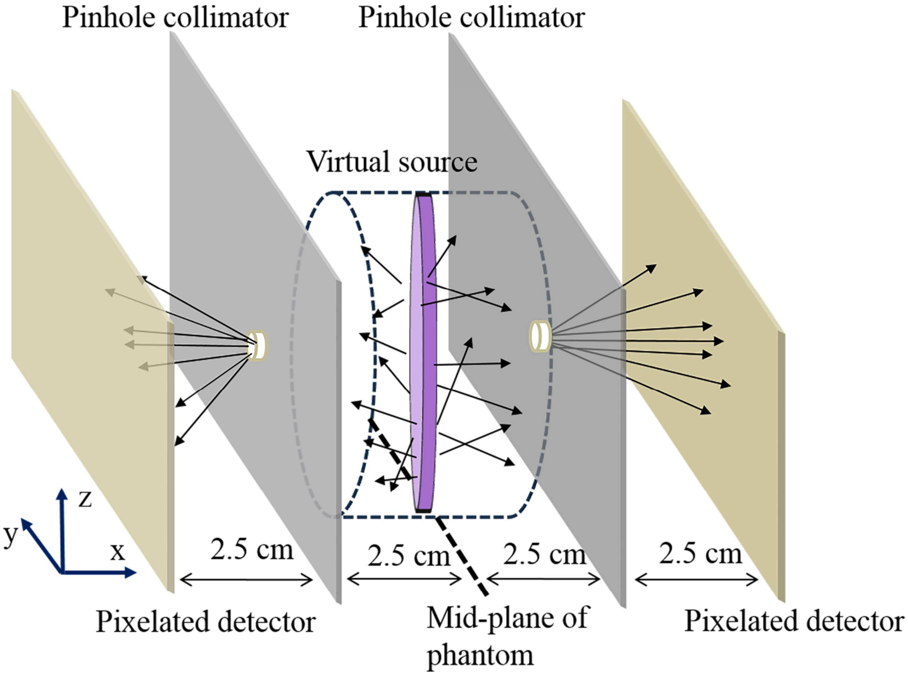

Fig. 7. MC simulation model for sensitivity correction. The virtual disk source of 5 cm diameter and 5 mm width in the mid-plane of water phantom isotropically emits fluorescence-like photons. The arrows describe photons emitting from the virtual source. The photons originating from the center of the source are detected more efficiently than those from the periphery.

II.1.3 Radiation Dose

The average dose to the water phantom for three incident X-ray spectra for each of Gd and Au XRF imaging was assessed by MC simulations. For each simulation, the energy deposited per history in the irradiated volume (i.e., 5 cm diameter and 5 mm height cylinder) of the water phantom was simulated for 1×10^{11} histories using the energy deposition tallies (*F8 of MCNP6). The average dose was determined by dividing the energy deposition per history by the mass of the irradiated volume and then multiplied it with 1×10^{11}.

II.2 Development of Pinhole K-shell XRF Imaging System

II.2.1 System Configuration and Operation Scheme

Based on the MC model, the K-shell XRF imaging system was developed. The XRF imaging system consists of fan-beam polychromatic X-rays, the pinhole collimator and the CZT gamma camera (Integrated Detect Electronics AS, Oslo, Norway) as the MC model suggested. Particularly, the diameter of the pinhole collimator and the peak voltage and the filter of the X-ray sources were exactly the same as the MC model. In addition, the methodology for the image processing was basically the same as the MC study. Moreover, additional XRF detection systems by using a single-pixel CdTe detector (X-123CdTe, Amptek Inc., Bedford, USA) and a SDD (X-123SDD, Amptek Inc., Bedford, USA) were also developed to cross-compare the concentrations measured by the CZT gamma camera. In summary, the whole XRF detection system in this investigation consists of (Fig. 8):

1. *K-shell in vivo XRF imaging system with the 2D CZT gamma camera and the pinhole collimator*
2. *K-shell in vivo XRF detection system with the single-pixel CdTe detector and the parallel hole collimator*
3. *L-shell ex vivo XRF detection system with the single-pixel SDD*

The incident X-rays passing through the tungsten fan-beam collimator interact with GNP-loaded object. On the right side of the object, the pinhole collimator made of tungsten and lead is located. The secondary photons including the Compton scattered photons and the XRF photons passing through the pinhole reach the CZT gamma camera. At the same time, on the left side of the object, the CdTe detector with the parallel hole collimator is located. The K-shell XRF photons and the Compton scattered photons are measured by the CdTe detector. In the actual measurement situation, once 2D images are acquired by the CZT gamma camera, the CdTe detector with the parallel hole collimator is translated to the point of interest to be measured. The L-shell XRF detection system is used to measure much lower concentration of GNPs from excised biological samples from the object. The SDD was well-known to measure the L-shell XRF photons due to their high-energy resolution and low noise in the energy range of the L-shell XRF photons of Au.

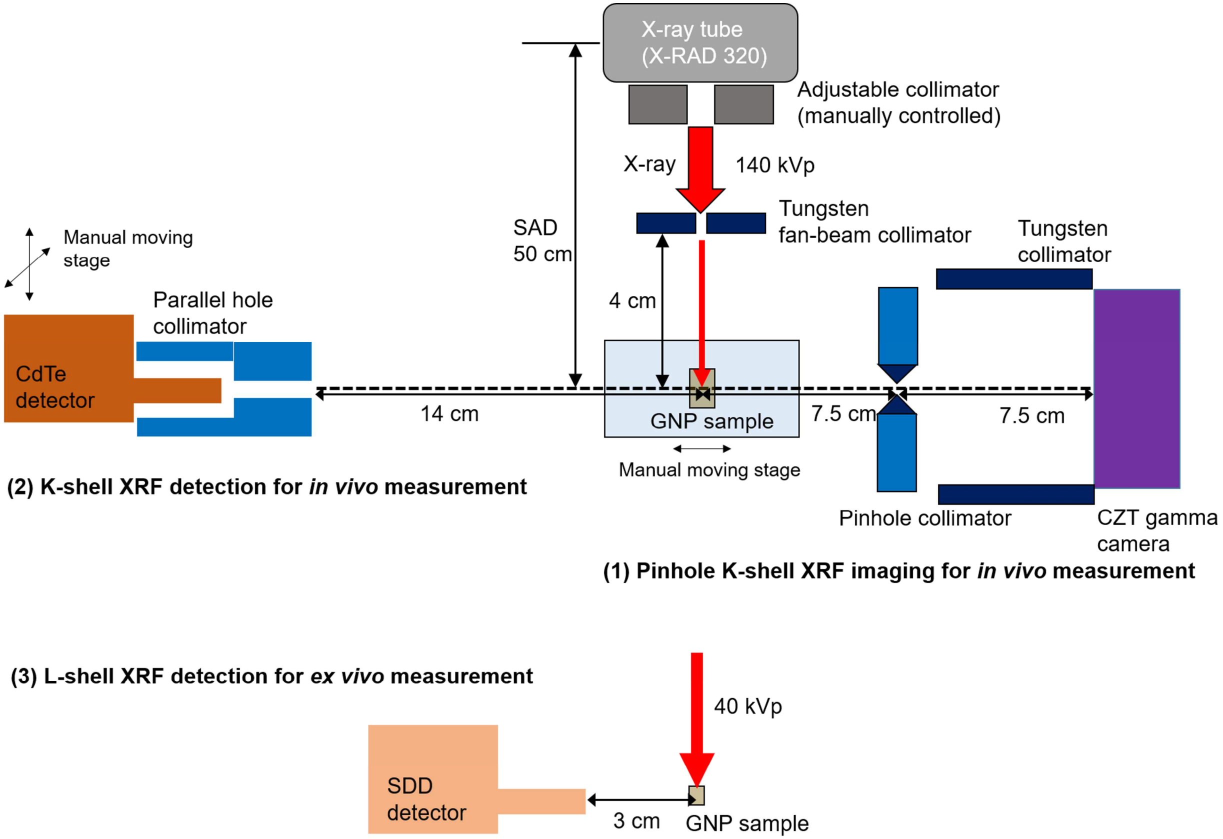

Fig. 8. Schematic diagram of a benchtop configuration of whole XRF detection system.

II.2.2 Pinhole K-shell XRF Imaging System

II.2.2.1 *Experimental Setup*

As mentioned in the previous section, the pinhole K-shell XRF imaging system was assembled based on the proposed MC model. The system consists of the movable sample stage, the pinhole collimator, the cylindrically shaped tungsten collimator and the CZT gamma camera (Fig. 9). The pinhole collimator and the CZT gamma camera were placed perpendicular to a beam direction. The inner of the pinhole was 2 mm as same as the diameter that was designed in the MC model. The outer diameter of pinhole was 4.88 mm with an acceptance angle of 40°. The pinhole of collimator was made of tungsten while the rest of the collimator was made of lead as shown in Fig. 9(a). The thickness of the entire collimator was 9 mm. The acceptance angle was different with that in the MC model, because the distances of beam-plane-to-pinhole and pinhole-to-CZT gamma camera were changed. The beam plane-to-collimator and the collimator-to-detector distance were 7.5 cm in the experiment. The cylindrically shaped 5 mm thick tungsten collimator was attached to the front window of the CZT gamma camera to shield photons leaking from the X-ray tube (Fig. 9). The inner diameter of the tungsten collimator was 6 cm. The detailed description of the CZT gamma camera was mentioned in II.1.1. The X-ray source to axis distance (SAD) was 50 cm, where the axis was defined as a line passing through the center of the pinhole and the CZT gamma camera. The geometrical efficiency, and the system resolution was calculated by (1) to (5). The FOV of this system was 4.8 cm in diameter.

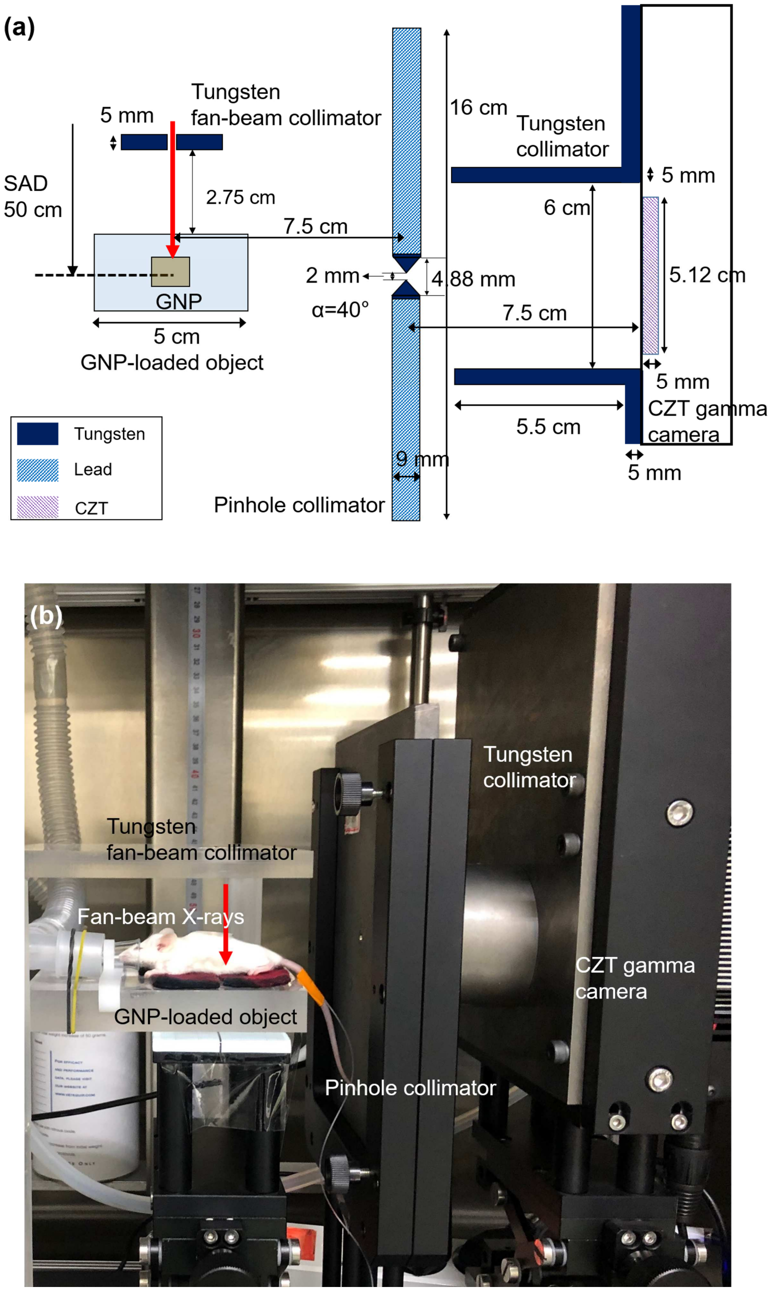

Fig. 9. (a) Schematic diagram and (b) photograph of pinhole K-shell XRF imaging system.

The filtered 140 kVp X-rays generated by X-RAD 320 were used to stimulate K-shell XRF photons from GNPs as recommended in the MC simulations (Fig. 5(b)). The current to the X-ray tube was determined to be 17 mA that did not exceed the maximum count rate for the CZT gamma camera (5.2×10^4 counts/sec for 1024 pixels). The X-RAD 320 has its adjustable collimator which users can control the radiation field size manually. However, by using the adjustable collimator, it was hard to generate a narrow sheet of fan-beam X-rays with a good reproducibility. Therefore, a tungsten fan-beam collimator was designed and manufactured (Korea Tungsten, Fig. 10). The tungsten fan-beam collimator with a 2 mm slit was used to generate the fan-beam having a thickness of 2.2 mm. The thickness of the tungsten fan-beam collimator was 5 mm. The beam profiles were measured by an XR-RV3 radiochromic film (Gafchromic®) as shown in Fig. 10(b). The film was located at the X-ray source to surface distance of 47.25 cm. The filtered 140 kVp X-rays irradiated the film for 10 min. Then, the film was scanned by an Epson 11000XL flatbed scanner by the reflection mode and analyzed by using a Verisoft 3.1 (PTW, Germany).

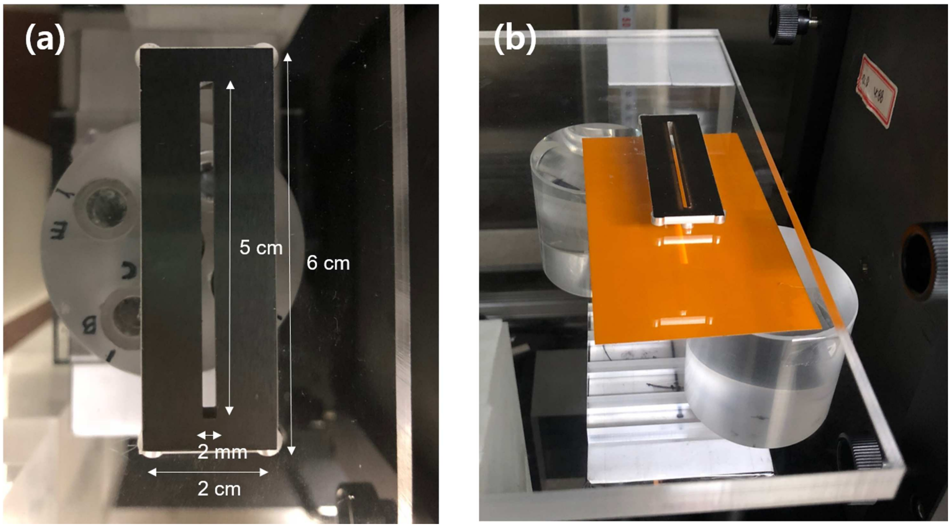

Fig. 10. Photographs of (a) the tungsten fan-beam collimator and (b) the experimental setup for the measurement of radiation field by using XR-RV3 radiochromic film.

The PMMA phantom of 2.5 cm diameter and 5 cm length was imaged to determine an optimal image acquisition time and to acquire a calibration curve to correlate GNP concentration to K-shell XRF counts (Fig. 11). In the phantom a 1.0 cm diameter hole was placed, where GNP columns having six different concentrations were inserted that were 0 wt%, 0.125 wt%, 0.25 wt%, 0.5 wt%, 1.0 wt%, and 2.0 wt%. 1.9 nm diameter GNPs (AuroVist, Nanoprobes Inc., NY, USA) were diluted with deionized water (DI water).[65] The GNP column had an inner diameter of 0.64 cm and an outer diameter of 1.0 cm. The height of GNP column was 1.0 cm.

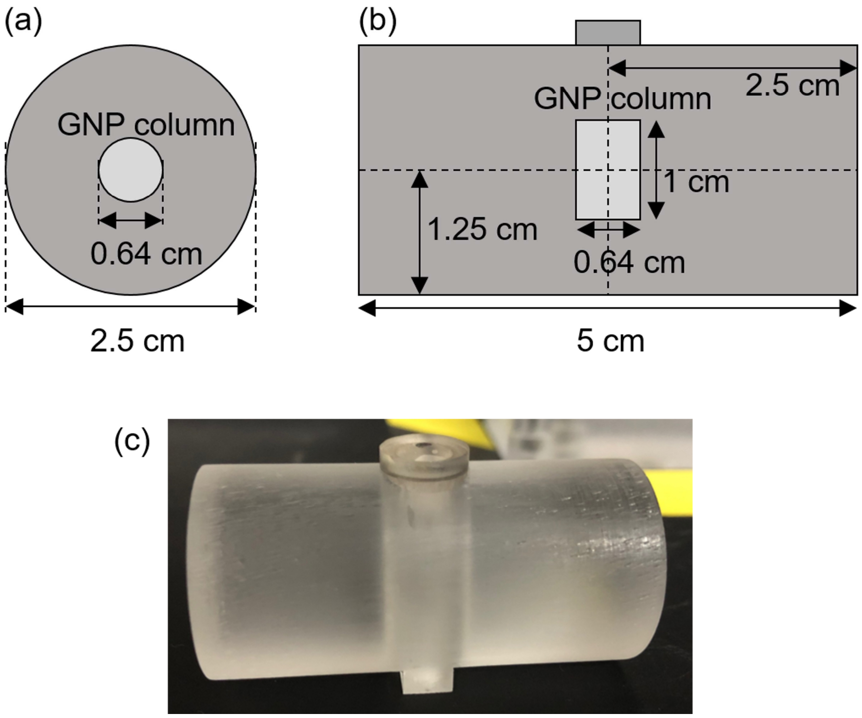

Fig. 11. Schematic illustrations of (a) top- and (b) lateral view of the imaging PMMA phantom. (c) Photograph of the imaging PMMA phantom.

II.2.2.2 *Measurement of K-shell XRF Signal*

The energy calibration of the CZT gamma camera was conducted by measuring gammas emitted from four different radio-isotopes that were Am-241 (Ortec, Oak Ridge, TN), Ba-133, Cd-109 and Co-57 (Type R, Eckert & Ziegler). The center of the radio-isotopes was aligned to the center of the CZT gamma camera by using a laser pointer. The gamma-rays were measured for 1 hour at room temperature at the radio-isotopes to detector distance of 5 cm. The number of channel bins was 256. All the photon counts from 1024 pixels were summed to generate one spectrum for each radio-isotope. Major photon emissions for the four radio-isotopes are listed in Table 3.[66]

Table 3. Major gamma emissions for Am-241, Ba-133, Cd-109 and Co-57.[66]

Nuclide	Major gamma emissions (keV)
Am-241	59.5 (36%)
Ba-133	81.0 (34.1%), 276 (7.2%), 303 (18.3%), 356 (61.9%), 384 (8.9%)
Cd-109	88.0 (3.6%)
Co-57	14.4 (9.2%), 122 (85.6%), 136.5 (10.7%)

According to Table 1, the most dominant K-shell XRF photons of Au have the energies of 67.2 keV and 69.0 keV. However, as will be described in III.1.1 and Fig. 18, due to the limitation of the energy resolution of the CZT gamma camera that was utilized in this investigation could not measure the two separate K-shell XRF peaks. Instead, one K-shell XRF peak from GNPs was shown at the energy window between 65.6 keV and 71.0 keV. As already presented in the MC study, the raw XRF signals were acquired by subtracting the photon counts of the K-shell XRF peak of the 0 wt% PMMA phantom from the counts of the same channels of the GNP-loaded PMMA phantom. The width of the channel windows was 4 channels (i.e., 5.4 keV in energy).

The raw K-shell XRF counts were then processed by the correction procedures that will be described in II.2.2.3. The methods to correct and account for the attenuation and the sensitivity were basically the same as in the MC study. Additionally, pixel-by-pixel channel windows for each pixel were selected by analyzing the measurement data that will be also mentioned in II.2.2.3. The negative raw K-shell XRF counts were considered to be zero.

Several pixels were observed to have large variations in the energy response. This abnormal difference in the photon counts might result in large noise in the K-shell XRF images. In particular, this affects the quality of images for low concentration of GNPs. In order to find the abnormal pixels, the photon counts scattered from a 0 wt% PMMA phantom were measured by the CZT gamma camera in three different days. The irradiations with 140 kVp X-rays to a PMMA phantom of 5 cm diameter and 5 cm height were conducted for 10 min in each day. The differences in the photon counts between the three measurements were analyzed. By using a Chauvenet's criterion, the abnormal pixels showing the large differences in the photon counts compared to the average differences between the three days' measurements were selected. The total number of the pixels in the FOV (i.e., 4.8 cm in diameter) was 764. For N = 764, the maximum permissible ratio of the deviation to standard deviation for the Chauvenet's criterion (i.e., τ) is 3.408. The values of the abnormal pixels whose τ_i is greater than 3.408 were then converted to the average value of the photon counts of the surrounding eight pixels (or five pixels when the abnormal pixel is located at the outermost in the FOV).

.

II.2.2.3 *Signal Processing: Correction Factors*

The attenuation correction method was already presented in the MC study as described in II.1.2. The attenuation for the incident X-ray and the K-shell XRF photons was considered by using the mass attenuation coefficient of PMMA published from NIST[63] as (9)

$$a_{CZT} = e^{\mu_I y_i} \times e^{\mu_K x_i} \qquad (9)$$

where a_{CZT} is the attenuation correction factor, μ_I is the linear attenuation coefficient of the PMMA at the incident X-ray energy, μ_K is the linear attenuation coefficient of the PMMA at K-shell XRF energy of Au (~68 keV). As shown in Fig. 12, y_i is the path length of the incident X-rays in the phantom, while x_i is the path length of the K-shell XRF photons of i^{th} pixel in the phantom. μ_I calculated by (7) was 0.1867 cm^{-1}, while μ_K was 0.2072 cm^{-1}.

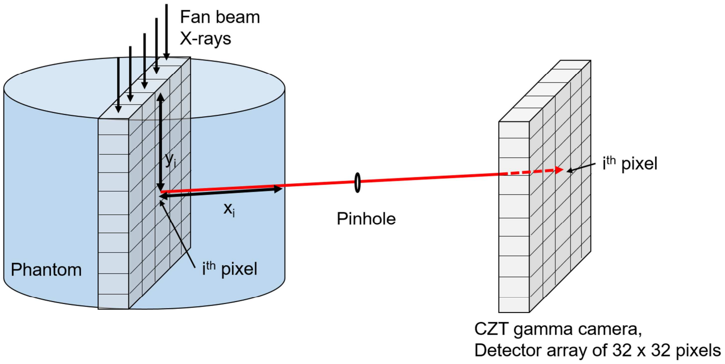

Fig. 12. Schematic illustration of pinhole XRF imaging system. The plane of PMMA phantom was divided into 32 × 32 pixels of each had 1.6 × 1.6 mm^2. y_i is the path length of incident X-rays in the phantom, while x_i is the path length of XRF photons of i^{th} pixel in the phantom.

As described in II.1.2, the decrease of the detection sensitivity of the peripheral pixels was calculated by the MC simulation. The cylindrically shaped tungsten collimators were attached to the virtual CZT gamma cameras on the both sides. A virtual source emitting 68 keV X-rays was defined to have 2 mm width and 5×5 cm^2 rectangular shape. In addition, the pinhole collimators were designed following the realistic geometry (i.e., the inner diameter of 2 mm with the acceptance angle of 40°) and material (i.e., tungsten and lead). The beam plane-to-collimator and the collimator-to-detector distances were 7.5 cm. The photon counts detected by each pixel of the detector were normalized against the maximum value among the pixels. The reciprocals of each value are the sensitivity correction factors. The sensitivity correction factors greater than 1.25 were assumed to be zero, since those pixels were out of the FOV (i.e., 4.8 cm in diameter).

Even in the uniform field of gammas, pixel-by-pixel photon counts measured by the CZT gamma camera showed quite large differences. This non-uniformity might be due to a defect of CZT crystal, a charge sharing effect, or electrical noise. In order to determine the correction factors for the pixel-by-pixel non-uniformity of the CZT gamma camera, a gamma emitting Cd-109 radio-isotope (Type R, Eckert & Ziegler) was used. The source to detector distance was 25 cm. Gamma rays emitted from the Cd-109 were measured by the CZT gamma camera for 41 hours at room temperature. The photon counts measured by each pixel of the detector were normalized against the maximum counts among the pixels. The reciprocals of each value are the pixel-by-pixel non-uniformity correction factors.

The total correction factors were calculated by the multiplication of the attenuation correction factors, the sensitivity correction factors and the pixel-by-pixel non-uniformity correction factors. By multiplying the total correction factors by the raw K-shell XRF counts, the corrected K-shell XRF counts were obtained. The corrected K-shell XRF counts were then treated for the Gaussian filter with $\sigma = 2$ of which matrix were 3×3 to decrease background noise of images.[67,68]

The effect of the scan time on the image quality of K-shell XRF images was investigated by varying the imaging time with 0.5 min, 1 min, 2 min, 3 min, and 5 min for the 0 wt% PMMA phantom and the 0.125 wt% PMMA phantom. Therefore, the total image acquisition times for one slice of a 2D image were from 1 min to 10 min. The measurements were repeated five times for each imaging time. The image qualities of K-shell XRF images for the 0.125 wt% GNP columns were assessed by CNRs. In order to acquire the calibration curve between the GNP concentrations and the corrected K-shell XRF counts, the measurements were repeated ten times for each GNP concentration with 1 min irradiation. The linear relationship between the GNP concentrations and the mean count number per pixel in ROIs was obtained. The ROI was the pixels projected by the GNP columns. Since the projected area of the GNP columns on the CZT gamma camera was 0.64×1.0 cm^2, the ROI had 4×6 pixels (i.e., 0.64×0.96 cm^2). The calibration curve was used to convert the corrected K-shell XRF counts to the concentration of GNPs for *in vivo* mice experiment that will be described in II.3.1 and III.3.

II.2.2.4 *Application of Convolutional Neural Network*

One of the limitation of the current imaging system is that the pre-scanning of the object (i.e., a scanning for the 0 wt% PMMA phantom in the phantom study) is necessary. In order to reduce the motion artifact caused by the inter-scanning positioning errors, the GNP-loaded object (i.e., the small animals) should be restrained at the same position during a full scanning period. If the interval between the scanning is too long to anesthetize the small animal (i.e., over than an hour), the inter-scanning positioning errors significantly affect the quality of the XRF images. Therefore, an application of convolutional neural network (CNN) was suggested to generate the XRF images, which only required the post-scanning.

The FOV for training the CNN was 3.2×3.2 cm^2 (i.e., 20×20 pixels). The 2.5 cm diameter PMMA phantom containing the 0.64 cm diameter GNPs columns of 0 wt%, 0.125 wt%, 0.25 wt%, 0.5 wt%, 1.0 wt% and 2.0 wt% was translated five times each for a horizontal direction and a vertical direction so that the XRF photons from GNPs could be measured at every pixel in the defined FOV. At each position, the phantom with 0 wt% GNPs (i.e., the pre-scanning) was irradiated twenty times, while the phantom with other concentrations of GNPs (i.e., the post-scanning) was irradiated ten times. The irradiation was performed for 1 min for each phantom. Among the measured data, 12,000 XRF images were used as a training dataset. These images were produced by the combination of randomly selected sixteen pre-scanning data and six post-scanning data at each position and concentration (i.e., 16 (pre-scanning) × 6 (post-scanning) × 25 (position) × 5 (concentration) = 12000). Both validation dataset and test dataset had 500 XRF images each (i.e., $2 \times 2 \times 25 \times 5 = 500$). The XRF images of validation and test dataset were not included in the training dataset. All the measured data were treated for the sensitivity correction and the pixel-by-pixel non-uniformity correction.

After the dataset preparation, the 2D CNN was built to generate XRF images without the pre-scanning. The schematic diagram of the architecture of the 2D CNN is shown in Fig. 13. In the training stage, the images of the post-scanning data were fed into the model as inputs, while XRF images generated by the subtraction between the pre- and post-scanning data were targets. The network was trained by a supervised manner with a combination of mean squared error and structural similarity loss. The number of epoch was 500 and the network was validated with the validation dataset after each epoch. The best model was updated and saved when the mean squared error of the ROI between output and target was less than the previous epoch. The ROIs were selected as 3×3 pixels neighboring the maximum pixel values in each XRF image. Four GPUs (Nvidia Tesla V100) were utilized for an efficient training. After the training stage, the evaluation of the trained network was performed with the test dataset.

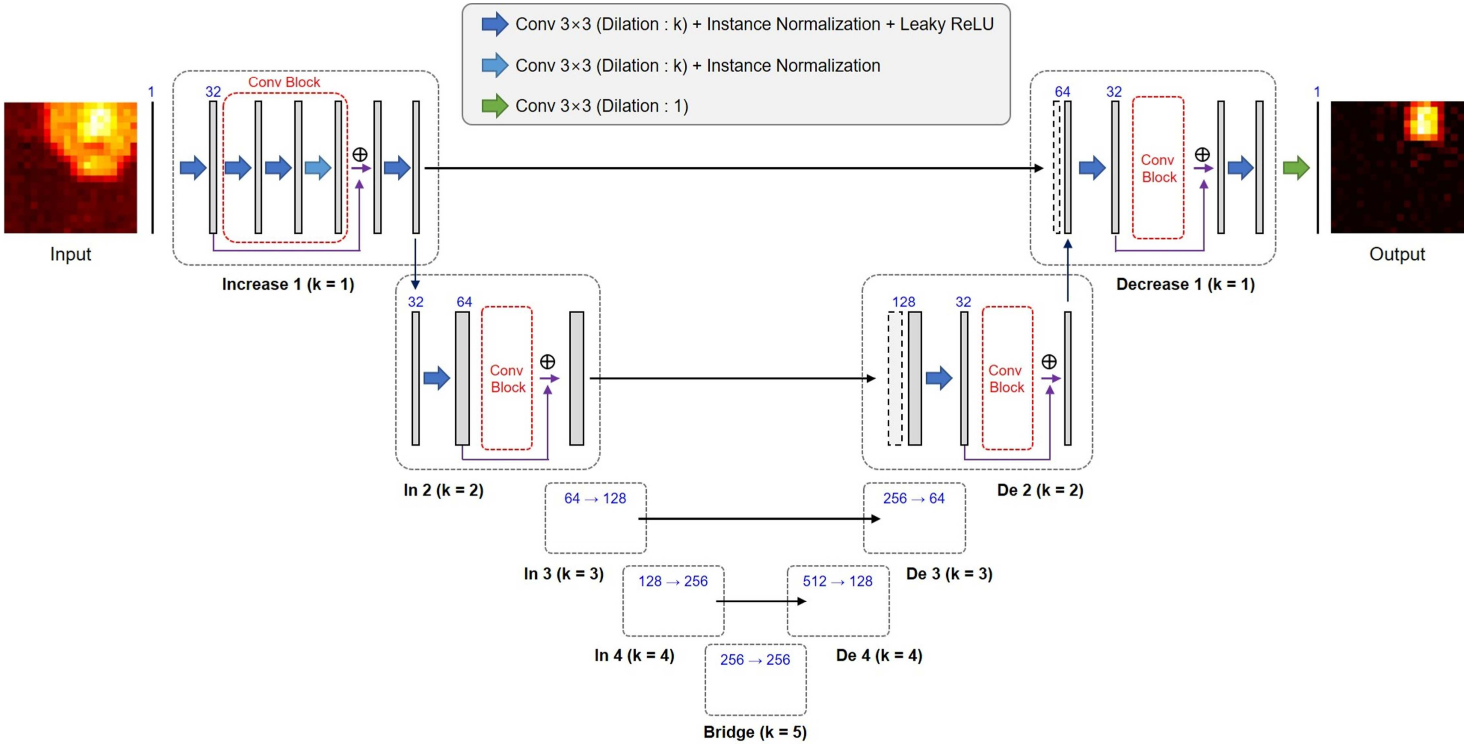

Fig. 13. An illustration of the architecture of 2D CNN to generate XRF images without pre-scanning.

II.2.3 K-shell XRF Detection System

II.2.3.1 *Experimental Setup*

Since the K-shell XRF detection system is used simultaneously with the pinhole K-shell XRF imaging system, the characteristics of incident X-rays were exactly the same as they were described in II.2.2.1. The experimental setup for the K-shell XRF detection system is shown in Fig. 14. A cylindrical lead collimator of 4.0 cm diameter and 9.0 cm height having a parallel hole of 0.25 cm diameter along its central axis was designed and manufactured to minimize the unwanted scattered photons reaching the CdTe detector. The collimator was located 14.0 cm from the beam plane. The CdTe detector and the collimator were perpendicular to the beam direction. The front window of the CdTe detector was located at 0.35 cm behind the front part of the collimator. The CdTe detector has a Be window of 100 μm, the CdTe crystal of $3 \times 3 \times 1$ mm^3. The energy calibration of the detector was conducted by using three dominant K-shell XRF peaks from 2.0 wt% GNPs ($K_{\alpha 2}$: 67.2 keV, $K_{\alpha 1}$: 69.0 keV and $K_{\beta 1}$: 78.2 keV). The number of channels was 1024. The dimension of the PMMA phantom and GNP columns was the same as it was described in II.2.2.1. The concentration of GNPs ranged from 0.125 wt% to 2 wt%. The irradiation was performed 1 min and repeated ten times for each concentration.

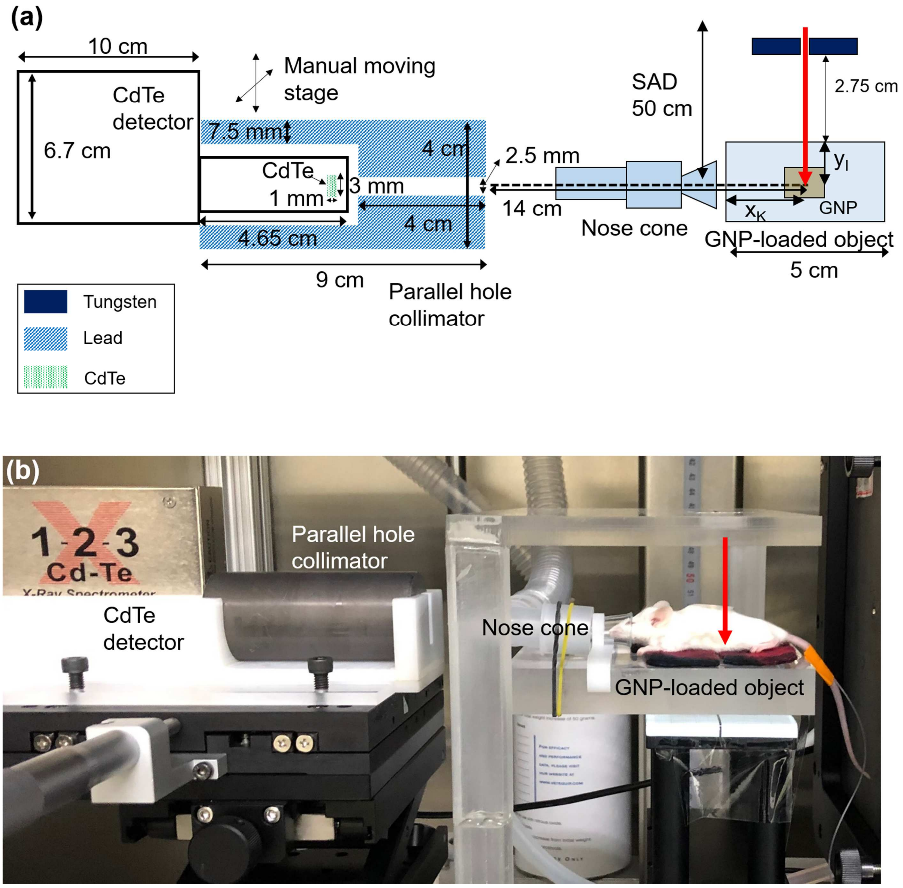

Fig. 14. (a) Schematic illustration and geometrical dimensions for experimental setup and (b) photograph of K-shell XRF detection system for an *in vivo* experiment.

II.2.3.2 *Signal Processing*

For acquiring the calibration curve between the GNP concentrations and the K-shell XRF photons emitted from the GNPs, the nose cone that was needed for anesthesia of mice (as will be described in II.3.1) was removed. The CdTe detector and the parallel hole collimator was aligned to the center of the GNP column inserted PMMA phantom. Three discrete K-shell XRF peaks were observed at channel number 453, 465 and 527. The most dominant two peaks at 453 and 465 were K_{α} XRF peaks of 67.2 keV and 69.0 keV. In order to estimate the Compton scattered photon counts under the K-shell XRF photons, thirty data points from the off-peak ranges of 62.12–64.21 keV, and 69.57–71.65 keV were selected. By using a linear interpolation, the background curve for Compton scattered photons was acquired. The K-shell XRF photon counts were determined to be the subtraction between the photon counts from GNP-loaded PMMA phantom and the generated background curve within the energy range of 64.21–71.65 keV. The attenuation correction for the K-shell XRF counts measured by the CdTe detector was take into account as (10)

$$a_{CdTe} = \frac{\exp(-\mu_{I,PMMA} \times y_{ref})}{\exp(-\mu_{I,m} \times y_{I})} \times \frac{\exp(-\mu_{K,PMMA} \times x_{ref})}{\exp(-\mu_{K,m} \times x_{K})} \times (\text{nose cone factor}) \quad (10)$$

where a_{CdTe} is the attenuation correction factor for the CdTe detector. The first term corrected the attenuation of incident X-rays in material, m, while the second term corrected the attenuation of XRF photons in the material, m. y_{ref} and x_{ref} are 1.25 cm and 2.5 cm, respectively. y_{I} and x_{K} are the path lengths for incident

X-rays and K-shell XRF photons in phantom (Fig. 14(a)). $\mu_{I,PMMA}$ and $\mu_{K,PMMA}$ are the linear attenuation coefficient of PMMA for incident X-rays and K-shell XRF photons, respectively. $\mu_{I,m}$ and $\mu_{K,m}$ are the linear attenuation coefficient of m for incident X-rays and K-shell XRF photons, respectively. For this study, m was PMMA so that the linear attenuation coefficient of m for incident X-rays and K-shell XRF photons were the same as the PMMA. After the attenuation correction factor was applied to the raw K-shell XRF photons, the linear relationship between the GNP concentration and the corrected K-shell XRF counts was acquired. The error bars were $1.96\sigma_{XRF}^{CdTe}$ (i.e., 95% confidence interval, CI) where σ_{XRF}^{CdTe} is the standard deviation of the corrected K-shell XRF counts from ten measurements. In addition, the attenuation corrections due to the nose cone (denoted as nose cone factor) along the beam path of XRF photons was considered. The nose cone factor was calculated by the ratio of the K-shell XRF count with the nose cone and without the nose cone for 0.5 wt% GNP-loaded phantom as (11).

$$\text{Nose cone factor} = \frac{K\!-\!shell\ XRF\ counts\ without\ nose\ cone}{K\!-\!shell\ XRF\ counts\ with\ nose\ cone} \quad (11)$$

II.2.4 L-shell XRF Detection System

II.2.4.1 *Experimental Setup*

For the measurement of *ex vivo* L-shell XRF photons, 40 kVp X-rays generated by X-RAD 320 were used as the excitation source. The 40 kVp X-rays were filtered with Al 2 mm. The tungsten fan-beam collimator was removed so that the incident X-rays fully covered the vials. The current to the X-ray tube was 10 mA. The SDD was placed perpendicular to the beam direction (Fig. 15). The front window of SDD was located 3 cm from the center of vials. The SDD had a Be window of 12.5 µm, a Si crystal of 0.5 mm thickness and 2.82 mm diameter. The peaking time of the SDD was 3.2 µs. Under this measurement setup, the SDD has an energy resolution in the range of 0.135–0.140 keV FWHM at 5.9 keV, while the maximum count rate is expected to fall in the range from 1×10^5–2×10^5 counts/sec according to the specifications by the manufacturer.[69]

The energy calibration of the SDD was performed by using three dominant L-shell XRF peaks from 2.0 wt% GNPs ($L_{\alpha 1}$: 9.71 keV, $L_{\beta 1}$: 11.48 keV and $L_{\gamma 1}$: 13.42 keV). The number of channels was 2048. 2.34 µg, 9.38 µg, 37.5 µg, 75 µg, 150 µg and 300 µg of GNPs stirred into 30 mg of DI water (0.0078 wt%–1.0 wt% GNPs) were used for a calibration curve between the mass of GNPs and the L-shell XRF counts. The vials for the calibration had an inner diameter of 5 mm and an outer diameter of 8 mm. The irradiation was performed 5 min and repeated five times for each vial.

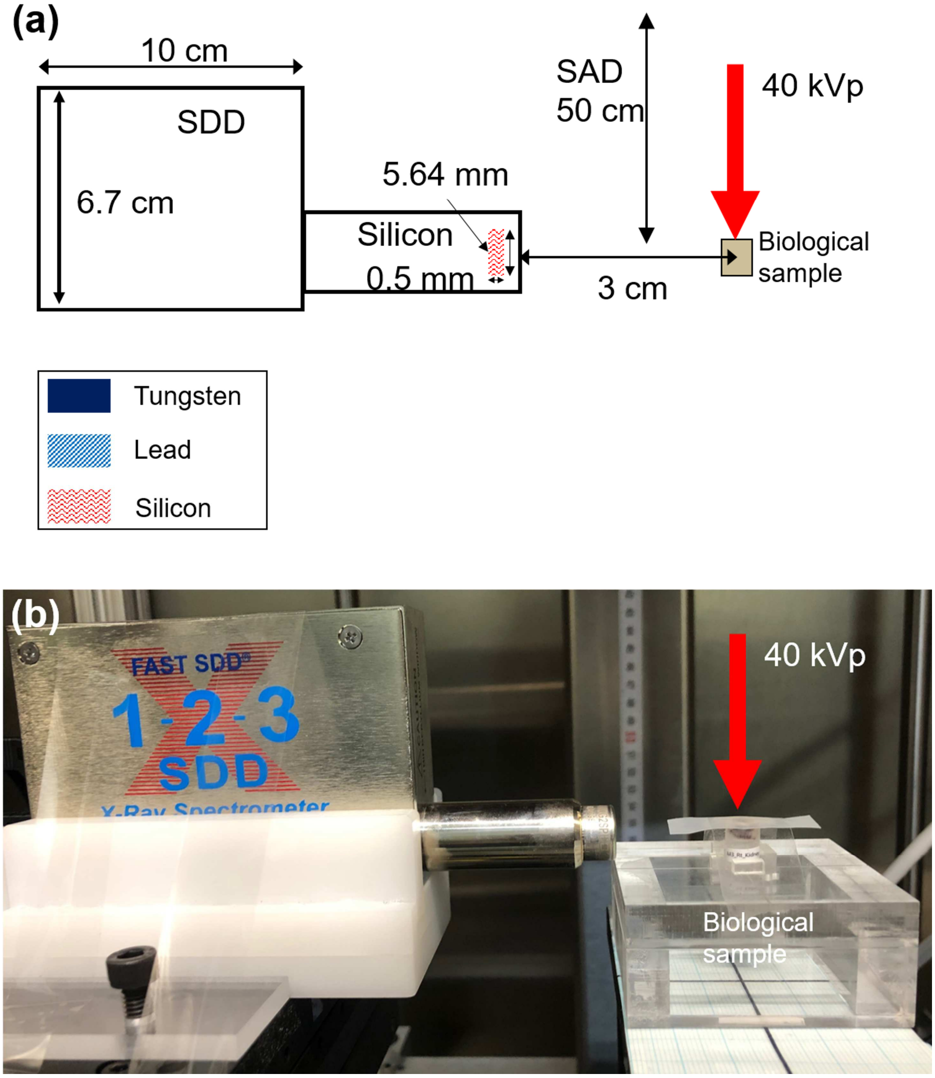

Fig. 15. (a) Schematic illustration and geometrical dimensions for experimental setup and (b) photograph of the L-shell XRF detection system.

II.2.4.2 *Signal Processing*

The three discrete L-shell XRF peaks were observed at channel number 405, 477 and 557. The most dominant two peaks at 405 and 477 were $L_{\alpha1}$ XRF peak of 9.71 keV and $L_{\beta1}$ XRF peak of 11.48 keV. A sum of the two L-shell XRF peaks was used to create the calibration curve. In order to generate a background curve for discriminating $L_{\alpha1}$ XRF peak, data points from the off-peak ranges of 9.08–9.32 keV, and 9.96–10.10 keV were selected. By using a linear interpolation, the background curve was acquired under $L_{\alpha1}$ XRF peak. The $L_{\beta1}$ XRF peak from GNPs was allowed to overlap with K_{α} XRF peak of Br. This peak might have been generated from the head geometry of the SDD. For the discrimination of the $L_{\beta1}$ XRF peak, a Gaussian function was applied to mimic the shape of the K_{α} XRF peak of Br. Pure $L_{\beta1}$ XRF counts from GNPs was extracted by subtracting the generated Gaussian background curve from the overlapped $L_{\beta1}$ XRF peak (Fig. 16).

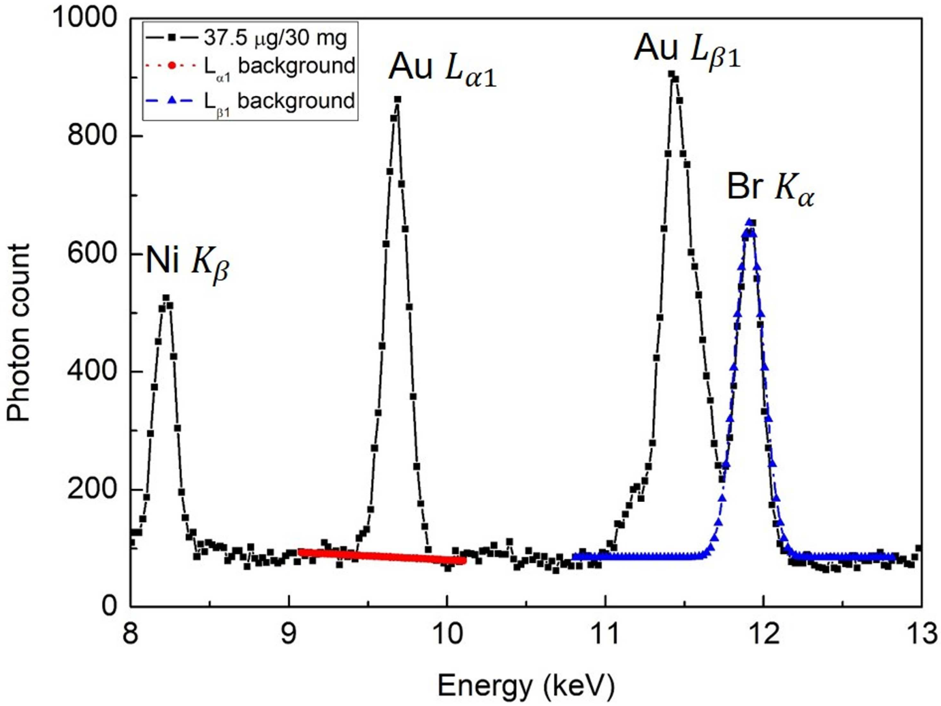

Fig. 16. The energy spectrum measured for 37.5 μg/30 mg GNPs (a solid line with squares). The generated background curves for discrimination of $L_{\alpha 1}$ and $L_{\beta 1}$ XRF peaks were indicated as circles and up-pointing triangles, respectively.

II.3 *In vivo* Study in Mice

II.3.1 Experimental Setup

The three mice were 6 week old female Balb/C, weighing 15–17 g ($N = 3$). All experiments were conducted in accordance with the protocols and guidelines approved by the Seoul National University Institutional Animal Care and Use Committee. 1.9 nm diameter GNPs (AuroVist, Nanoprobes Inc., NY, USA) were prepared according to the instruction provided by the manufacturer. The 40 mg of GNPs was suspended in 0.2 mL phosphate-buffered saline solution. The mice were anesthetized with isoflurane gas via inhalation for about an hour. They were restrained in a prone position and three slices of abdomen for each mouse were set to the light field of the fan-beam of X-RAD 320 (Fig. 17). Before the injection of the GNP-containing solution, pre-scanning of each mouse was performed for 1 min for each slice. The thickness of the slice was 2 mm. Following the pre-scanning, the GNP-containing solution was injected into the mice via a tail vein. Subsequent to the injection of GNP-containing solution, the mice were scanned at T = 0, 10, 20, 30, 45, and 60 min. At every time point, the post-scanning was performed for 1 min for each slice. The correction factors including the attenuation correction, the sensitivity correction and the pixel-by-pixel non-uniformity correction were multiplied to the raw XRF counts. It was assumed that the linear attenuation coefficient along the beam path in the mice was the same as that of the cylindrical water phantom. The 3×3 Gaussian filter was then applied to the image to reduce the background noise.

After T = 60 min, the mice were euthanized via CO_2 inhalation and left and right kidneys, spleen, liver, and blood from the three mice were extracted. The total number of tissue samples was 15, while 3 organs of each type listed above were extracted. The extracted organs were then excised into small pieces whose diameters were less than 3 mm. The masses of excised organs were measured to calculate the concentration. The L-shell XRF detection system with 40 kVp X-rays was used to measure the L-shell XRF photons emitted from the samples. The irradiation time was 5 min and the measurement was repeated three times for each sample. ICP-AES was again used to measure the mass of GNPs within the same excised organs. The correlation between the concentrations of all excised organs ($n = 15$) measured by the L-shell XRF detection system and ICP-AES was assessed by Pearson correlation coefficient. In addition, the mean and standard deviations of the measured concentrations of the tissue samples ($n = 15$) from the three mice ($N = 3$) were also compared.

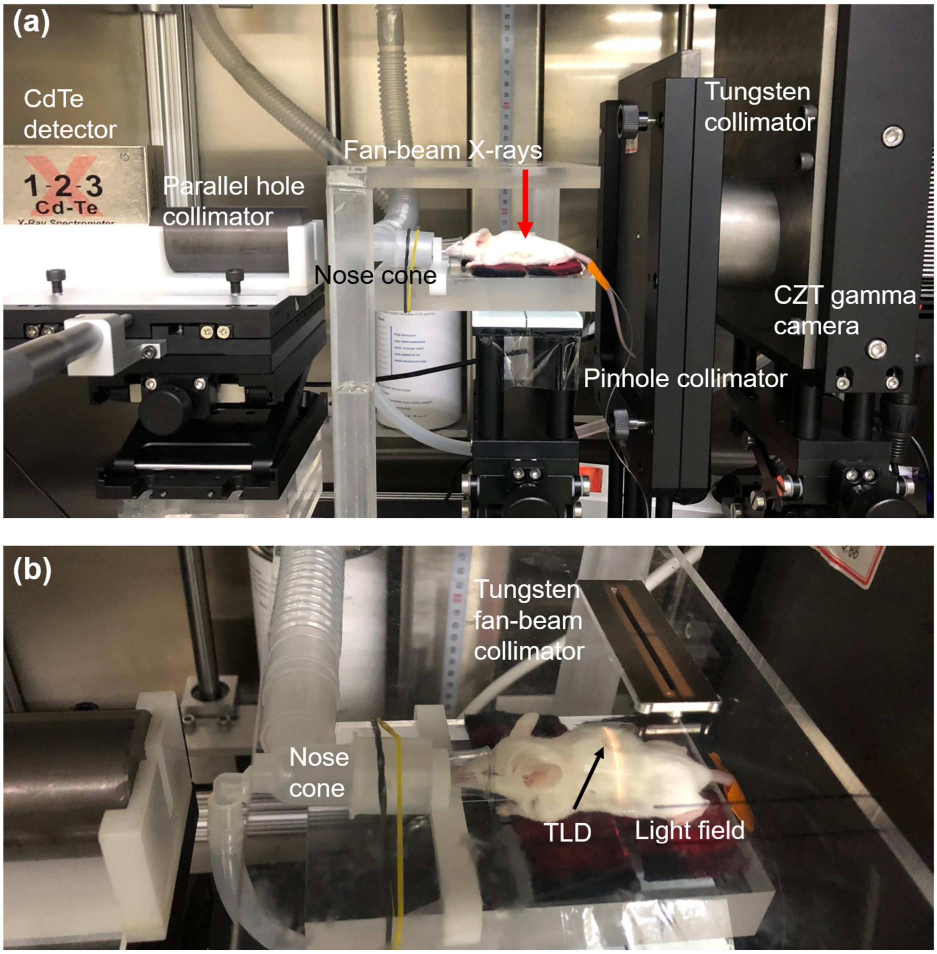

Fig. 17. (a) Experimental setup of *in vivo* pinhole K-shell XRF imaging system and K-shell XRF detection system. (b) Photograph of the tungsten fan-beam collimator, the light field and the TLD attached to the skin of mouse.

II.3.2 Dose Measurement

In order to measure the radiation dose delivered to the skin of the mice during the imaging interval, TLD-100 detectors (Harshaw, Thermo Fisher Scientific, denoted as TLD) were used. The TLDs were calibrated by the filtered 140 kVp of X-RAD 320. The reference dosimetry was performed by following the TG-61 in-air measurement protocol with a 0.6cc farmer-type ion chamber (30013, PTW, Germany).[70] The TLDs were attached to the skin of the mice where indicated by light field (Fig. 17(b)). After the irradiation, the TLDs were read out by a TLD Reader (Harshaw 3500, Thermo Fisher Scientific).

CHAPTER III. RESULTS

III.1 Monte Carlo Model

III.1.1 Geometric Efficiency, System and Energy Resolution

Since the energies of K-shell XRF photons of Gd and Au were relatively low (Gd: ~43 keV, Au: ~68 keV), the effective pinhole diameter was almost same as the physical pinhole diameter which means that there was no significant penetration effect in the edge of aperture. The geometric efficiency depends on the angle, θ. The geometric efficiency was 1.65×10^{-3} for the minimum angle (i.e., 0°) and 5.03×10^{-4} for the maximum angle (i.e., 47.7°). The collimator and intrinsic resolutions were 3.90 mm and 1.60 mm, respectively. The imaging system had the system resolution of 4.22 mm.

From the measurement of Am-241 photon peak at 59.5 keV, %FWHM of the detector was determined to be 18.6% (i.e., 11.1 keV) (Fig. 18). According to this %FWHM, the original MC spectra of 1 keV energy bin were degraded by using the Gaussian distribution (MATLAB 2014a, MathWorks, Inc.).

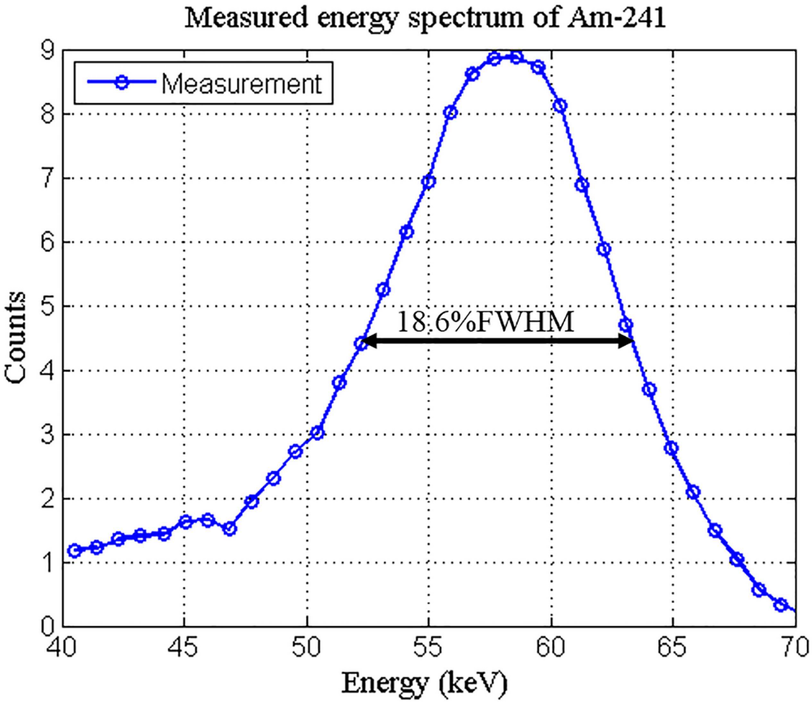

Fig. 18. The energy spectrum of Am-241 acquired with the CZT gamma camera.

III.1.2 K-shell XRF Image by Monte Carlo Simulations

Fig. 19 illustrates the simulated spectra of the central pixel for 0.09 wt% Gd column region irradiated by the three different X-rays. The two green curves of Fig. 17 were obtained by degrading the original MC spectra (two red curves of Fig. 19) of 110 kVp according to the measured %FWHM of 18.6%. The XRF peaks of $K_{\alpha 2}$ and $K_{\alpha 1}$ are shown to be a single peak due to their close energies (red arrow of Fig. 19). The X-rays of 51 keV induced more Compton background photons than the X-rays of 60 keV and 110 kVp. The X-rays of 60 keV and 110 kVp showed very similar XRF and Compton photon counts in Fig. 19(b), which means that 110 kVp with a tungsten filter could replace monochromatic X-rays. In Fig. 19(b), the energy window of A was used to acquire images for 1 keV-energy resolved detector, while the energy window of B for 18.6% FWHM-treated detector. Fig. 20 shows Compton scattered photon count maps and 2D pinhole K-shell XRF images of Gd. Compton background photons by 51 keV X-rays were mainly from the region of 0.06 wt% Gd column or nearby (see also Fig. 4). The white dashed arrow in Fig. 20(e) shows decreased XRF signals caused by a large amount of Compton background (backward-scattered photons). Even Gd columns of 0.01 wt% (i.e., lowest concentration) were detectable in all XRF images.

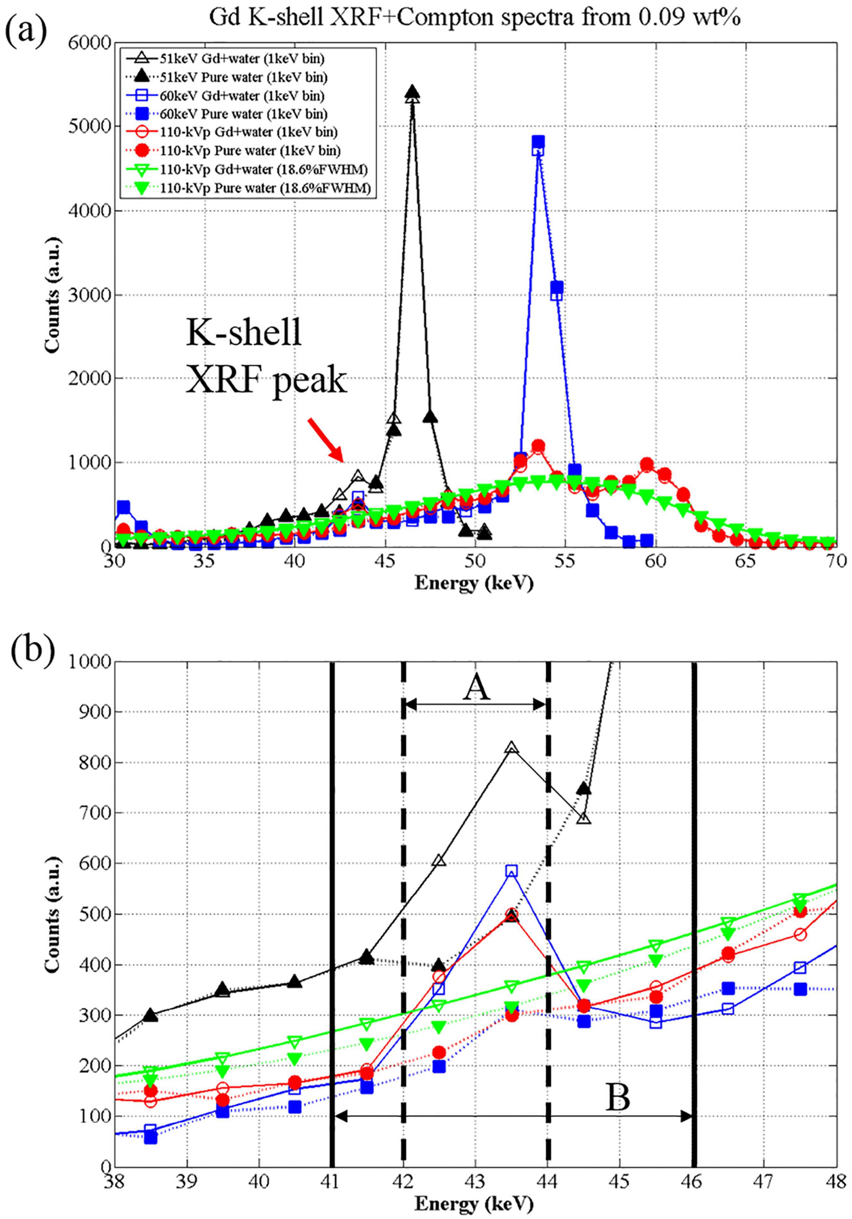

Fig. 19. Energy spectra of K-shell XRF and Compton scattered photons from 0.09 wt% of Gd column; (a) energy spectra of 30 to 70 keV and (b) energy spectra of 38 to 48 keV focusing on the range of K-shell XRF energy.

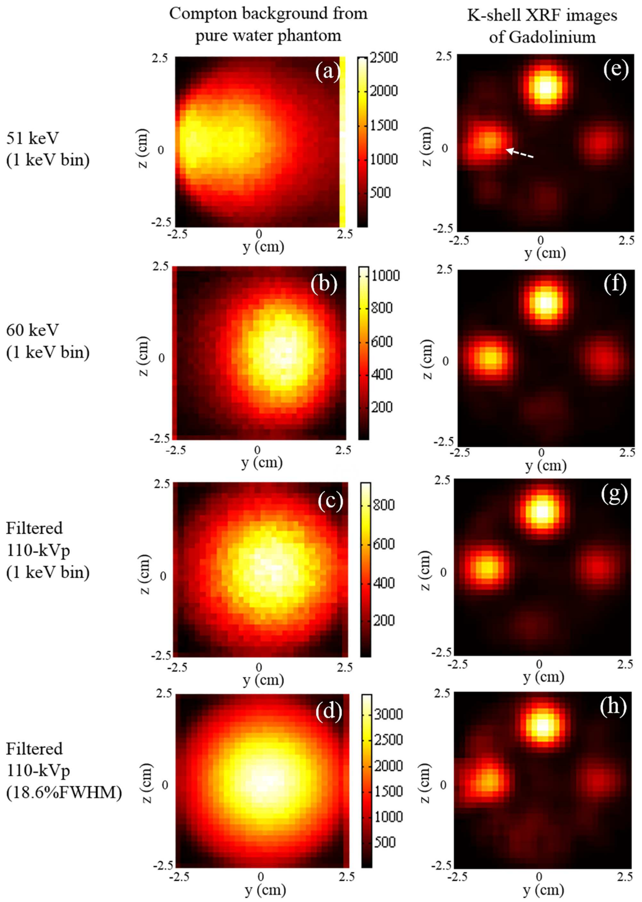

Fig. 20. Images of (a)-(c) with X-ray energies: Compton background photon images from a pure water phantom. Images of (e)-(g) with X-ray energies: Pinhole K-shell XRF for four gadolinium columns. Images of (d) and (h) showed Compton backscattered photons and pinhole XRF photons of 110 kVp degraded by 18.6% FWHM. A fan-beam of X-rays was incident on the phantom from the left side of each image. Gd-columns of 0.01 wt%, 0.03 wt%, 0.06 wt% and 0.09 wt% were shown in bottom, right, left and top, respectively. The white dashed arrow in (e) showed the decreased XRF signals due to a large amount of Compton background photons.

The linear relationship between XRF signals and Gd concentrations was plotted in Fig. 21. In Fig. 21(a), all curves for three incident X-rays show a strong linearity (i.e., $R^2 > 0.98$). This also implied that the corrections for the attenuation and sensitivity worked well. The CNRs of the Gd columns calculated from pinhole K-shell XRF images are shown in Fig. 21(b). There was no significant difference in CNRs of 51 keV and 60 keV images except for 0.09 wt% Gd column. All the CNRs of 110 kVp X-ray images acquired by 1 keV-energy resolved detector were lower than those in monochromatic X-rays. The CNR of 110 kVp image of 1 keV-energy bin had the lowest value of 4.6 for 0.01 wt% Gd column, which was larger than the value of 4 as the recognizable limit according to the Rose criterion. Although some blurring noise of 110 kVp images of 18.6% FWHM-degraded detector appeared, their CNRs were similar or even higher than those of the images of 1 keV-energy resolved detector.

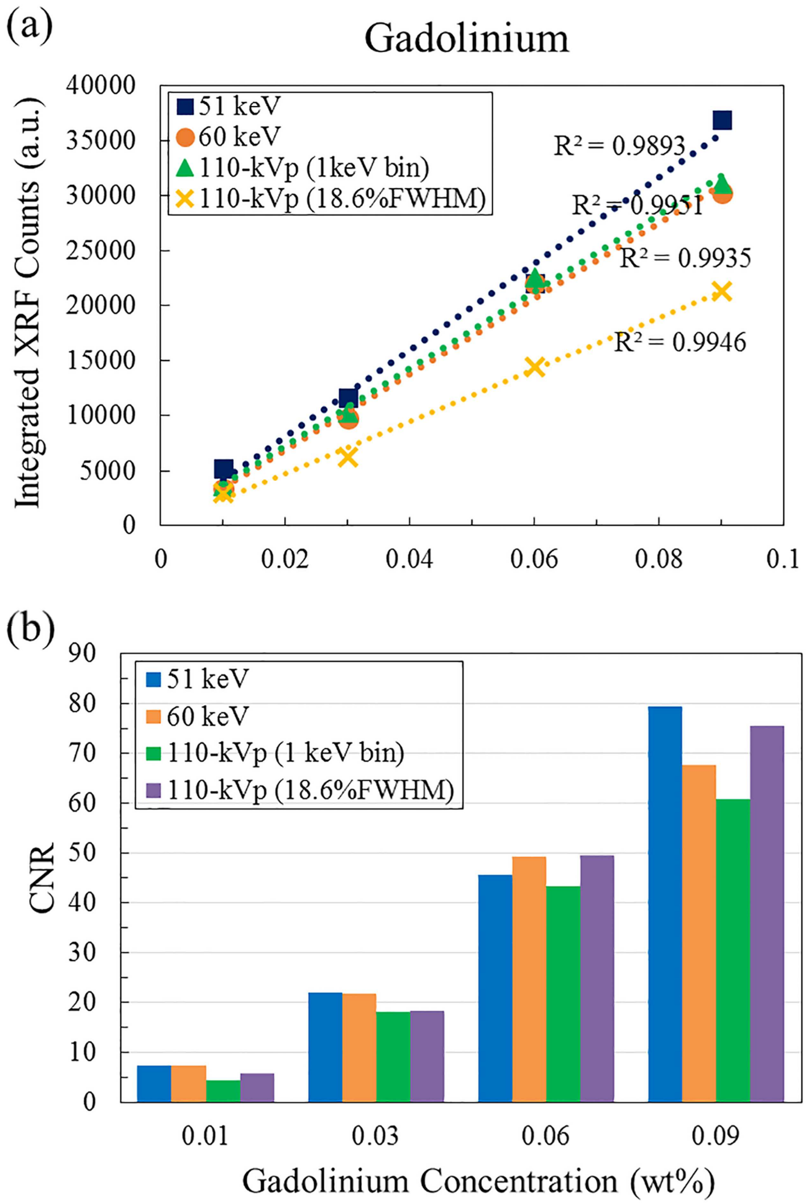

Fig. 21. (a) Linear relationship between gadolinium concentrations and integrated XRF counts. (b) CNR values in the region of gadolinium columns for three different X-ray source spectra.

The two peaks of $K_{\alpha 2}$ and $K_{\alpha 1}$ XRF photons from 0.09 wt% Au column were clearly discerned from Compton background in the spectra of 1 keV-energy resolution detector (as shown in Fig. 22). Although the XRF peaks in the degraded spectrum (empty green triangles in Fig. 22(a) and 22(b)) were broadened and barely shown, they had higher photon counts than the corresponding photon counts in the spectrum of pure water phantom (solid green triangles in Fig. 22(c)). The X-rays of 81 keV generated large Compton background counts in the range of K-shell XRF energies, while the X-rays of 95 keV had the lowest background counts among the three incident X-rays. In Fig. 22(c), the energy window of A was used to acquire images for 1 keV-energy resolved detector, while the energy window of B for 18.6% FWHM-treated detector. Fig. 23 illustrates Compton scattered photon count maps and 2D pinhole K-shell XRF images of Au. In Fig. 23(a), there was a region of very strong Compton scattered photons. In addition, background photon counts generated from 81 keV X-rays was about 6 to 10 times higher than those from 95 keV and filtered 140 kVp. The white arrows in Fig. 23(e) indicated the Compton-scattered noise caused by those strong background photons scattered by 81 keV X-rays.

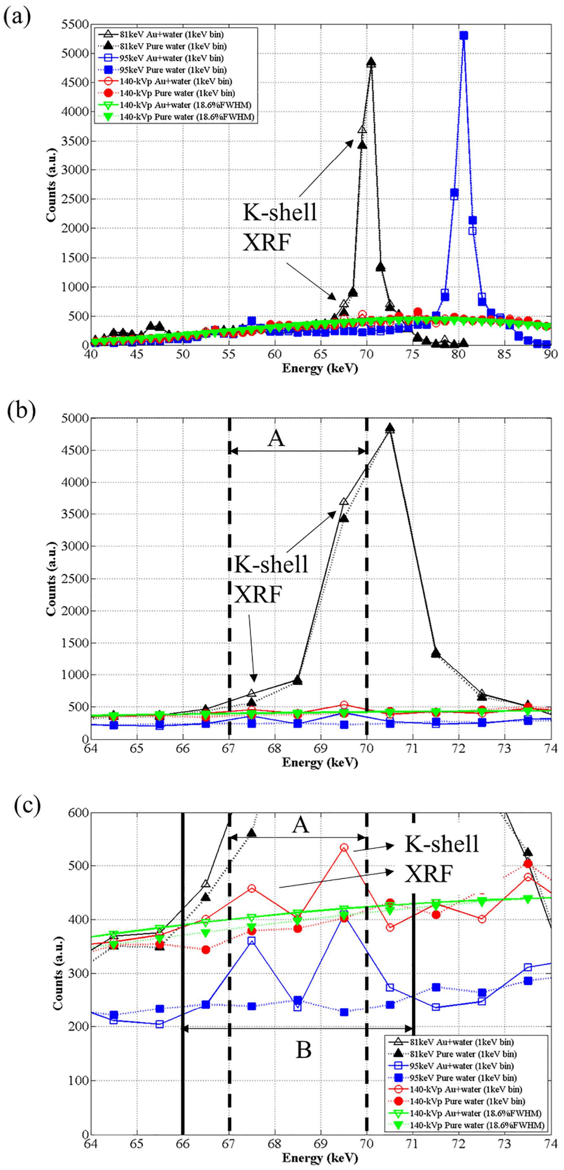

Fig. 22. Energy spectra of K-shell XRF and Compton scattered photons from 0.09 wt% of Au column; (a) energy spectra of 40 to 90 keV, (b) energy spectra of 64 to 74 keV focusing on the range of K-shell XRF energy, and (c) energy spectra of 64 to 74 keV in range of photon counts under 600.

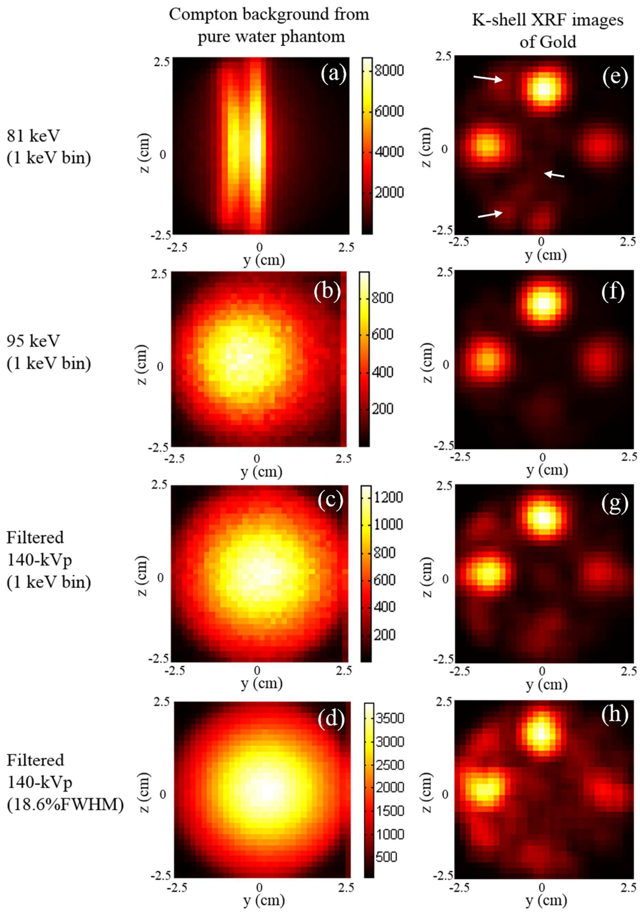

Fig. 23. Images of (a)-(c) with X-ray energies: Compton background photon counts from pure water phantom. Images of (e)-(g) with X-ray energies: Pinhole K-shell XRF images of four gold columns. Images of (d) and (h) showed Compton backscattered photons and pinhole XRF photons of 140 kVp degraded by 18.6% FWHM. A fan-beam of X-rays was incident on the phantom from the left side of each image. Au-columns of 0.01 wt%, 0.03 wt%, 0.06 wt% and 0.09 wt% were shown in in bottom, right, left and top, respectively. The white arrows in (e) showed the background noise signals due to a large amount of Compton background photons.

All three incident X-rays showed good linear relationships (R^2 > 0.9162) between the integrated XRF signals and the concentrations of Au (Fig. 24(a)). As XRF signals were degraded by 18.6% FWHM, the linearity was also decreased, having R^2 of 0.92. The image quality of filtered 140 kVp of 1 keV-energy resolved detector seemed to be in the similar level with 81 keV images. All the CNRs of 81 keV image were the much lower than those of 95 keV images because Compton-scattered photons spoiled the image quality in the background region. 95 keV X-rays could avoid direct Compton scattered photons so that their images showed the lowest level of background photons and the highest CNRs. The CNRs of 0.01 wt% Au columns were 1.7 and 6.4 in 81 keV and 95 keV images, respectively (Fig. 24(b)). For 140 kVp X-rays, according to Rose criterion of CNR, the lowest distinguishable concentrations were 0.01 wt% in 1 keV-resolution images and 0.03 wt% in 18.6% FWHM images (Fig. 24(b)).

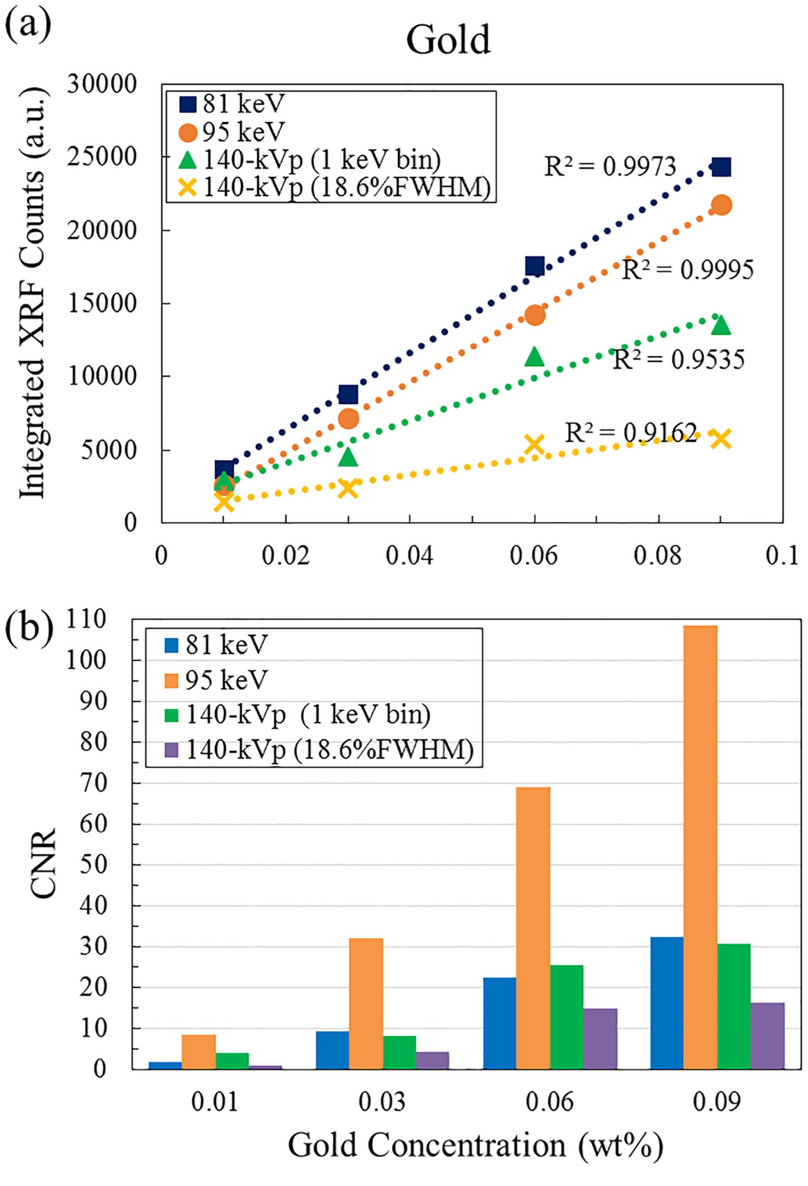

Fig. 24. (a) Linear relationship between gold concentrations and integrated XRF counts. (b) CNR values in the region of gold columns for three different X-ray source spectra.

III.1.3 Radiation Dose

The imaging doses of the pinhole XRF imaging system are summarized in Table 4. These radiation doses were calculated for 1 × 10^{11} histories of incident X-rays, which was also the number of histories to acquire all the images shown before. The radiation doses with metal elements in the phantom were a little higher (by 0.1 mGy) than those of pure water phantom. The total imaging doses could be the sum of these two components, when additional information on background photon counts was necessary. Thus, XRF imaging of polychromatic X-rays required 19.9 mGy for Gd and 26.1 mGy for Au. In the experiment, imaging time depends on the X-ray tube voltage and current, and the source-to-phantom distance.

Table 4. Imaging dose for pinhole XRF imaging calculated by MC simulations.

Incident X-rays	Average dose (mGy)		
	Pure water	Gd/Au NPs loaded water phantom	Sum
51 keV	10.1	10.2	20.3
60 keV	9.5	9.6	19.1
110 kVp	9.9	10.0	19.9
81 keV	10.6	10.7	21.3
95 keV	12.2	12.3	24.5
140 kVp	13.0	13.1	26.1

III.2. Development of Pinhole XRF Imaging System

III.2.1 Pinhole K-shell XRF Imaging System

III.2.1.1 *Energy Calibration and Measurement of Field Size*

The energy spectra of Am-241, Ba-133, Cd-109 and Co-57 are shown in Fig. 25(a) and 25(b). Five discrete photo-peaks; 59.5 keV, 81.0 keV, 88.0 keV, 122 keV and 276 keV from Am-241, Ba-133, Cd-109, from Co-57 and Ba-133 were measured. A linear relationship between the channel number and the energy was described in Fig. 25(c). The linear regression curve had a slope of 1.8095 and an y-intercept of -12.223, having $R^2 > 0.99$. One channel corresponded to 1.8095 keV and the minimum detectable energy was about 35 keV, while the maximum energy was about 285 keV.

Fig. 26 shows the irradiated XR-RV3 film and measured profiles of fan-beam X-rays. The pixel values were normalized to the central position of the film. The beam width in x-direction was measured to be 2.2 mm as shown in Fig. 26(c).

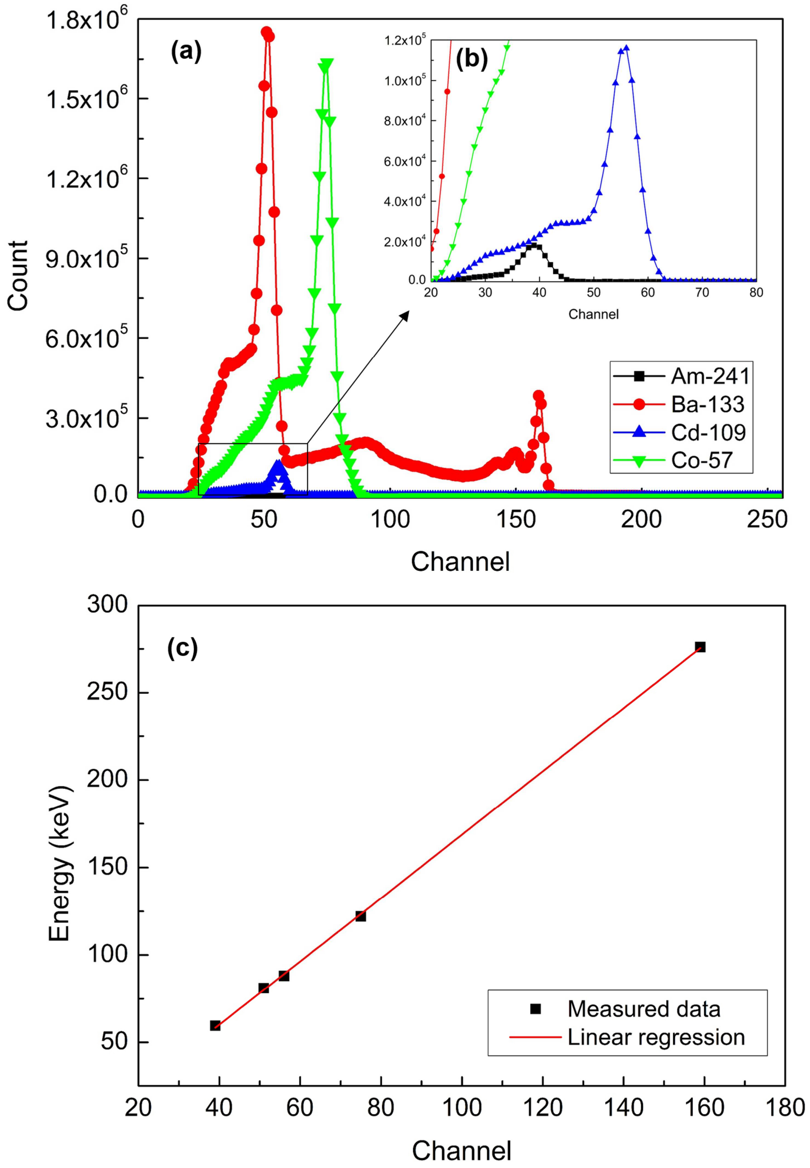

Fig. 25. (a) Measured photon spectra of Am-241, Ba-133, Cd-109 and Co-57 and (b) its magnified image showing channel from 20 to 80. (c) The linear regression fitting curve between channel and energy.

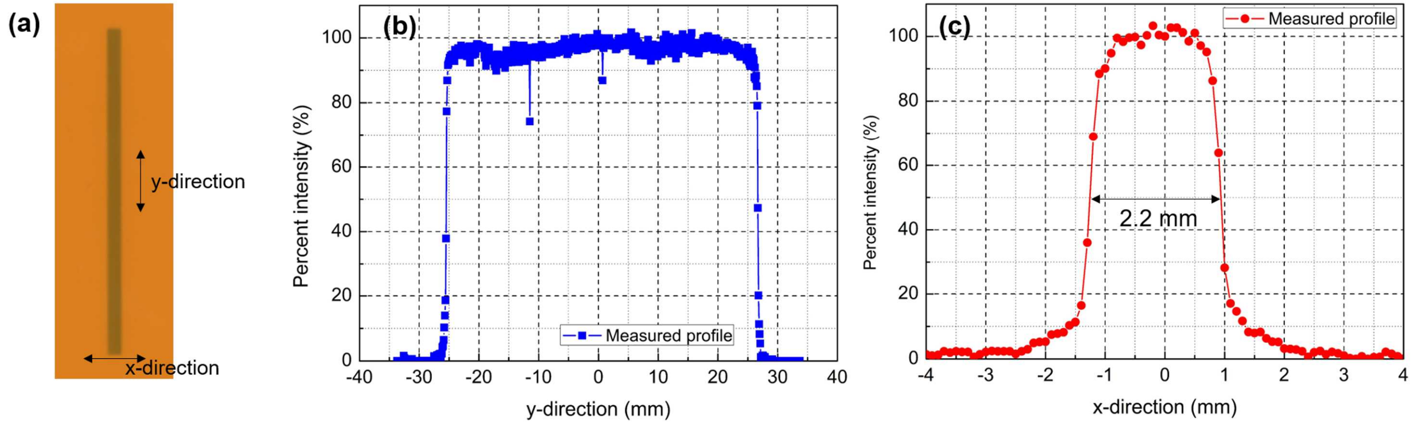

Fig. 26. (a) measured radiation field, (b) beam profile of y-direction and (c) x-direction. The XR-RV3 film was scanned by Epson 11000 XL and the profiles were analyzed by Verisoft 3.1 (PTW, Germany).

III.2.1.2 *Raw K-shell XRF Signal*

Fig. 27 illustrates the energy spectra of a central pixel of the CZT gamma camera which measured K-shell XRF photons and Compton scattered photons from GNP-loaded PMMA phantom with various concentrations for 1 minute. The XRF of $K_{\alpha 1}$ and $K_{\alpha 2}$ are shown to be a single peak due to their close energies and the low energy resolution of the CZT gamma camera. Higher concentration of GNPs emitted higher number of K-shell XRF photons. The highest peak was observed at 67.4–69.2 keV energy bin which corresponds to the energy of $K_{\alpha 1}$ (i.e., 69.04 keV).

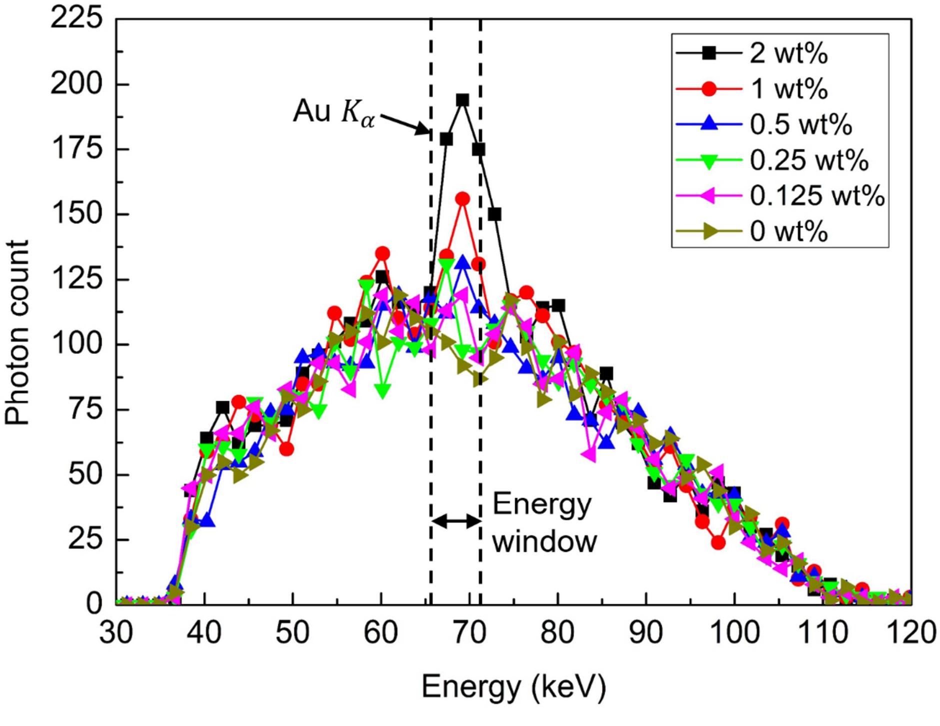

Fig. 27. Energy spectra of K-shell XRF and Compton scattered photons from 0 wt% to 2 wt% GNP columns at the central pixel of CZT gamma camera.

Fig. 28 shows the pixel coordinates of the CZT gamma camera. Particularly, the measured photon spectra of the pixels in the red boxes were shown in detail (Fig. 29). Although Cd-109 source emitted monochromatic 88 keV gammas only, the photo-peaks were observed at various channels ranged from 52 to 61 (Fig. 29). Therefore, the pixel-by-pixel difference in channel-to-energy conversion should be taken into account.

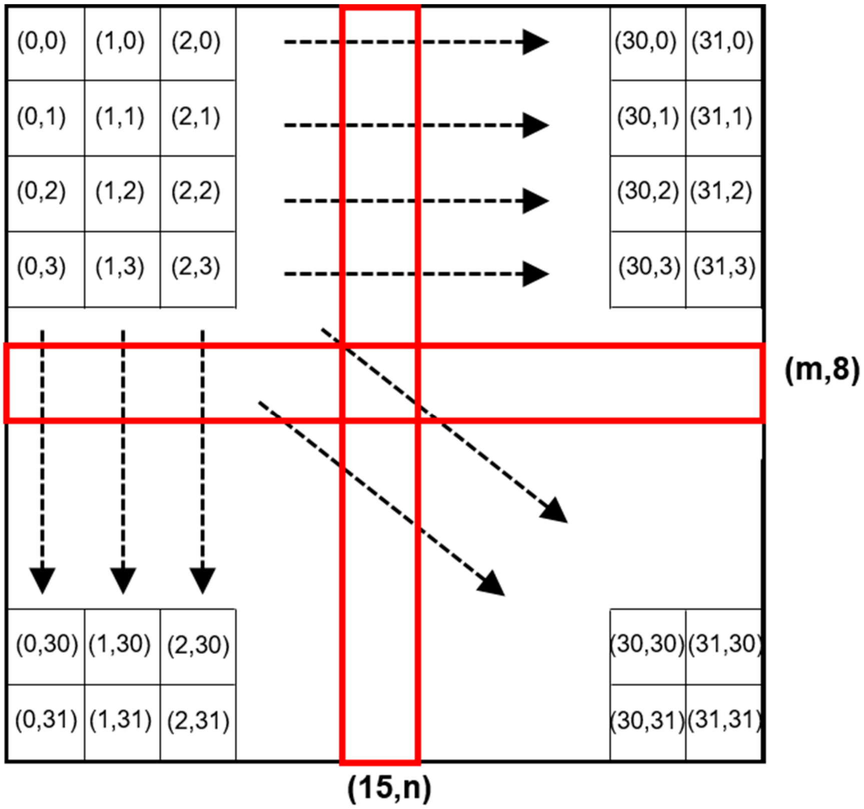

Fig. 28. Schematic description of pixel coordinates of CZT gamma camera. The measured spectra of pixels irradiated by Cd-109 source in two red boxes (i.e., (m, 8) and (15, n)) were shown in Fig. 29.

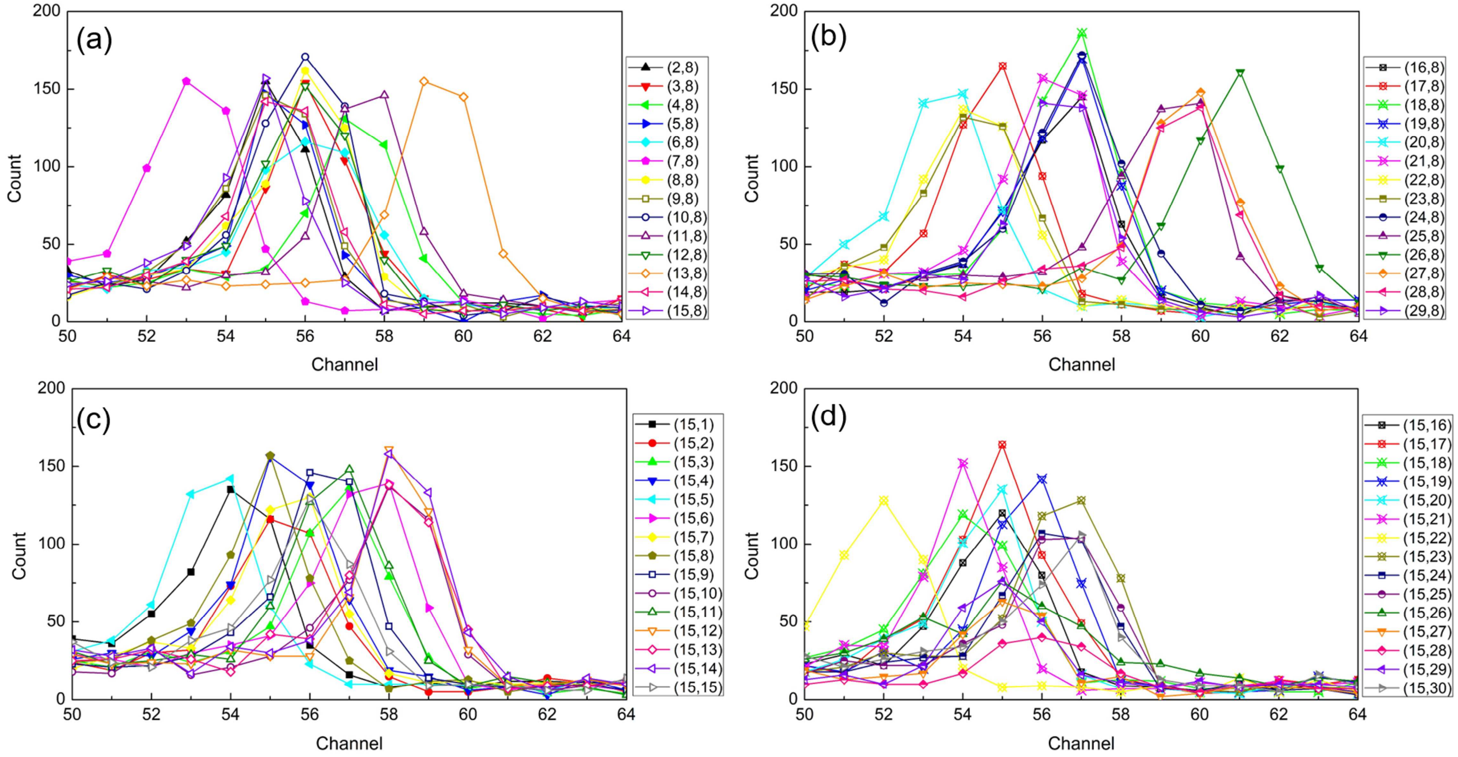

Fig. 29. The measured spectra of pixels irradiated by Cd-109 source in two red boxes (i.e., (m, 8) and (15, n)) were shown. Although Cd-109 emitted 88 keV gammas, the peak channels ranged from 52 to 61.

The subtraction of photon counts among the measured data from three different days is illustrated in Fig. 30. Black arrows indicate the abnormal pixels whose τ_i is greater than 3.408 (i.e., Chauvenet’s criterion). Fig. 30(d-f) shows the distribution of differences in photon counts. Although the average differences were different, the distributions were observed to follow a normal distribution. Four abnormal pixels had large differences in the counts than the others.

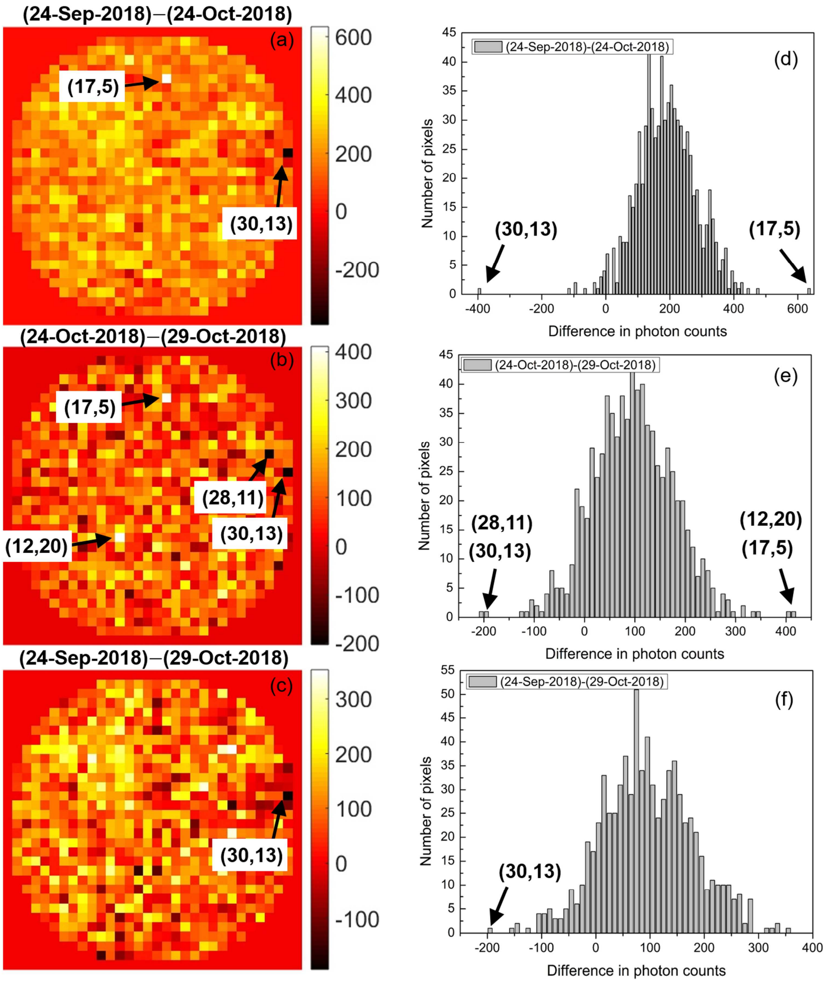

Fig. 30. (a) Subtraction of photon counts between measured data at (24-Sep-2018) and at (24-Oct-2018). (b) Subtraction of photon counts between measured data at (24-Oct-2018) and at (29-Oct-2018). (c) Subtraction of photon counts between measured data at (24-Sep-2018) and at (29-Oct-2018). (d-f) Four abnormal pixels were observed in histograms for (a), (b) and (c) with the bin size of 10 counts.

III.2.1.3 *Correction Factors*

Fig. 31 describes a map of detected photon counts per history from the MC simulation to calculate sensitivity correction factors. The central pixels had higher photon counts than the peripheral pixels. The map of sensitivity correction factors is shown in Fig. 31(b). The sensitivity correction factors greater than 1.25 were determined to be out of FOV.

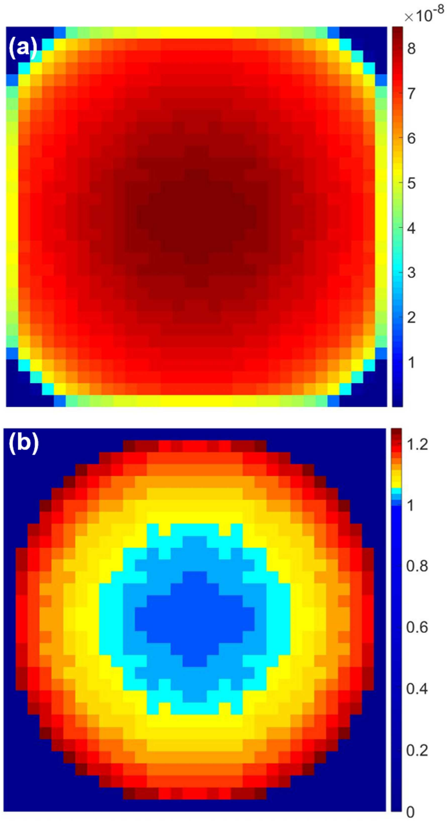

Fig. 31. (a) MC simulation result of detected XRF-like photons by CZT gamma camera and (b) sensitivity correction factors. Sensitivity correction factors greater than 1.25 were assumed to be zero.

A map of measured photon counts from Cd-109 radio-isotope is illustrated in Fig. 32. Four pixels had over than four times higher counts than the lowest counts. The pixels near the cross-line and in-line passing the center of CZT gamma camera showed lowest photon counts. When the maximum counts of the window level were adjusted to 6000, the regions of lower photon counts are shown more apparently (Fig. 32(b)). The pixel-by-pixel non-uniformity correction factors were highest for the pixels near the cross-line and the in-line. The uniformity factors ranged from 1 to 4.24 (Fig. 32(c)).

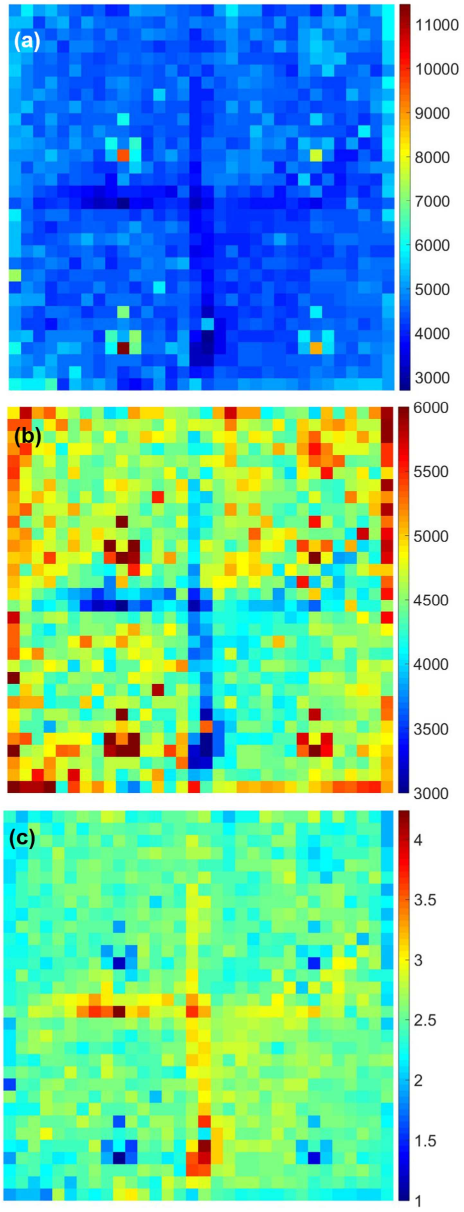

Fig. 32. (a) A map of measurement of 88.0 keV gammas from Cd-109 radio-isotope by CZT gamma camera and (b) the map of which window level of measured photon counts is from 3000 to 6000. (c) The pixel-by-pixel non-uniformity correction factors.

III.2.1.4 *K-shell XRF Image*

The effective pinhole diameters were 2.07 mm and 2.05 mm for $R_{eff,g}$ and $R_{eff,R}$. The geometric efficiency depends on the angle, θ. The geometric efficiency was 2.30×10^{-4} for the minimum angle (i.e., 0°) and 1.96×10^{-4} for the maximum angle (i.e., 18.4°). The collimator and intrinsic resolutions were 4.10 mm and 1.60 mm, respectively. The imaging system had the system resolution of 4.40 mm.

The K-shell XRF images multiplied by the 3×3 Gaussian filter of 0.125 wt% GNP column-loaded phantom with respect to total image acquisition time are shown in Fig. 33(a)-(e). Fig. 33(f) indicates the CNRs of XRF images with respect to total irradiation time. The mean CNR of 0.125 wt% GNPs was 8.7 ± 3.6 for total imaging time of 2 min (pre-scanning of 1min and post-scanning of 1 min). Since 1 min of irradiation for each scan had the CNRs fairly higher than Rose criterion (i.e., CNR = 4), the irradiation time for each scan was determined to be 1 min.

Fig. 34 illustrates the K-shell XRF images and the CNRs of 0.125 wt% to 2.0 wt% GNP-loaded PMMA phantom generated by the direct subtraction method (pre-scanning of 1 min and post-scanning of 1 min). The corrected K-shell XRF counts in the ROIs increased as the concentration of GNPs increased. Fig. 35 shows the linear relationship between the GNP concentrations and the mean count number per pixel in the ROIs for each GNP concentration. The error bars are standard deviations of those mean count number per pixel in the ROIs from ten measurements at 95% CI. The mean count number per pixel and the GNP concentrations showed a good linear relationship (R^2=0.9993).

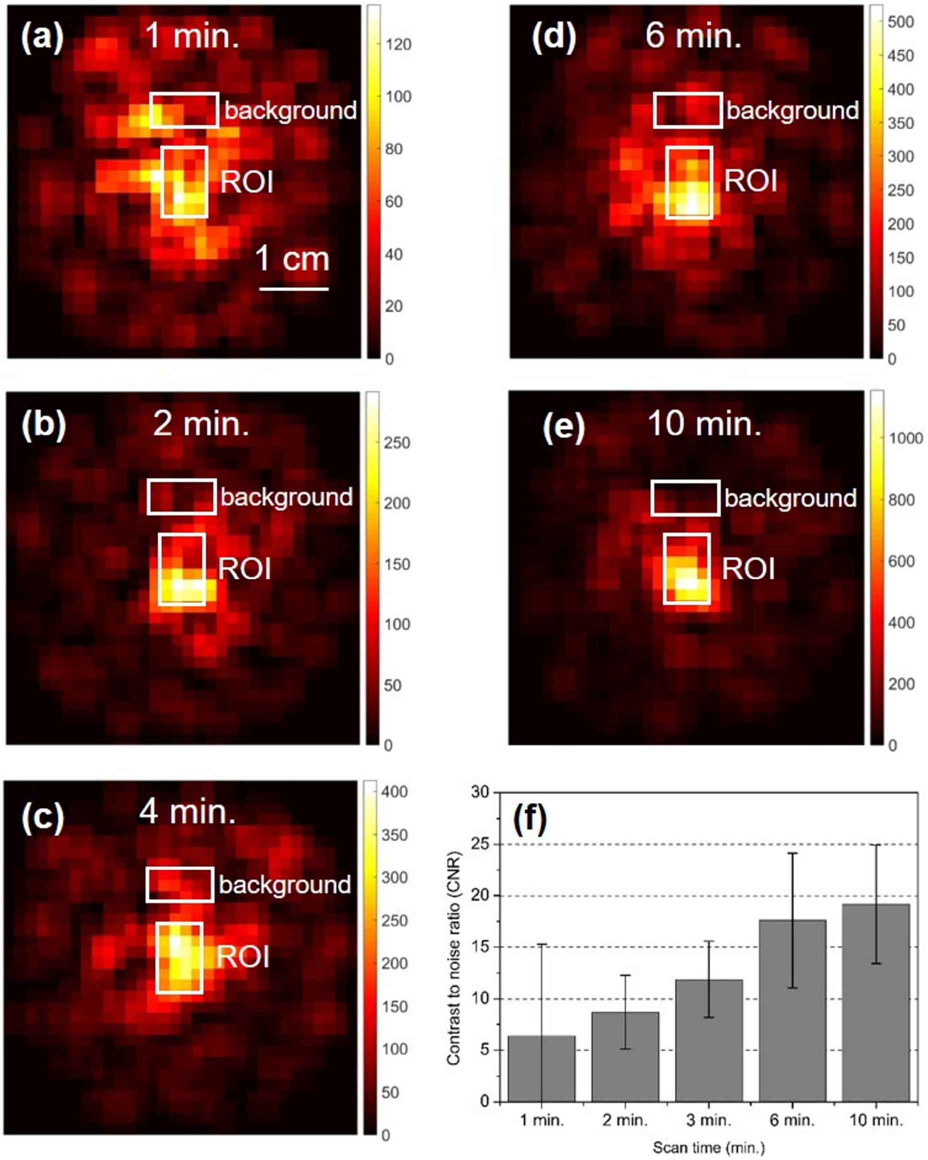

Fig. 33. XRF images of 0.125 wt% GNP column loaded-phantom with respect to total imaging time for (a) 1 min, (b) 2 min, (c) 4 min, (d) 6 min and (e) 10 min. (f) Contrast to noise ratio (CNR) of XRF images for 0.125 wt% GNP column loaded-phantom with respect to total imaging time. The measurements were conducted for five times in each imaging time.

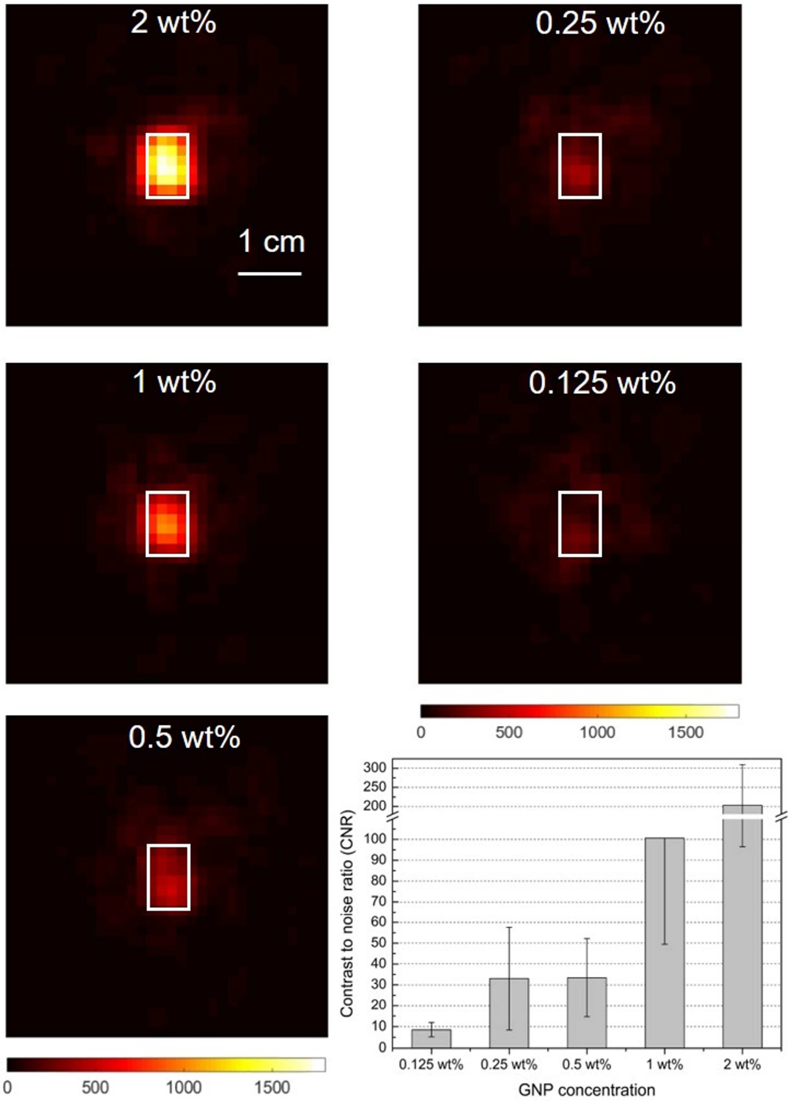

Fig. 34. XRF images and contrast to noise ratios (CNRs) of 0.125 wt%, 0.25 wt%, 0.5 wt%, 1.0 wt% and 2 wt% GNP columns. The total imaging time was 2 min for each GNP column.

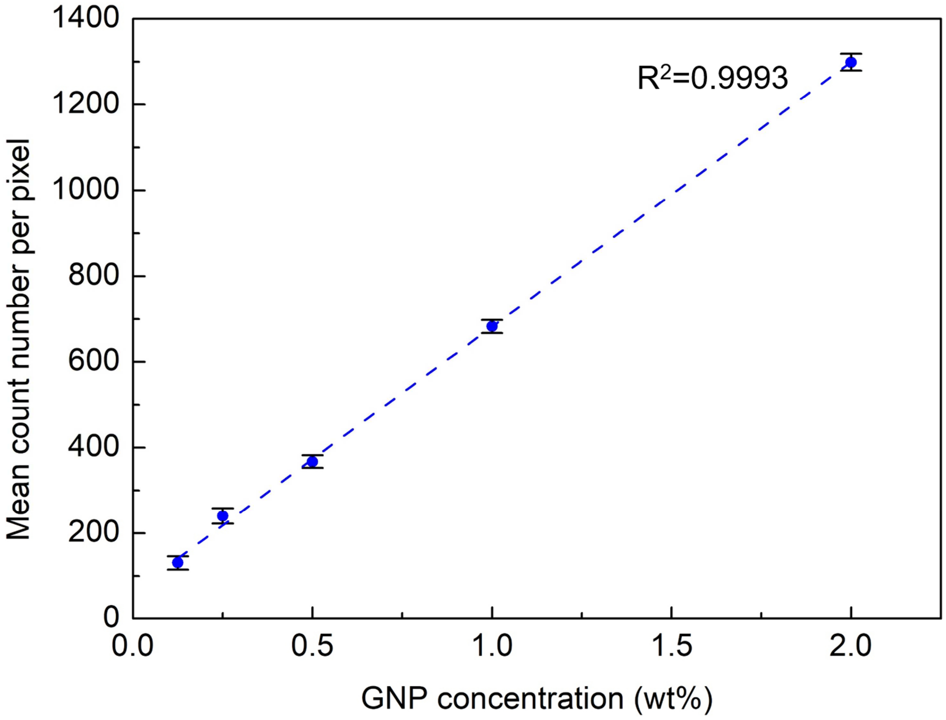

Fig. 35. A linear relationship between GNP concentrations and the mean count number per pixel in the ROIs measured by the CZT gamma camera. Dashed line indicates a linear regression curve.

III.2.2 K-shell XRF Detection System

Fig. 36(a) shows full energy spectra measured by the CdTe detector. The K-shell XRF detection system measured 0.0 wt%, 0.125 wt%, 0.25 wt%, 0.5 wt%, 1.0 wt%, 2.0 wt% GNPs. Three K-shell XRF peaks were observed at the energies of 67.2 keV ($K_{\alpha 2}$), 69.0 keV ($K_{\alpha 1}$), and 78.2 keV ($K_{\beta 1}$). Since, the most dominant two peaks were 67.2 keV and 69.0 keV, K-shell XRF counts were acquired from these peaks. Fig. 36(b) shows the energy spectra of 64 keV to 72 keV focusing on the range of interested energy window. One channel corresponded to about 0.15 keV. Since the Compton scattered photons from 0.0 wt% GNP-loaded phantom showed almost linear curve with some fluctuations between 62 keV to 72 keV (Fig. 36(b)), it was reasonable to make the artificial Compton background counts (triangles in Fig. 37) under K-shell XRF counts by using a linear interpolation. Fig. 38 shows the linear relationship between the corrected K-shell XRF counts measured by using the CdTe detector and the GNP concentrations. The error bars are standard deviations of those corrected K-shell XRF counts from ten measurements at 95% CI. The corrected K-shell XRF counts and the GNP concentration showed a good linear relationship (R^2=0.9933).

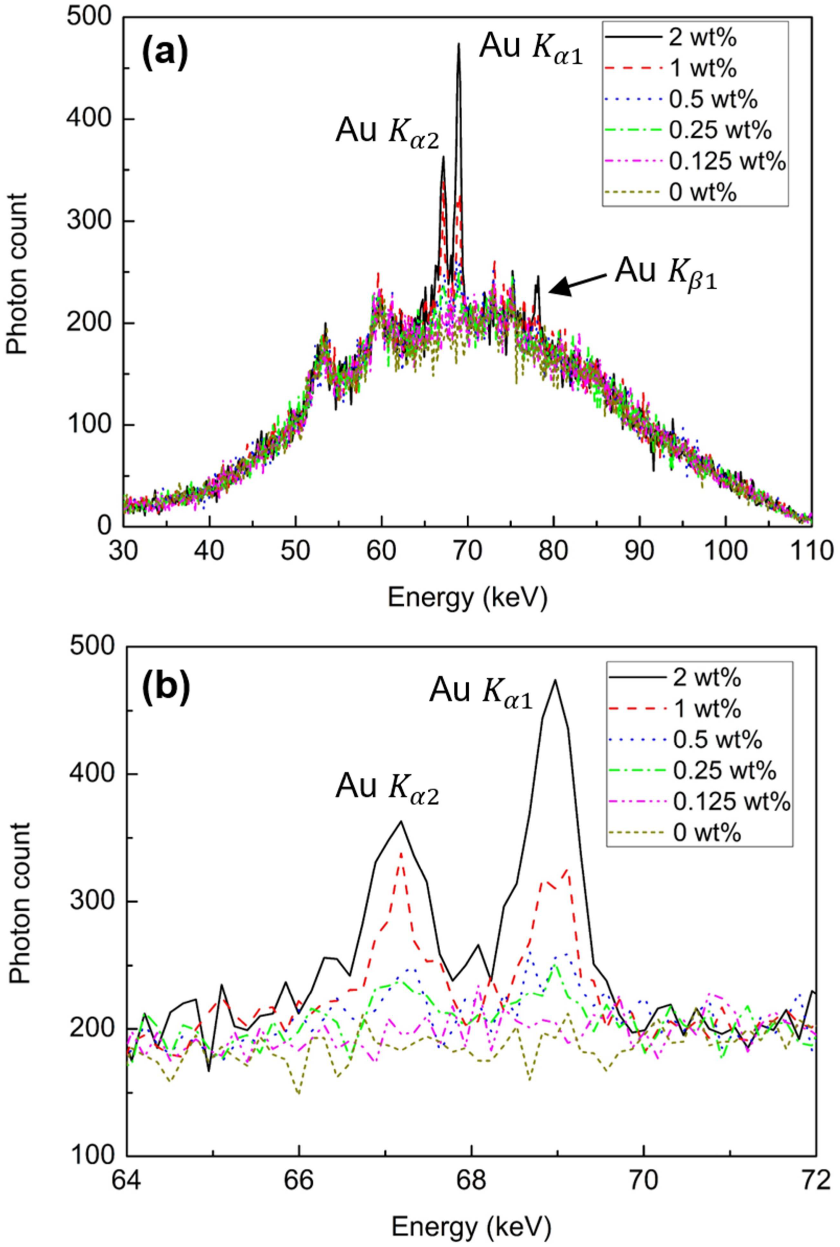

Fig. 36. Energy spectra of K-shell XRF photons and Compton scattered photon from GNPs of 0 wt%–2.0 wt%; (a) energy spectra of 30 to 120 keV, (b) energy spectra of 62 to 72 keV focusing on the range of K-shell XRF energy..

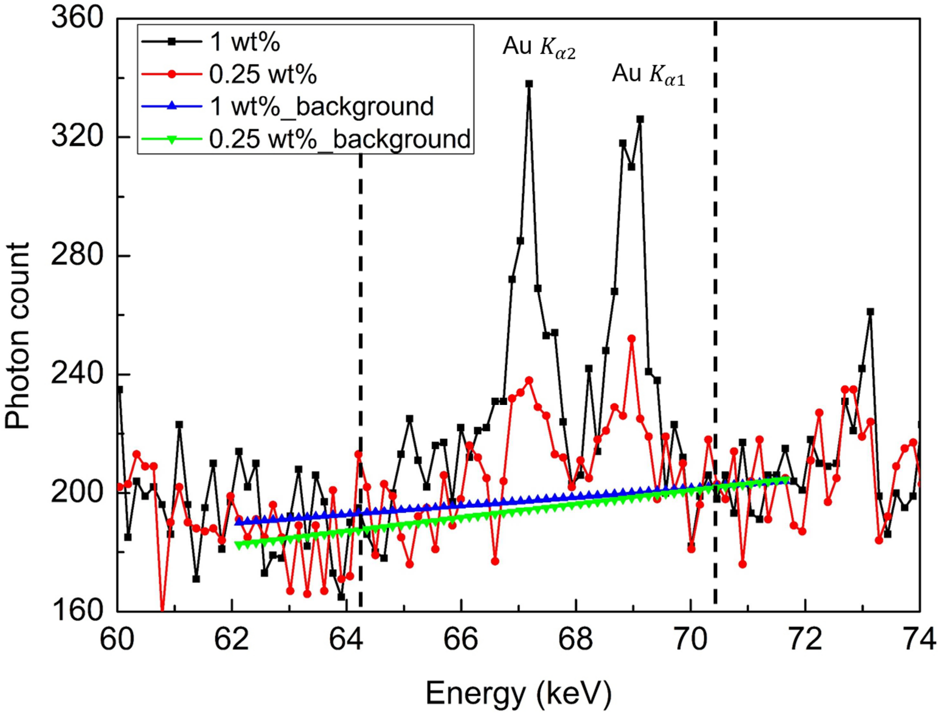

Fig. 37. K-shell XRF and Compton scattered photon spectra of 1 wt% (a line with squares) and 0.25 wt% (a line with circles). Linear interpolation curves of background count for 1 wt% and 0.25 wt% are plotted in a blue line with up-pointing triangles and a green line with down-pointing triangles, respectively.

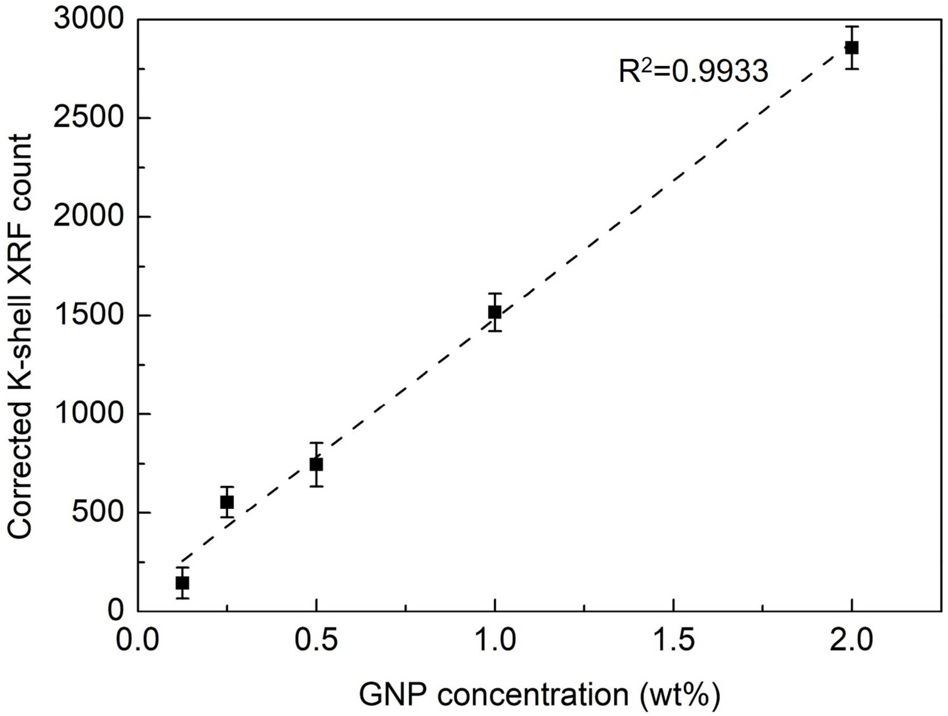

Fig. 38. Measurement data from GNP-loaded PMMA phantoms, showing a linear relationship between the corrected K-shell XRF counts and the GNP concentration from 0.125 wt% to 2 wt%.

III.2.3 L-shell XRF Detection System

Fig. 39(a) shows full energy spectra from the L-shell XRF measurement of GNPs of which the mass of GNPs was from 2.34 μg–300 μg when the GNP with DI water was 30 mg (0.0078 wt%–1.0 wt%). Three L-shell XRF peaks were observed at the energies of 9.71 keV ($L_{\alpha 1}$), 11.48 keV ($L_{\beta 1}$), and 13.42 keV ($L_{\gamma 1}$). Since, the most dominant two peaks were 9.71 keV and 11.48 keV, L-shell XRF counts were acquired from these peaks. Fig. 39(b) shows the energy spectra of 5.0 keV to 15.0 keV focusing on the range of interested energy window. One channel corresponded to about 0.0244 keV. Since L-shell XRF photons emitted from high concentrations of GNPs suffered self-absorption in the samples, the measured L-shell XRF photons along the concentrations of GNPs were assumed to follow an exponential function (i.e., R^2=0.9917) rather than a linear function. Fig. 40 shows the exponential relationship between the L-shell XRF counts measured by using the SDD and the mass of GNP. The L-shell XRF counts and the mass of GNP showed a good exponential relationship (R^2= 0.9917).

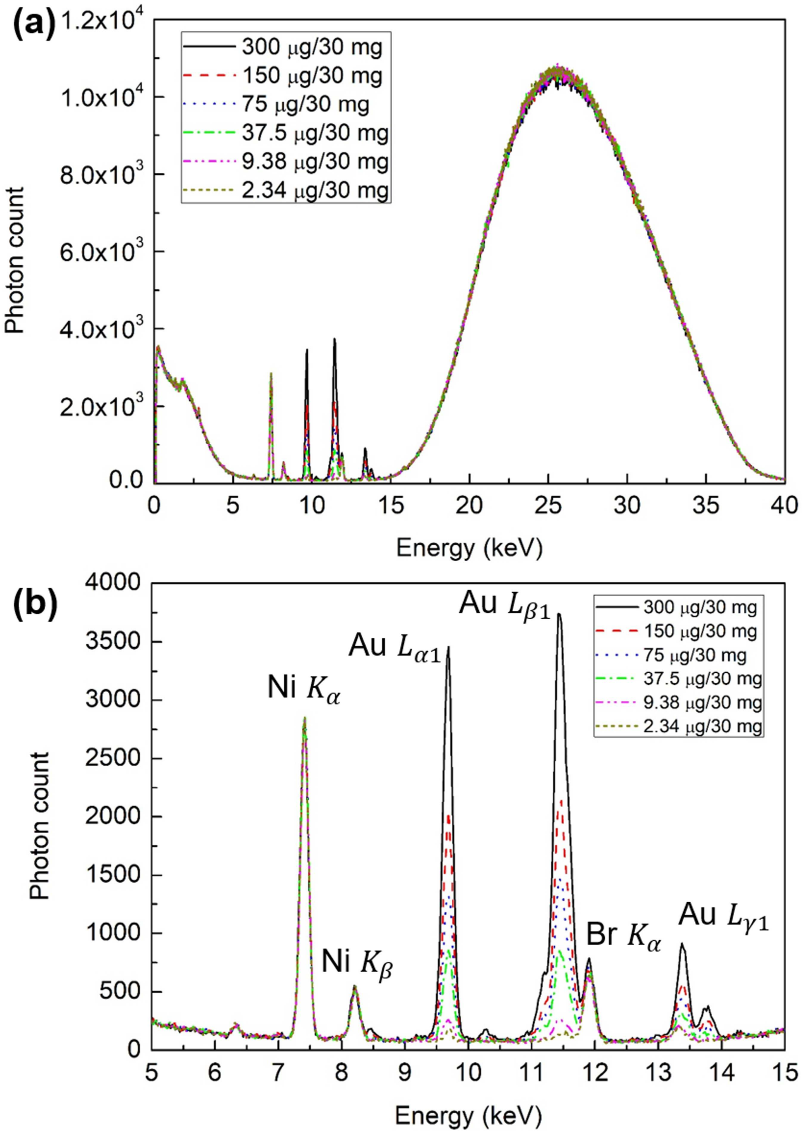

Fig. 39. Energy spectra of L-shell XRF photons from GNPs of 2.34 μg–300 μg mixed within 30 mg DI water (0.0078 wt%–1.0 wt% GNPs). (a) Energy spectra of 0 to 40 keV and (b) energy spectra of 5 to 15.0 keV focusing on the range of the L-shell XRF energy.

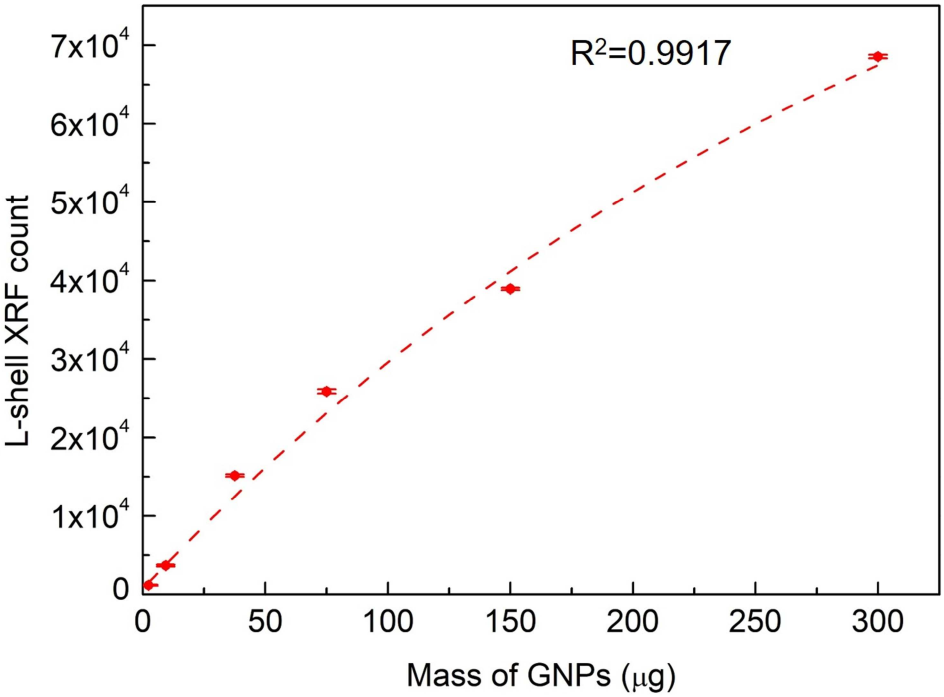

Fig. 40. An exponential relationship between mass of GNPs and L-shell XRF count measured by SDD. The dashed line indicates an exponential fitting curve.

III.3 *In vivo* Study in Mice

III.3.1 *In vivo* K-shell XRF Image

Fig. 41 shows the measured spectra of K-shell XRF and Compton scattered photons from the right kidney of mouse no.1 (M1) at pre-injection, and post-injection at T = 0, 30, 60 min. When compared with the measured spectrum at pre-injection, clear Au K_α XRF peaks within the energy window (vertical dashed lines in Fig. 41) were observed in those spectra measured post-injection. The raw K_α XRF counts were obtained by subtracting the photon counts at pre-injection from the photon counts at post-injections within the energy window. These raw K_α XRF counts were then treated for the attenuation, the sensitivity, the pixel-by-pixel non-uniformity corrections, and the 3×3 Gaussian filter.

Fig. 42 shows the K-shell XRF images of M1 at post injection T = 0, 10, 30 and 60 min and K-shell XRF images fused with the Compton scattered photon image. The image of the Compton scattered photons could at least provide a structure of the surface of the mice body. At T = 0 min, the maximum concentration of GNPs in the right kidney of M1 was observed. After T = 10 min, the GNPs in the right kidney of M1 were excreted and a pair of kidneys was shown in the K-shell XRF images. Fig 43 shows the XRF images of mouse no.2 (M2) and mouse no.3 (M3) at post injection T = 0 min and Compton/XRF fusion images. The right kidneys were observed in both XRF images. Although two more slices in the superior direction for each mouse were scanned, the left kidneys were not observed. The left kidney might be located in different slices in the inferior direction. The K-shell XRF images generated by the

2D CNN that did not require the pre-scanning of the mice were shown in Fig. 42 and Fig. 43 for the three mice.

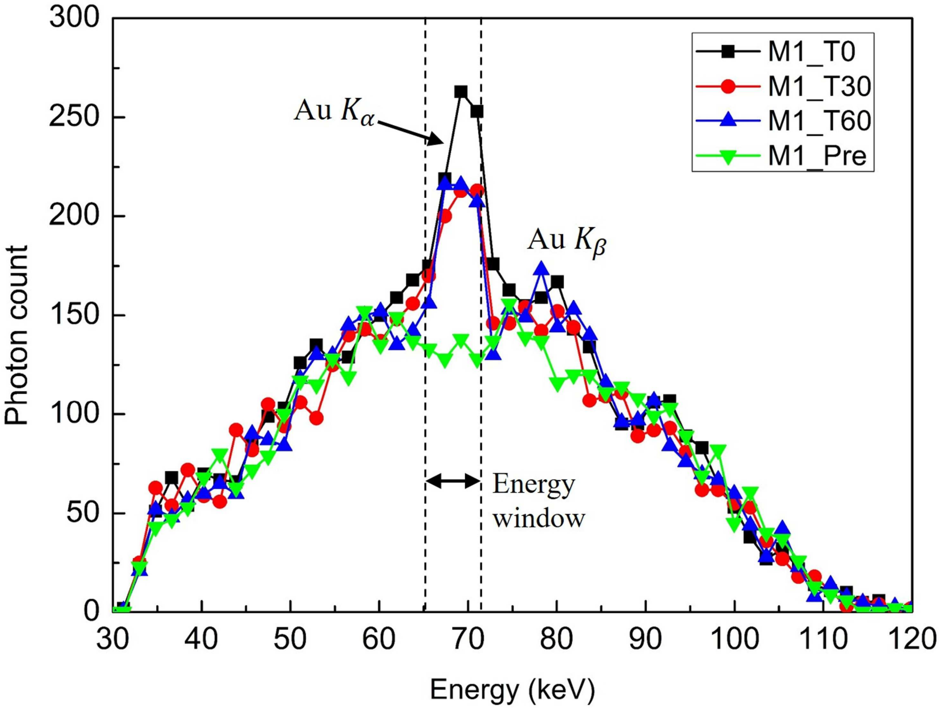

Fig. 41. Measured spectra of K-shell XRF of GNPs and Compton scattered photons from a right kidney of mouse 1 (M1) at pre-injection (pre), post-injection T = 0 min (T0), post-injection T = 30 min (T30) and post-injection T = 60 min (T60).

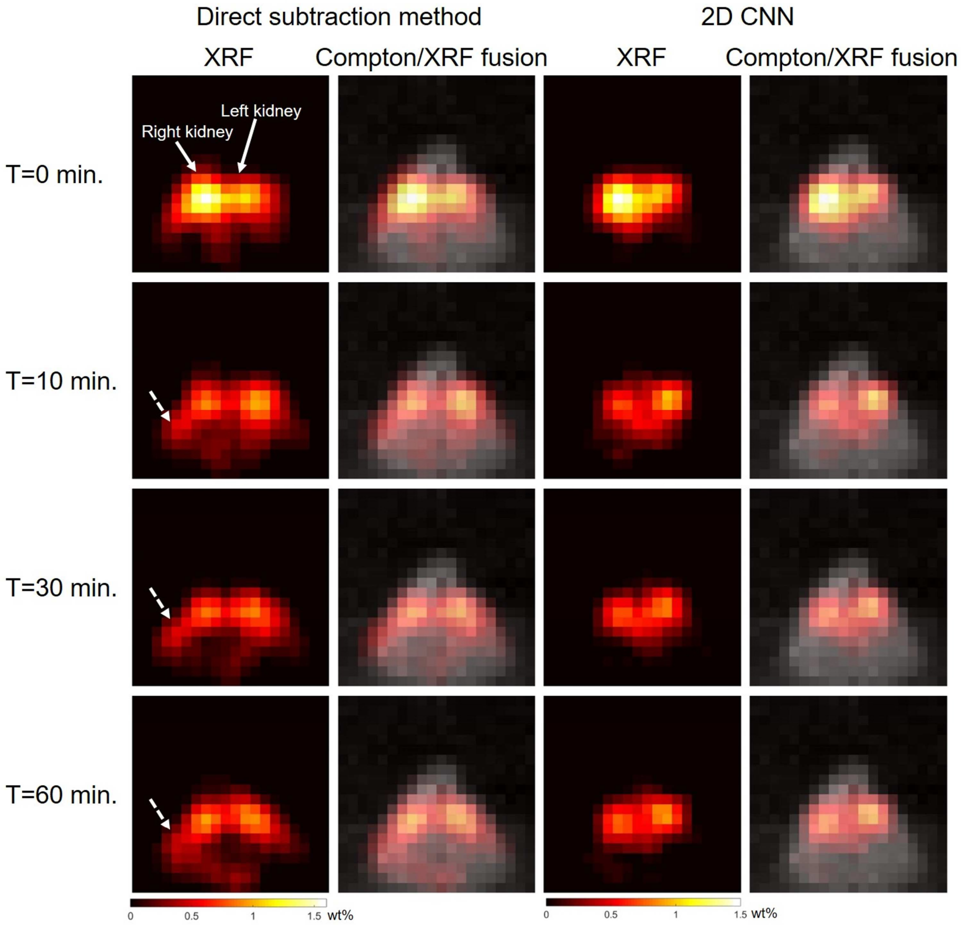

Fig. 42. Left two columns show XRF images of kidneys of mouse no. 1 (M1) at post-injection T = 0, 10, 30, 60 min processed by a direct subtraction method and the XRF images fused with Compton scattered images acquired at pre-injection. Right two columns show XRF images obtained by a 2D CNN and the XRF images fused with Compton scattered images. The white solid arrows indicate the location of kidneys. The white dashed arrows indicate the difference of XRF images between the direct subtraction method and the 2D CNN.

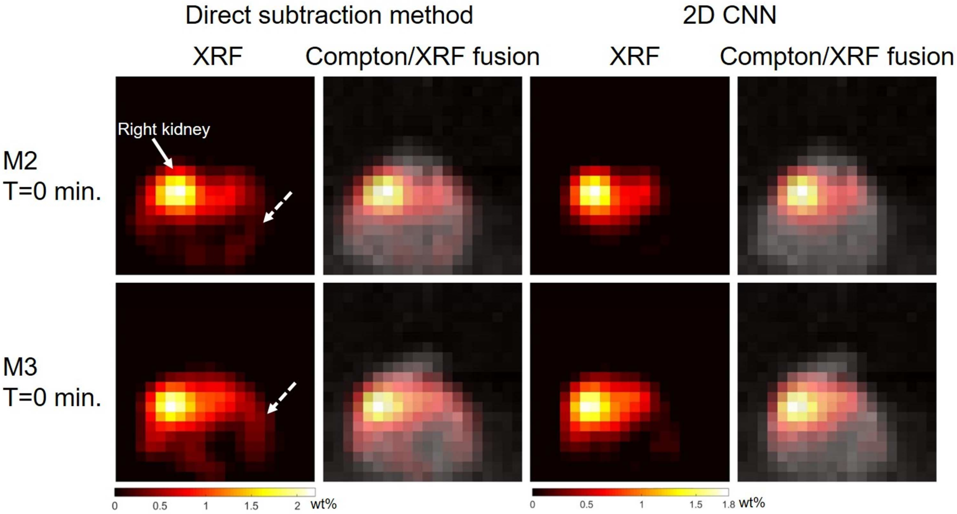

Fig. 43. Left two columns show XRF images of kidneys of mouse no. 2 (M2, top) and mouse no. 3 (M3, bottom) at post-injection T=0 min obtained by the direct subtraction method and the XRF images fused with Compton scattered images acquired at pre-injection. Right two columns show XRF images of kidneys of M2 (top) and M3 (bottom) at post-injection T = 0 min obtained by a 2D CNN and the XRF images fused with Compton scattered images acquired at pre-injection. The white solid arrow indicates the location of the kidneys. The white dashed arrows indicate the difference of XRF images between the direct subtraction method and the 2D CNN.

III.3.2 Quantification of GNPs in Living Mice

The CdTe detector and the parallel hole collimator were translated to target the right kidneys of the three mice at T = 10 min and photon spectra were measured by the CdTe detector (Fig. 44(a)). The attenuation corrections for the incident X-rays and the XRF photons were took into account. Since there was no information for the attenuation coefficient of the material along the beam path inside the mice, the attenuation coefficient of mice was assumed to be the same as the water. In addition, the nose cone factors were multiplied by the above attenuation corrections. The nose cone factors for M1, M2 and M3 were 1.67, 1.43, and 1.44, respectively. The clearance data of GNPs in the right kidneys from the three mice ($N = 3$) were obtained over a 60 min period (Fig. 45). The concentration of GNPs at T = 60 min was decreased by half from the concentration at T = 0 min. This tendency of GNPs in the kidneys to reduce in concentration with increasing T was comparable with the results from previous studies.[8] The measured concentrations by the K-shell detection system with the CdTe detector were 0.24 wt%-0.41 wt% lower than those measured by the CZT gamma camera.

Fig. 44(b) shows the measured spectra of the L-shell XRF of GNPs in the excised organs from the euthanized M3 and K-shell XRF photons from the head of the detector. In comparison with the measured spectra from the blood, liver and spleen, higher photon counts of Au L_α and L_β XRF peaks were observed in the spectra measured from a pair of kidneys. The masses of GNPs in tissue samples of the three mice were estimated by the calibration curve shown in Fig. 40. The concentrations of GNPs were then calculated by dividing the measured masses of the tissue samples. Fig. 46 illustrates the GNP concentrations in the organs harvested from the euthanized mice ($N = 3$). The Pearson correlation coefficient, r, for the fifteen excised organs was 0.9178. The concentrations measured by the L-shell detection system were compared with *in vivo* measurements and validated with the concentrations measured by ICP-AES. The difference in GNP concentrations in both kidneys measured by the L-shell XRF detection system and ICP-AES was 0.05-0.08 wt%.

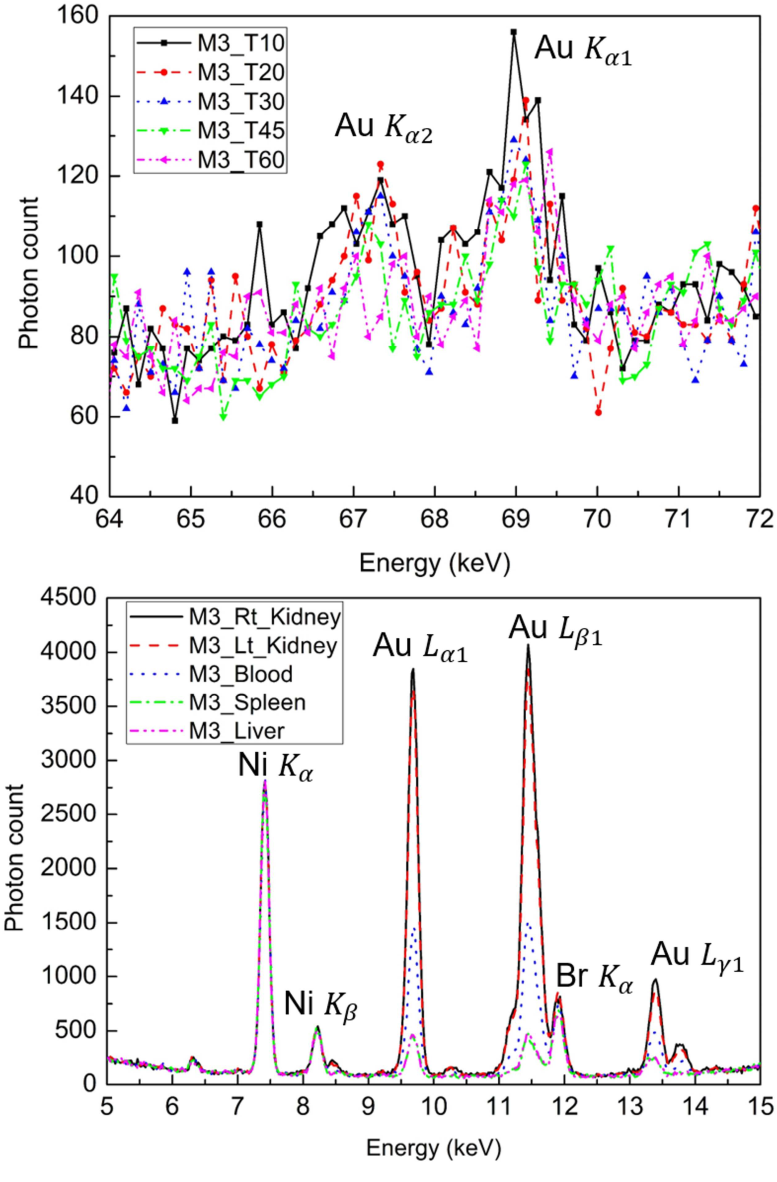

Fig. 44. Energy spectra measured from mouse no. 3 (M3) of (a) K-shell *in vivo* detection system and (b) L-shell *ex vivo* XRF detection system.

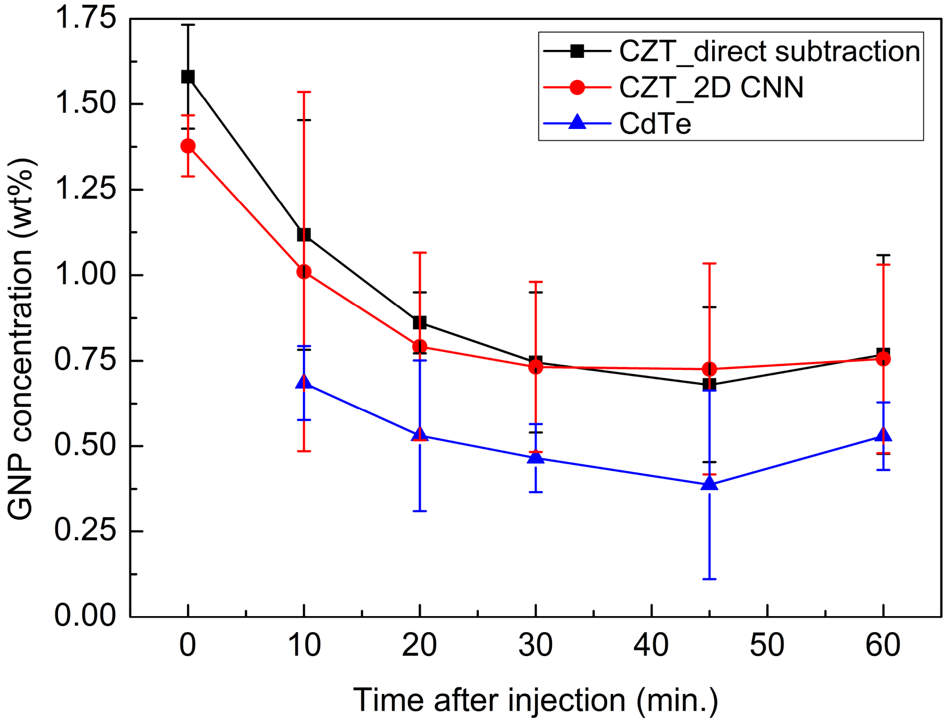

Fig. 45. Clearance of GNPs showing biodistribution in the mice right kidneys (*N* = 3) over a 60 min period after 40 mg of GNP injection measured by the CZT gamma camera with the direct subtraction method, by the CZT gamma camera with the 2D CNN, and by the K-shell XRF detection system with the CdTe detector.

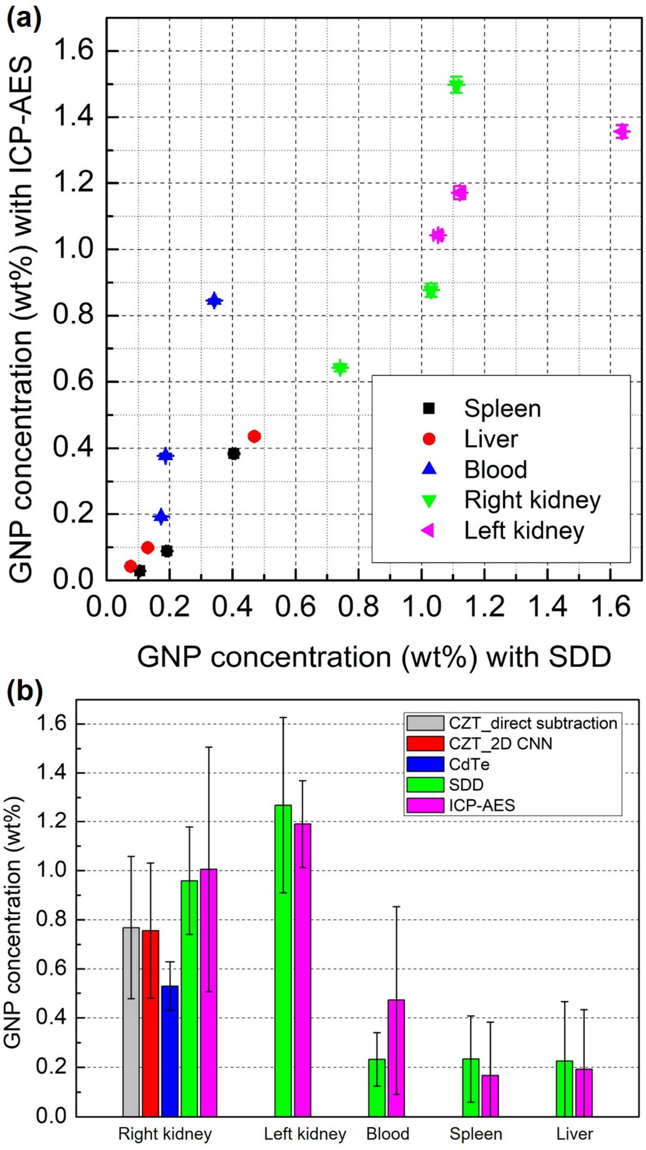

Fig. 46. GNP concentration in organs harvested from mice 60 min after injection. Concentration is measured by both the L-shell XRF detection with the SDD and ICP-AES. (a) All the data measured with both L-shell XRF detection with SDD and ICP-AES (n = 15). (b) Mean and standard deviations of GNP concentrations measured by CZT, CdTe, SDD and ICP-AES for three mice (N = 3).

III.3.3 Dose Measurement

The radiation doses to the skin of the three mice measured by TLDs are listed in Table 5. The delivered dose was 107 mGy during the acquisition of one slice image acquired by using the direct subtraction method (i.e., the sum of pre-scanning 1 min and post-scanning 1 min), while the dose for one slice image was reduced to 53 mGy by using the 2D CNN. Using the developed system, the total dose during the full *in vivo* imaging period was expected to be about 1120 mGy.

Table 5. Skin dose measured by TLDs for *in vivo* study in mice.

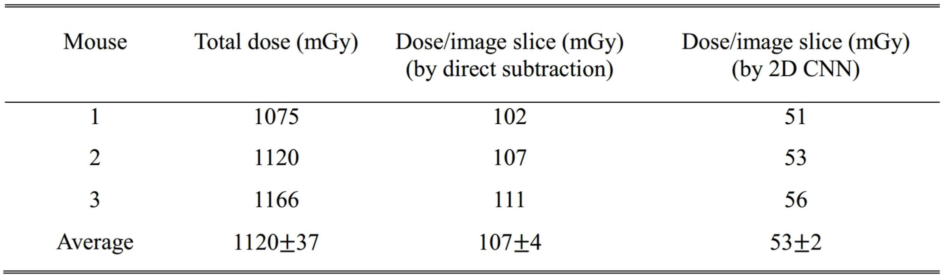

Mouse	Total dose (mGy)	Dose/image slice (mGy) (by direct subtraction)	Dose/image slice (mGy) (by 2D CNN)
1	1075	102	51
2	1120	107	53
3	1166	111	56
Average	1120±37	107±4	53±2

CHAPTER IV. DISCUSSION

IV.1 Monte Carlo Model

The suggested MC model of the pinhole K-shell XRF imaging using polychromatic X-rays and 2D array of position-sensitive detectors appears to be feasible for *in vivo* imaging and quantification of GdNP- or GNP columns within a small-animal-sized phantom. The filtered 110 kVp and 140 kVp could detect GdNP and GNP columns, respectively, as low as 0.01 wt% when the detector could resolve photon counts by 1 keV. The developed model could acquire 2D XRF images directly from only one fan-beam irradiation without any further process of beam scanning or rotation of phantoms.

Although 51 and 81 keV X-rays are close to K_{edge} energies of Gd and Au, respectively, the resulting images obtained by 60 and 95 keV beams showed superior image quality. The lower image quality of lower energy X-rays was caused by the statistical noise from subtraction of Compton scatter background, which was sometimes larger than the signals of XRF.[58] Although their integrated XRF counts were less than the monochromic X-rays, the proposed polychromatic X-rays could generate recognizable K-shell XRF images even for 0.01 wt% GdNPs and GNPs. For Au imaging, the filtered 140 kVp, which had a mean energy of 97.5 keV, showed always better image quality in terms of CNR values than 81 keV X-rays.

In the MC simulation, the images were degraded by the measured %FWHM at 59.5 keV. After the degradation, the mean pixel values in ROIs and standard deviations in the defined background region were reduced, while the mean pixel values in background region stayed similar as before. For Au imaging, CNR values of degraded images were always lower than those of 1 keV-resolution detector due to much decreased mean pixel values in ROIs, so that the Au column of 0.01 wt% could not be distinguished from the background. However, even though the blurs of Gd images were increased, CNRs of degraded images were similar or higher than those of 1 keV resolution detector. This was caused by much decreased standard deviations in the background region. The dose level (~ 30 mGy) predicted by MC simulations of the imaging system was much less than imaging doses (a few hundred mGy) delivered by XFCT and micro-CT scanning of small animals.[27,71]

IV.2 Development of Pinhole K-shell XRF Imaging System

The developed pinhole K-shell *in vivo* XRF imaging system using polychromatic X-rays and the CZT gamma camera was shown to be a potential *in vivo* imaging modality for GNP injected into living mice. The imaging system could detect GNP columns as low as 0.125 wt% in the imaging phantom. The imaging system acquired 2D XRF images directly from pre- and post-scanning of fan-beam irradiations without any further process of translation and rotation of objects. Hence, a short image acquisition time (i.e., 2 min per slice) could be achieved by using the direct subtraction method while the image acquisition time was 1 min per slice by using the 2D CNN.

Comparing with the parallel hole collimator XFCT system, the pinhole XRF imaging suffers from low detection efficiency. However, the pinhole system does not need to translate and rotate the sample to acquire a 2D slice image as the parallel-hole system does. This system can offer magnified images by simply adjusting the object-to-pinhole and pinhole-to-detector distances. La Riviere *et al.* also demonstrated that the pinhole imaging system could detect more XRF photons per unit time and the extended volume of phantom irradiated by incident X-rays improved imaging speed.[36,37] Therefore, these advantages could offset the low detection efficiency of pinhole system. Furthermore, implementation of multi-pinhole collimation system may improve the imaging speed and efficiency.[23,72]

IV.2.1 Quantification of GNPs

The clearance data of kidneys were acquired from the K-shell XRF images and the K-shell XRF measurements. By measuring the L-shell XRF photons from the excised organs, the L-shell XRF detection system could estimate much lower concentrations of GNPs than did *in vivo* XRF imaging system and was validated by ICP-AES. The L-shell XRF detection system is a non-destructive means of quantification for GNPs in biological samples compared to ICP-AES. In particular, the GNP concentration of the right kidneys measured by *in vivo* K-shell XRF images at T = 60 min after the injection was about 0.19-0.23 wt% lower than those concentrations analyzed by *ex vivo* measurements. This might be due to the heterogeneous distribution of Au in kidney. In order to avoid such discrepancies, it would be better to compare the concentrations of kidney homogenate samples. The concentrations of GNP in kidneys with normal function decayed exponentially as presented by Xu *et al.*[73] In fact, the concentrations in kidneys over 15 min after the injection could exhibit fluctuations and may display mouse-to-mouse variations.[73] In order to investigate the transport of the GNP in kidneys more carefully, a higher number of mouse to be imaged might be required. The relationship between the L-shell XRF counts and the GNP concentrations should be linear when the self-absorption of L-shell XRF counts in the sample is corrected. As reported by Ricketts *et al.*[45,46] and Manohar *et al.*,[41] the self-absorption in the sample could be corrected by dividing the measured L-shell XRF counts by the Compton scattered photon counts. In order to implement the scatter-correction technique, a parallel hole collimator is required to be additionally configured into the L-shell XRF detection system in future work. On the other hand, the differences between the measured concentrations by the CZT gamma camera and the K-shell detection system with the CdTe detector might be due to an imperfect attenuation correction treated for the K-shell XRF photons measured by the CdTe detector. In this study, the attenuation corrections for bony structures (in the superior direction of mice) and the self-absorption by GNPs were not considered.

IV.2.2 Comparison between MC and Experimental Results

Comparing the acquired the detection limit with the results from the MC model, the developed imaging system had about an order of ten times higher detection limit. This discrepancy might be due to the significant difference in the object-to-detector distances between the MC model and the developed imaging system. The MC model assumed that the distance was 5 cm, while the developed system had the distance of 15 cm. There existed a mechanical limitation of the experimental setup due to the size of stages where the phantom, the pinhole collimator and the CZT gamma camera were put on. In the MC model, the images were degraded by the measured %FWHM of 59.5 keV photons. In fact, the radiation transport codes could not solely include the physical degradations of the detector response such as electron hole trapping, non-uniformity and charge sharing.[74-76] Therefore, the %FWHM of CZT detector was measured to overcome the limitation of the MC study. However, since the measured %FWHM applied to the simulated spectra was pixel-averaged, there is a possible overestimation in the quality of the processed images. In addition, any systematic errors could not be explicitly considered in the MC study. In order to reduce the inter-scanning systematic errors (e.g., positioning, environmental condition for CZT detector), the experimental setup should be coincident for both pre- and post-scanning. Furthermore, the MC model could not reflect the limited count rate of the CZT gamma camera (i.e., 5.2×10^4 counts/sec for 1024 pixels).

IV.2.3 Limitations

IV.2.3.1 *Concentration*

The concentrations of GNPs accumulated in the organs or tumors in mice depend on the injected dose of GNPs, characteristics of GNPs (e.g., size, shape, and surface-coating). This is particularly true, in the previous studies conducted by Hainfeld *et al.*[8] and Manohar *et al.*,[27] that used the same 1.9 nm diameter GNPs without surface-coating (i.e., passive targeting) as used in the current study, where 40-54 mg of GNPs had been injected into the mice. The concentrations of GNPs in tumors were measured to be higher than 0.2 wt%. Although, such an injected dose is still acceptable in terms of LD_{50} (i.e., 2.7 g Au/kg), the injected dose in the aforementioned studies was much higher than the dose for typical *in vivo* studies using GNPs.[8,24,27] In order to use this XRF imaging technique as a preclinical molecular imaging modality, the XRF imaging system should be improved to detect the GNP concentrations as low as an order of 0.001 wt% (i.e., a few ppm level).[41-44] The detectable concentration is dependent on the performance (i.e., the energy resolution and maximum count rate) of a detector. In the early MC studies, it was assumed that the pixelated detectors have the same performance in terms of the energy resolution and maximum count rate as do the single-pixel detectors (e.g., X-123 CdTe or HPGe detector).[77,78] However, by overlooking an electronic noise, a charge sharing effect and a hole-tailing effect, those MC studies might have overestimated the image quality and detection limit. Therefore, some research groups have tried to develop pixelated detectors having a superior energy resolution and maximum count rate to enhance the detection limit of XFCT.[79] There have been other technical efforts to improve the energy resolution of pixelated semiconductor detectors.[75] Such detectors have been manufactured by several research groups for the purpose of detecting gamma rays in the space,[80] while those detectors have not been used for medical imaging purpose yet. On the other hand, the characteristics (i.e., spectrum and intensity) of incident X-rays can also affect the detection limit significantly. Quasi-monochromatic X-ray spectra with sufficient intensity can be obtained by adopting a carbon nantobue X-ray source or an X-ray source using highly oriented pyrolytic graphite.[55] The implementation of such X-ray sources can improve the detection limit by increasing the XRF photon counts and decreasing the Compton scattered photons.

IV.2.3.2 *System Resolution*

The current imaging system using the commercial CZT gamma camera has limitations in terms of the system resolution (e.g., the pixel size and the pinhole diameter) and the energy resolution. For the imaging of small animals, the system resolution of 4.40 mm was quite large for the size of the small organs. Hence, a magnification of the image by adjusting the distances between the beam plane-to-pinhole and pinhole-to-CZT gamma camera could be considered in future studies. For example, within a space available in the current system (i.e., 15 cm), the magnification factor can be increased by 2 when the distances of the beam plane-to-pinhole and of the pinhole-to-CZT gamma camera are 5 cm and 10 cm, respectively. According the theoretical equations (3)–(5) to calculate the system resolution, the increased magnification factor might improve the system resolution, i.e., from 4.4 mm to 3.4 mm. Furthermore, the use of a detector with smaller pixels and the use of a smaller pinhole can be pursued to enhance the system resolution. With a pinhole of 1 mm diameter, a 2.6 mm system resolution can be achievable. However, such an implementation will require increasing imaging time as well as an increased imaging dose.

IV.2.3.3 *Radiation Dose*

The skin dose (53 mGy by using the 2D CNN, and 107 mGy by using the direct subtraction method) during the image acquisition for one slice of a 2D image was similar to the imaging dose delivered by micro-CT (few 100 mGy[81] and 260 mGy[71]). On the other hand, it was much lower than the imaging doses (610 mGy[40] and 743 mGy[27]) delivered by the XFCT systems used for the recent *in vivo* studies. However, the comparison was conducted between the systems at different system resolutions and slice thickness. Particularly, the system resolution of XFCT system developed by Cho's research group could be varied with different step sizes and projection angles for data acquisition.[27] The system resolution of their system might have been above 2.5 mm, considering the diameter of the parallel hole of their collimator (i.e., 2.5 mm diameter).[27] However, this dose level may induce deterministic effects that could confound the biological outcome of the experiment with small animals.[71] Therefore, the dose level should be reduced as much as possible in future work.

IV.2.4 Application of CNN

The 2D CNN was applied to generate the K-shell XRF images from the post-scanning irradiation without pre-scanning. The 2D CNN could estimate the biodistributions of Au in living mice exposed to GNPs. Particularly, the model showed an excellent performance for the K-shell XRF images of the kidneys in M2 and M3. This application reduced the scan time and the imaging dose by half from the direct subtraction method. Furthermore, restraining the mice during the full imaging time is not necessary so that dynamic *in vivo* XRF images can obtained without the time limitation of anesthesia. Hence, the imaging system could acquire the biodistributions of GNPs at one day, one month or even longer period after the injection of GNPs. The imaging phantom used for the measurements had only single GNP column inserted in the phantom. The limited configurations of the shape of input and target images for the training dataset might cause the discrepancies of the concentrations in the kidneys as well as around the kidneys for M1 (Fig. 42). Unlike the single GNP column-loaded imaging phantom, GNPs were accumulated in a pair of kidneys within a close distance which resulted in an underestimation of the concentrations in both kidneys. If *in vivo* XRF images could be fed into the training dataset, more similarities between two methods will be achieved. Otherwise, new complex imaging phantoms mimicking GNP distributions of mice (e.g., GNP columns more than two with close distances) could be used to produce more realistic *in vivo* circumstance in the mice. In order to obtain 3D information of biodistributions of GNPs by stacking 2D XRF images, faster image acquisition time rather than 1 min will be required. Further investigation is required with a reduced image acquisition time, as the 2D CNN model should be updated with a new training dataset using the reduced irradiation time.

IV.2.5 Future Work

Since a CT scan was not available in this study, anatomical information was not available. With the animal CT images, more accurate attenuation corrections for incident X-rays and XRF photons could be applied to estimate the biodistributions of GNP. Further, the XRF image fused with the CT images would be useful in preclinical practices. Other metal nanoparticles rather than GNP can be used as an agent for the XRF imaging system. Since the minimum detectable energy for CZT gamma camera utilized in the current system is ~35 keV, the K-shell XRF photons from the MNP whose Z is greater than 63 (i.e., ~41 keV for Eu) is measurable. Thus, the XRF imaging system can be used to obtain the XRF images of multi-element MNPs injected into small animals in future studies. Since the imaging system was modeled and built by benchmarking the conventional pinhole SPECT system which detects much higher energy photons than K-shell XRF photons, further investigation in processing the XRF signals and optimizing the system design such as collimator design, X-ray filter, and tube potential is needed as reducing the dose level and improving the image quality as much as possible.

CHAPTER V. CONCLUSIONS

A pinhole K-shell XRF imaging system based on the proposed MC model, a K-shell XRF detection system, and an L-shell *ex vivo* XRF detection system were successfully developed. The biodistribution of GNPs in mice measured by pinhole *in vivo* K-shell XRF imaging system, K-shell XRF detection system and *ex vivo* L-shell XRF detection system was cross-compared and validated by ICP-AES. Using a 2D CZT gamma camera, dynamic *in vivo* K-shell XRF images were acquired and the image acquisition time was dramatically reduced to 1 min per slice. If the system is combined with a CT scanner, it will provide the anatomical information as well as the molecular information. This was the first investigation of dynamic *in vivo* XRF imaging of Au in living mice exposed to GNPs. The system could provide potential *in vivo* molecular imaging modality for MNPs to emerge as a radiosensitizer and a drug-delivery agent.

REFERENCES

[1]Salata O. Applications of nanoparticles in biology and medicine. *Journal of nanobiotechnology.* 2004;2(1):3.

[2]De Jong WH, Borm PJ. Drug delivery and nanoparticles:applications and hazards. *Int J Nanomedicine*. 2008;3(2):133-149.

[3]Jain PK, Huang X, El-Sayed IH, El-Sayed MA. Noble metals on the nanoscale: optical and photothermal properties and some applications in imaging, sensing, biology, and medicine. *Accounts of chemical research*. 2008;41(12):1578-1586.

[4]Zhang L, Gu FX, Chan JM, Wang AZ, Langer RS, Farokhzad OC. Nanoparticles in medicine: Therapeutic applications and developments. *Clin Pharmacol Ther*. 2008;83(5):761-769.

[5]Nazir S, Hussain T, Ayub A, Rashid U, MacRobert AJ. Nanomaterials in combating cancer: therapeutic applications and developments. *Nanomedicine-Uk*. 2014;10(1):19-34.

[6]Schuemann J, Berbeco R, Chithrani DB, et al. Roadmap to Clinical Use of Gold Nanoparticles for Radiation Sensitization. *Int J Radiat Oncol* 2016; 94: 189-205.

[7]Subiel A, Ashmore R and Schettino G. Standards and Methodologies for Characterizing Radiobiological Impact of High-Z Nanoparticles. *Theranostics* 2016; 6: 1651-1671.

[8]Hainfeld JF, Slatkin DN, Focella TM, Smilowitz HM. Gold nanoparticles: a new X-ray contrast agent. *The British Journal of Radiology*. 2006;79:248-253.

[9]Paunesku T, Ke T, Dharmakumar R, et al. Gadolinium-conjugated TiO2-DNA oligonucleotide nanoconjugates show prolonged intracellular retention period and T1-weighted contrast enhancement in magnetic resonance images. *Nanomedicine-Uk*. 2008;4(3):201-207.

[10]Park JY, Baek MJ, Choi ES, et al. Paramagnetic ultrasmall gadolinium oxide nanoparticles as advanced T1 MRI contrast agent: account for large longitudinal relaxivity, optimal particle diameter, and in vivo T1 MR images. *ACS nano*. 2009;3(11):3663-3669.

[11]Kim TJ, Chae KS, Chang Y, Lee GH. Gadolinium Oxide Nanoparticles as Potential Multimodal Imaging and Therapeutic Agents. *Curr Top Med Chem.* 2013;13(4):422-433.

[12]Hainfeld JF, Slatkin DN, Smilowitz HM. The use of gold nanoparticles to enhance radiotherapy in mice. *Phys Med Biol.* 2004;49(18):N309-315.

[13] Cho SH, Jones BL, Krishnan S. The dosimetric feasibility of gold nanoparticle-aided radiation therapy (GNRT) via brachytherapy using low-energy gamma-/x-ray sources. *Phys Med Biol.* 2009;54(16):4889-4905.

[14] Rahman WN, Bishara N, Ackerly T, et al. Enhancement of radiation effects by gold nanoparticles for superficial radiation therapy. *Nanomedicine-Uk.* 2009;5(2):136-142.

[15] Kim JK, Seo SJ, Kim HT, et al. Enhanced proton treatment in mouse tumors through proton irradiated nanoradiator effects on metallic nanoparticles. *Phys Med Biol.* 2012;57(24):8309-8323.

[16] Ngwa W, Korideck H, Kassis AI, et al. In vitro radiosensitization by gold nanoparticles during continuous low-dose-rate gamma irradiation with I-125 brachytherapy seeds. *Nanomedicine-Uk.* 2013;9(1):25-27.

[17] Lin Y, McMahon SJ, Paganetti H, Schuemann J. Biological modeling of gold nanoparticle enhanced radiotherapy for proton therapy. *Phys Med Biol.* 2015;60(10):4149-4168.

[18] Paro AD, Hossain M, Webster TJ, Su M. Monte Carlo and analytic simulations in nanoparticle-enhanced radiation therapy. *Int J Nanomedicine.* 2016;11:4735-4741.

[19] Sung W, Jung S, Ye SJ. Evaluation of the microscopic dose enhancement for nanoparticle-enhanced Auger therapy. *Phys Med Biol.* 2016;61(21):7522-7535.

[20] Liu Y, Liu X, Jin X, et al. The dependence of radiation enhancement effect on the concentration of gold nanoparticles exposed to low- and high-LET radiations. *Physica medica*. 2015; 31: 210-218.

[21] Her S, Jaffray DA and Allen C. Gold nanoparticles for applications in cancer radiotherapy: Mechanisms and recent advancements. *Adv Drug Deliv Rev.* 2017; 109: 84-101.

[22] Takeda T, Wu Jin, Lwin TT, et al. X-ray fluorescent CT imaging of cerebral uptake of stable-iodine perfusion agent iodoamphetamin alalog IMP in mice. *J Synchrotron Rad.* 2008;16:57-62.

[23] Sasaya T, Sunaguchi N, Hyodo K, Zeniya T, Yuasa T. Multi-pinhole fluorescence x-ray comptued tomography for molecular imaging. *Scientific Reports.* 2017;7:5742.

[24] Chou LY, Chan WC. Fluorescence-tagged gold nanoparticles for rapidly characterizing the size dependent biodistribution in tumor model. *Adv Healthc Mater.* 2012;1(6):714-21.

[25]De La Zerda A, Zavaleta C, Keren S, et al. Carbon nanotubes as photoacoustic molecular imaging agents in living mice. *Nat Nanotechnol.* 2008;3:557-62.

[26]Li W, Chen X. Gold nanoparticles for photoacoustic imaging. *Nanomedicine (UK).* 2015;10(2):299-320.

[27]Manohar N, Reynoso FJ, Diagaradjane P, Krishnan S, Cho SH. Quantitative imaging of gold nanoparticle distribution in a tumor-bearing mouse using benchtop x-ray fluorescence computed tomography. *Scientific reports.* 2016;6:22079.

[28]Si-Mohamed S, Cormode DP, Bar-Ness D, et al. Evaluation of spectral photon counting computed tomography K-edge imaging for determination of gold nanoparticle biodistribution in vivo. *Nanoscale.* 2017;9:18246-18257.

[29]Cho SH, Krishnan S, Cancer nanotechnology: principles and applications in radiation oncology. Boca Raton, FL: CRC Press. 2013:99-108.

[30]Perkins, ST, Cullen DE, Chen MH., Hubbel JH., Rathkopf J, Scofield J. Tables and Graphs of Atomic Subshell and Relaxation Data Derived from the LLNL Evaluated Atomic Data Library (EADL), Z= 1-100, Lawrence Livermore National Laboratory, Report UCRL-50400 Series, Livermore (CA). 199.

[31]Vernekohl D, Ahmad M, Chinn G, Xing L. Feasibility study of Compton cameras for x-ray fluorescence computed tomography with humans. *Phys. Med. Biol.* 2016;61:8521-8540.

[32]Boisseau P. Determination of three dimensional trace element distributions by the use of monochromatic X-ray microbeams. Ph.D. dissertation. Cambridge: Massachusetts Institute of Technology; 1986.

[33]Cheong SK, Jones BL, Siddiqi AK, Liu F, Manohar N, Cho SH. X-ray fluorescence computed tomography (XFCT) imaging of gold nanoparticle-loaded objects using 110 kVp x-rays. *Phys Med Biol*. 2010;55(3):647-662.

[34]Jones BL, Manohar N, Reynoso F, Karellas A, Cho SH. Experimental demonstration of benchtop x-ray fluorescence computed tomography (XFCT) of gold nanoparticle-loaded objects using lead- and tin-filtered polychromatic cone-beams. *Phys Med Biol.* 2012;57(23):N457-467.

[35]Ahmad M, Bazalova-Carter M, Fahrig R, Xing L. Optimized Detector Angular Configuration Increases the Sensitivity of X-ray Fluorescence Computed Tomography (XFCT). *IEEE Trans Med Imaging.* 2015;34(5):1140-1147.

[36] Meng LJ, Li N, La Riviere PJ. X-ray Fluorescence Emission Tomography (XFET) with Novel Imaging Geometries - A Monte Carlo Study. *IEEE Trans Nucl Sci.* 2011;58(6):3359-3369.

[37] Fu G, Meng LJ, Eng P, Newville M, Vargas P, La Riviere P. Experimental demonstration of novel imaging geometries for x-ray fluorescence computed tomography. *Med Phys.* 2013;40(6):061903.

[38] Groll A, George J, Vargas P, La Riviere PJ, Meng LJ. Element Mapping in Organic Samples Utilizing a Benchtop X-Ray Fluorescence Emission Tomography (XFET) System. *IEEE Trans Nucl Sci.* 2015;62(5):2310-2317.

[39] Sasaya T, Sunaguchi N, Seo SJ, Hyodo K, Zeniya T, Kim JK, Yuasa T. Preliminary study on X-ray fluorescence computed tomography imaging of gold nanoparticles: Acceleration of data acquisition by multi pinholes scheme. *Nucl Instrum Meth A.* 2018;886:71-6.

[40] Zhang S, Li L, Chen J, Chen Z, Zhang W, Lu H. Quantitative imaging of Gd nanoparticles in mice using benchtop cone-beam X-ray fluorescence computed tomography system. *Int J Mol Sci*. 2019;20:2315.

[41] Manohar N, Reynoso FJ, Cho SH. Experimental demonstration of direct L-shell x-ray fluorescence imaging of gold nanoparticles using a benchtop x-ray source. *Med Phys.* 2013;40(8):080702.

[42] Bazalova-Carter M. The potential of L-shell X-ray fluorescence CT (XFCT) for molecular imaging. *The British journal of radiology.* 2015;88(1055):20140308.

[43] Bazalova-Carter M, Ahmad M, Xing L, Fahrig R. Experimental validation of L-shell x-ray fluorescence computed tomography imaging: phantom study. *Journal of medical imaging.* 2015;2(4):043501.

[44] Ahmed MF, Yasar S, Cho SH. Development of an attenuation correction method for direct x-ray fluorescence (XRF) imaging utilizing gold L-shell XRF photons. *Med Phys.* 2018;45(12):5543-54.

[45] Ricketts K, Castoldi A, Guazzoni C, Ozkan C, Christodoulou C, Gibson A P and Royle G J. A quantitative x-ray detection system for gold nanoparticle tumour biomarkers. *Phys Med Biol.* 2012.;57:5543-55.

[46] Ricketts K, Guazzoni C, Castoldi A and Royle G. A bench-top K X-ray fluorescence system for quantitative measurement of gold nanoparticles for biological sample diagnostics . *Nucl Instrum Meth A.* 2016;816:25-32.

[47]Jaszczak RJ., Li JY, Wang HL, Zalutsky MR, Coleman RE. Pinhole Collimation for Ultra-High-Resolution, Small-Field-of-View Spect. *Phys Med Biol.* 1994;39:425-437.

[48]Deloar HM, Watabe H, Aoi T, Iida H. Evaluation of penetration and scattering components in conventional pinhole SPECT: phantom studies using Monte Carlo simulation. *Phys Med Biol.* 2003;48:995-1008.

[49]Cherry SR, Sorenson JA, Phelps ME. Physics in nuclear medicine, 4th ed. Philadelphia, PA: Saunders, 2012.

[50]Moji V, Zeraatkar N, Farahani MH, Aghamiri MR, Sajedi S, Teimourian B, et al. Performance evaluation of a newly developed high-resolution, dual-head animal SPECT system based on the NEMA NU1-2007 standard. *Journal of Applied Clinical Medical Physics.* 2014;15:267-678.

[51]Peterson M, Strand SE, Ljungberg M. Using Rose's metal alloy as a pinhole collimator material in preclinical small-animal imaging: A Monte Carlo evaluation. *Med Phys.* 2015;42:1698-1709.

[52]Goorley T, James M, Booth T, et al. Initial Mcnp6 Release Overview. *Nucl Technol.* 2012;180(3):298-315.

[53]Alnafea M, Wells K, Spyrou NM, Guy M. Preliminary Monte Carlo study of coded aperture imaging with a CZT gamma camera system for scintimammography. *Nucl Instrum Meth A.* 2007;573(1-2):122-125.

[54]Campbell DL, Peterson TE. Simulation study comparing high-purity germanium and cadmium zinc telluride detectors for breast imaging. *Phys Med Biol.* 2014;59(22):7059-7079.

[55]Manohar N, Jones BL, Cho SH. Improving x-ray fluorescence signal for benchtop polychromatic cone-beam x-ray fluorescence computed tomography by incident x-ray spectrum optimization: a Monte Carlo study. *Med Phys.* 2014;41(10):101906.

[56]Iwanczyk JS, Iniewski K. Radiation detectors for medical imaging. Roca Ration, FL: CRC Press, 2016:193-232.

[57]IDEAS, Oslo, Norway, Gamma Camera-6400px-350keV [Online]. Available: http://www.ideas.no.

[58]Ahmad M, Bazalova M, Xiang L, Xing L. Order of magnitude sensitivity increase in X-ray Fluorescence Computed Tomography (XFCT) imaging with an optimized spectro-spatial detector configuration: theory and simulation. *IEEE Trans Med Imaging*. 2014;33:1119-28.

[59]Poludniowski G, Landry G, DeBlois F, Evans PM, Verhaegen F, SpekCalc: a program to calculate photon spectra from tungsten anode X-ray tubes. *Phys Med Biol.* 2009;54:N443-N438.

[60]Pidikiti R, Stojadinovic S, Speiser M, Song KH, Hager F, Saha D, et al., Dosimetric characterization of an image-guided stereotactic small animal irradiator. *Phys Med Biol.* 2011;56:2585-99.

[61]Mesbahi A, Zakariaee SS. Effect of anode angle on photon beam spectra and depth dose characteristics for X-RAD320 orthovoltage unit. *Rep Pract Oncol Radiother.* 2013;18:148-52.

[62]Noblet C, Chiavassa S, Smekens F, Sarrut D, Passal V, Suhard J, et al. Validation of fast Monte Carlo dose calculation in small animal radiotherapy with EBT3 radiochromic films. *Phys Med Biol.* 2016;61:3521-35.

[63]Hubbell JH, Seltzer SM. Tables of X-ray mass attenuation coefficients and mass energy-absorption coefficients 1 keV to 20 MeV for elements Z=1 to 92 and 48 additional substances of dosimetric interest. National Inst. Of Standards and Technology-PL, Gaithersburg, MD, Tech. Rep. TRN:51812148 1995.

[64]Connolly LP, Treves ST, Davis RT, Zimmerman RE. Pediatric applications of pinhole magnification imaging. *J Nucl Med.* 1999;40(11):1896-1901.

[65] AuroVist^{TM} Product Information and Instructions, Nanoprobes, Inc. 2009

[66]Chu SYF, Ekstrom LP, Firestone RB, The Lund/LBNL Nuclear Data Search version 2.0. 1999. [Online] Available: http://nucleardata.nuclear.lu.se/toi.

[67]Deepa P, Suganthi M. Performance evaluation of various denoising filters for medical image. *International Journal of Computer Science and Information Technologies*. 2014;5(3):4205-4209.

[68]Umapathi VJ, Narayanan VS. Medical image denoising based on Gaussian filter and DWT SWT based enhancement technique. *International Journal of Soft Computing and Artificial Intelligence.* 2014;2.

[69]Amptek, Bedford, USA, X-123SDD [Online]. Available: http://amptek.com/products/x-123sdd-complete-x-ray-spectrometer-with-silicon-drift-detector-sdd.

[70]Ma CM, Coffey CW, DeWerd LA, et al. AAPM protocol for 40-300 kV x-ray beam dosimetry in radiotherapy and radiobiology. *Med Phys.* 2001;28:868-93.

[71]Boone JM, Velazquez O, Cherry SR. Small-animal X-ray dose from micro-CT. *Molecular imaging.* 2004;3(3):149-158.

[72] Deng L, Wei B, He P, Zhang Y, Feng P. A Geant4-based Monte Carlo study of a benchtop multi-pinhole X-ray fluorescence computed tomography imaging. *Int J Nanomedicine*. 2018;13:7207-7216.

[73] Xu J, Yu M, Carter P, Hernandez E, Dang A, Kapur P, et al. In vivo x-ray imaging of transport of renal clearable gold nanoparticles in the kidneys. *Angewandte Chemie*. 2017;56:13356-13360.

[74] d'Aillon EG, Tabary J, Gliere A, Verger L. Charge sharing on monolithic CdZnTe gamma-ray detectors: A simulation study. *Nucl Instrum Meth A.* 2006;563(1):124-127.

[75] Del Sordo S, Abbene L, Caroli E, Mancini AM, Zappettini A, Ubertini P. Progress in the Development of CdTe and CdZnTe Semiconductor Radiation Detectors for Astrophysical and Medical Applications. *Sensors-Basel.* 2009;9(5):3491-3526.

[76] Bolotnikov AE, Camarda GS, Cui Y, et al. Characterization and evaluation of extended defects in CZT crystals for gamma-ray detectors. *J Cryst Growth.* 2013;379:46-56.

[77] Jones BL, Cho SH. The feasibility of polychromatic cone-beam x-ray fluorescence computed tomography (XFCT) imaging of gold nanoparticle-loaded objects: a Monte Carlo study. *Phys Med Biol.* 2011;56:3719-30.

[78] Dunning CAS, Bazalova-Carter M. Optimization of a table-top x-ray fluorescence computed tomography (XFCT) system. *Phys Med Biol*. 2018;63:235013.

[79] Li M, George J, Meng LJ. Broadband X-ray fluorescence emission tomography with a small pixel CdTe imaging-spectrometry detector. *J Nucl Med*. 2017;58:401.

[80] KoKubun M, Nakazawa K, Enoto T, Fukazawa Y, Gilmore K, Kataoka J, et al. Hard X-ray imager (HXI) for the ASTRO-H mission. *In Proc. SPIE.* 2010;7732:773215.

[81] Badea CT, Drangova M, Holdsworth DW, Johnson GA. In vivo small animal imaging using miro-CT and digital subtraction angiography. *Phys Med Biol.* 2008;53:R319-R350.

ABSTRACT (in Korean)

국 문 초 록

목적: 본 연구의 목표는 금나노입자의 체내 농도 분포 측정을 위한 핀홀 엑스선 형광 영상시스템을 개발하고, 시간에 따른 쥐의 체내 금나노입자 분포 영상을 획득하여 개발 영상시스템이 전임상시험에 활용 가능함을 실험적으로 증명하는 것이다. 2차원 cadmium zinc telluride (CZT) 감마카메라를 사용하여 K-shell 엑스선 형광 신호를 측정함으로써, 영상 획득 시간과 피폭 방사선량을 줄일 수 있다. 또한, 본 연구는 샘플의 복잡한 전처리 과정 없이 금나노입자의 체외 농도를 측정할 수 있는 silicon drift detector (SDD)를 사용한 L-shell 엑스선 형광 측정 시스템을 개발하고자 한다.

방법: 금나노입자의 농도와 K-shell 엑스선 형광 신호 사이의 교정 곡선을 획득하기 위해 0.0 wt%, 0.125 wt%, 0.25 wt%, 0.5 wt%, 1.0 wt%, 2.0 wt%의 금나노입자 샘플을 반지름 2.5 cm인 아크릴 팬톰에 삽입하여 140 kVp 엑스선을 1분씩 조사하였다. K-shell 엑스선 형광 신호는 금나노입자가 삽입되어 있는 아크릴 팬톰으로부터 측정한 엑스선 스펙트럼에서 금나노입자가 삽입되어 있지 않은 아크릴 팬톰으로부터 측정한 엑스선 스펙트럼의 차이를 통해 추출하였다. 금나노입자 주입 후 측정 데이터만으로 금나노입자의 엑스선 형광 영상을 획득하기 위해 인공지능 convolutional neural network (CNN) 모델을 개발하고

적용하였다. 실험용 쥐로부터 추출한 장기의 금나노입자 농도 측정을 위해 L−shell 엑스선 형광 시스템측정을 개발하였으며, 이 시스템은 SDD 측정기와 40 kVp의 선원을 이용하여 2.34 μg – 300 μg (금나노입자)/30 mg (물) (0.0078 wt%−1.0 wt%)의 금나노입자와 L−shell 엑스선 형광 신호 사이의 교정 곡선을 얻어 장기 내 축적된 금나노입자의 질량을 측정하였다.

핀홀 엑스선 형광 영상시스템을 이용하여 실험용 쥐에 금나노입자를 주입 후 시간에 따른 신장 내 금나노입자 농도 영상을 획득하였다. 안락사 후 적출한 양쪽 신장, 간, 비장, 혈액의 금나노입자 농도를 L−shell 엑스선 형광 체외 측정 시스템과 ICP−AES를 사용하여 측정하였고 영상시스템을 통해 획득한 농도와 비교·검증하였다. 영상 획득 시 실험용 쥐에 조사되는 방사선량은 TLD를 실험용 쥐의 피부에 붙여 측정하였다.

결과: 엑스선 형광 영상 분석을 통해 측정한 실험용 쥐의 오른쪽 신장 내 금나노입자의 농도는 주입 직후 1.58±0.15 wt%였으며, 60분 후 그 농도는 0.77±0.29 wt%로 감소하였다. 개발한 인공지능 CNN 모델을 적용해 금나노입자 주입 전 영상의 획득 없이 금나노입자의 엑스선 형광 영상을 생성할 수 있었다. 적출한 장기에서 측정된 금나노입자의 신장 내 농도는 L−shell 엑스선 형광 측정법으로 0.96±0.22 wt%, ICP−AES로는 1.00±0.50 wt% 였다. 영상 획득 시 실험용 쥐의 피부에 전달된 방사선량은 금나노입자 주입 전과 후 영상을 모두 획득 시(총

2분) 107±4 mGy, CNN 모델 적용 시(1분) 53±2 mGy로 측정되었다.

결론: 2차원 CZT 감마 카메라와 핀홀 콜리메이터를 사용한 엑스선 형광 영상시스템은 영상 획득 시간과 피폭 방사선량을 크게 감소시켰으며, 살아있는 쥐의 시간에 따른 체내 금나노입자 분포 변화를 영상화 할 수 있음을 증명하였다. 또한 L-shell 엑스선 형광 측정 시스템은 복잡한 전처리 과정 없이 체외 금나노입자의 농도를 정확하게 측정할 수 있었다. 본 개발 시스템을 금속나노입자의 체내 분포 연구를 위한 전임상시험용 분자영상장비로서 활용할 수 있을 것으로 기대한다.

……………………………………………………

주요어: 엑스선 형광, 핀홀, 금나노입자, 체내 분포, 방사선량

학번: 2014-24851